LONDON metropolitan university

Faculty of Computing

Novel Narrowband Microstrip Filters for Wireless Communications Systems

Mohamad Farhat BEng (Hons), MSc

A thesis is submitted in fulfilment of requirements of

London Metropolitan University for the Degree of Doctor of Philosophy

June 2010

Acknowledgements

Foremost, I would like to express my sincere gratitude to my supervisor Dr Bal S. Virdee for the continuous support of my PhD study and research, for his patience, motivation, enthusiasm, and immense knowledge. His guidance and assistance helped me immensely throughout my research time at the University. I could not have imagined having a better supervisor and mentor for my PhD study.

I would like to thank Mr Peter Pettit for fabricating all the circuits for this research project.

I would like to thank my family, in particular my parents, my wife and my daughter for their warm encouragement as well as the generous financial support throughout my study.

I gratefully thank all my friends here in England and abroad for their continuous support and encouragement.

Abstract

The novel resonant structures based on microstrip integrated circuit technology have been developed and extensively studied in this research project for filter applications in next generation wireless communication systems. Several novel microstrip bandpass filter structures have been introduced that meet the stringent requirements for high-performance (sharp-cutoff frequency response, low insertion-loss, high return-loss, and high out-of-band isolation), compact size, low cost, and ease of integration in subsystem and systems. The analysis and modelling methods for these resonators includes a transmission-line theory, ABCD matrix, and EM simulation based on method of moments. The measured results are used to validate the performance of the devices developed and show good agreement with the theory and simulation results.

The various 'C-shape' open-loop ring resonators were developed and fabricated, namely 'Embedded-Square' and 'Embedded-Triangle' resonators, exhibited a quasi-elliptic function bandpass filter response free from spurii across an ultra-wide bandwidth. The theoretical analysis on these structures revealed that the transmission zeros (or attenuation poles) disposed at either side of the passband were a function of the length of the open-ends relative to the feed-line. It was also discovered that the input/output feed-lines had to be located asymmetrically relative to each other to yield the desired bandpass response. The 'C-shape' resonator is able to produce a very broad 3-dB bandwidth of 1027 MHz, which has a fractional bandwidth of 24.63%. This broad passband is achieved with the resonator with line width of 200 microns. In addition, it has a return-loss of 13.16 dB and insertion-loss of 1.22 dB at centre frequency of 4.17 GHz. The newly designed 'Embedded-Square' and 'Embedded-Triangle' resonators were fabricated and the measured results showed an excellent suppression of out-of-band spurious responses up to 13.8 GHz and 17.7 GHz, respectively, where the rejection is greater than 10 dB. These new structures not only achieve fractional bandwidth of around 18% and 22% for the 'Embedded-Square' resonator and 'Embedded-Triangle' resonator, respectively; but also maintain an insertion-loss at maximum of 0.7 dB. These proposed filters exhibit good stopband rejection and the measured results confirm the validity and the usefulness of these proposed filters in many practical applications.

Compact dual bandpass filters were also developed using a variant of the open-loop resonator and interconnected using an inter-digital capacitor. These microstrip structures have the ability to tune the upper passband without affecting the characteristics of the lower passband response. The tuning range is across a frequency range of $1.51f_o$, where f_o is centre frequency of the primary passband. The novel filter designs presented in this thesis provide advantage of compact size, low insertion-loss, high selectivity, and high out-of-band isolation across an ultra-bandwidth frequency range.

Table of Contents

List of Figures

List of Tables

List of Principal Symbols

θ	Electrical length
λ_g	Guided wavelength
Ω	Ohm
μ	Permeability
ε	Permittivity
ω	Angular frequency
ω_o	The centre of the operating angular frequency
ε_r	Relative dielectric constant
b	Susceptance slope
B	Susceptance
c	Velocity of light in free space
f	Frequency
f_o	Center of the operating frequency
$J_{i,i+1}$	The impedance inverter of the filter for section i
Q_U	Unloaded quality factor
Q_E	External quality factor
Q_L	Loaded quality factor
J	Inverter constant
Z	Impedance
Y	Admittance
ε_o	Permittivity of air
β	Propagation constant
ε_{eff}	Effective dielectric constant

List of Abbreviations

BPF	Bandpass filter
dB	Decibel
EM	Electromagnetic
FDD	Frequency-Division Duplex
GSM	Global systems for mobile communications
GHz	Gigahertz = 10^9 cycles per second = 10^9 Hz
Hz	Hertz
HTS	High temperature superconducting
IF	Intermediate frequency
IL	Insertion-loss
K	Kelvin
LNA	Low noise amplifier
LAN	Local area network
MIC	Microwave integrated circuit
MMIC	Monolithic microwave integrated circuit
MHz	Megahertz 10^6 cycles per second = 10^6 Hz
RF	Radio frequency
RL	Return-loss
SIR	Stepped impedance resonators
TDD	Time-Division Duplex
UMTS	Universal Mobile Telecommunications System
W-CDMA	Wideband Code Division Multiple Access

Chapter 1 Introduction

1.1 Rationale of this Research

Rapid growth of wireless communication systems and the practise of spectrum auctions have increasingly necessitated the efficient usage of the limited frequency spectrum available. In addition, with increasing subscriber numbers the interference between different systems is likely to increase. In particular, the third generation mobile communication system (UMTS) the frequency spectrum specified by the Radio communications Agency is between 1900-2025 MHz and 2110-2200 MHz, as indicated in Figure 1.1 .The satellite service uses the bands 1980-2010 MHz (uplink), and 2170-2200 MHz (downlink). This leaves the 1900-1980 MHz, 2010-2025 MHz, and 2110-2170 MHz bands for terrestrial UMTS. As can be seen from the diagram in Figure1.1, UMTS frequency domain duplex (FDD) is designed to operate in paired frequency bands, with uplink in the 1920-1980 MHz band, and downlink in the 2110-2170 MHz band. UMTS time domain duplex (TDD) is left with the unpaired frequency bands 1900-1920 MHz, and 2010-2025 MHz The up- and down-link of a TDD system operate at the same frequency. As the frequency bands of TDD systems are directly adjacent to FDD systems if the location of a FDD system base station is close to a TDD system base station, the weak up-link signals of mobile subscribers of the FDD system are interfered by strong down-link signals of the TDD base station. To avoid inter modulation in the RF front ends, highly selective preselect filters are required for an efficient exploitation of the spectrum.

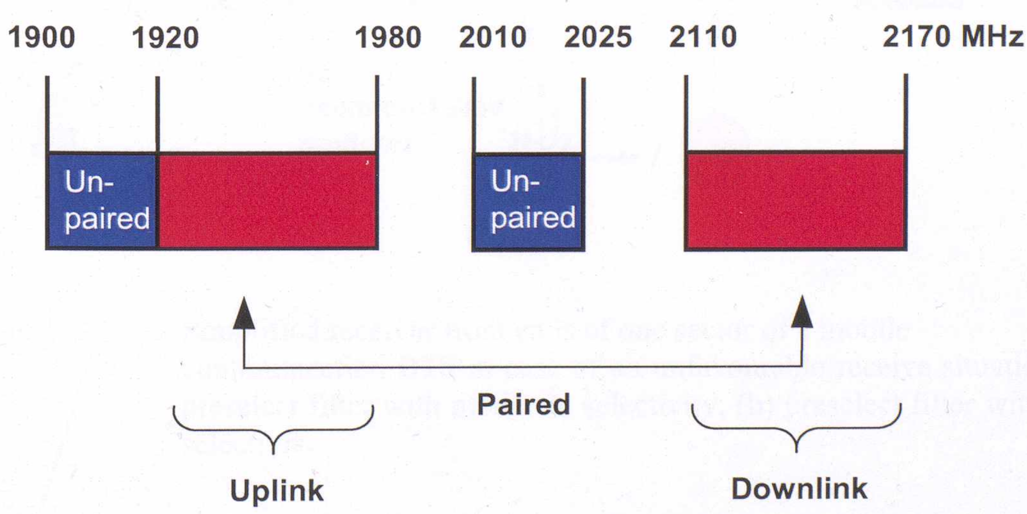

Figure 1. 1 3G Mobile Spectrum Plan [1].

The detrimental effects of intermodulation is illustrated by Figure 1.2, which shows two simplified receiver front ends for one sector of a mobile communication base transceiver station (BTS) in case of strong interference by out-of-band signals (e.g. of a different TDD mobile system). The case (a) depicts a front end with a preselect filter of moderate selectivity, whereas in (b) a filter with high selectivity is used.

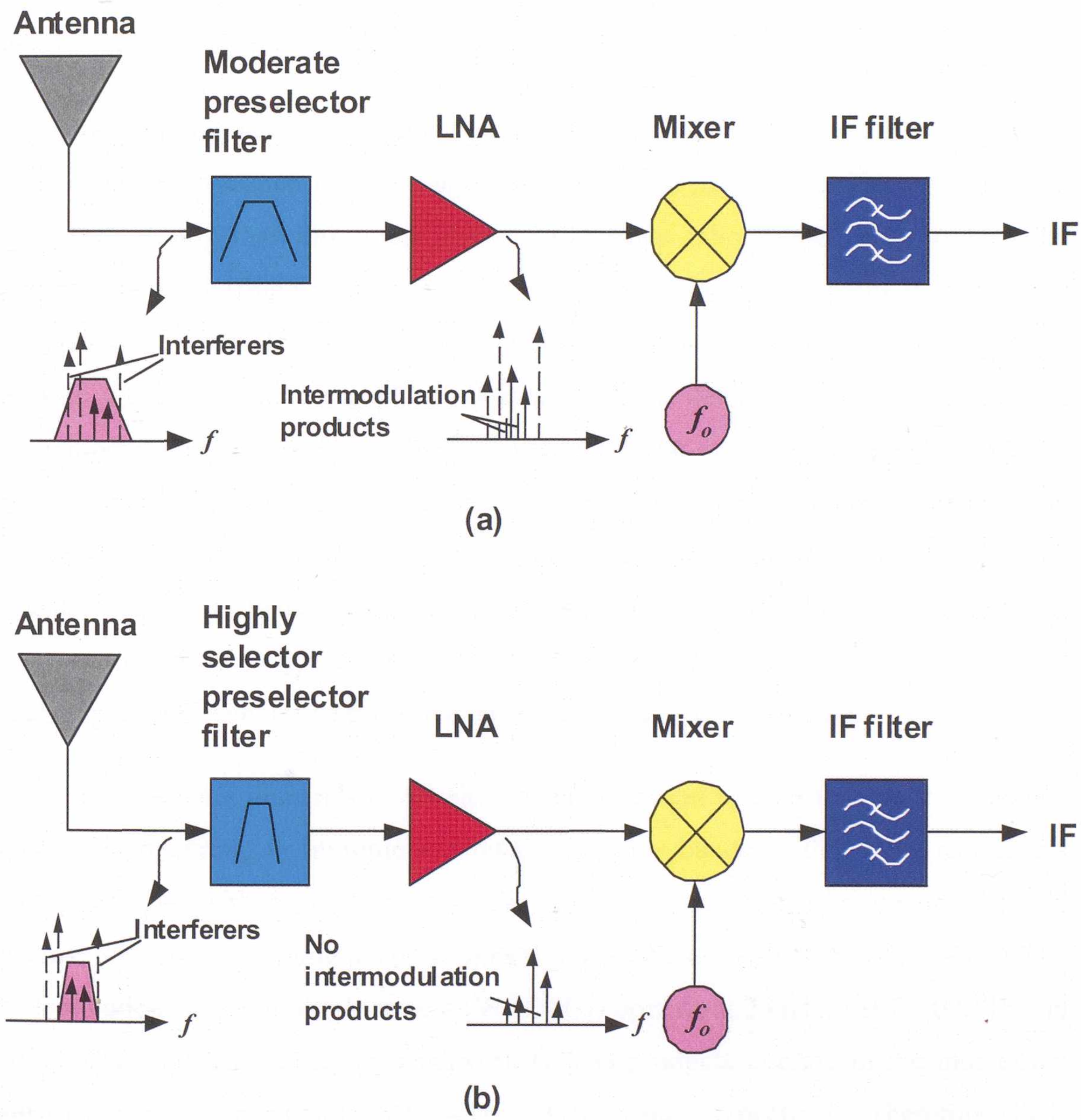

Figure 1. 2 Simplified receiver front ends of one sector of a mobile communication BTS in case of an unfavourable receive situation: (a) preselect filter with moderate selectivity, (b) preselect filter with high selectivity.

Because of the moderate filter selectivity in case (a), the signal strength of the interferers is still high at the input of the low noise amplifier (LNA). However, a real

LNA becomes nonlinear at a relatively low power level, and as a consequence intermodulation products emerge at the output of the LNA. The frequencies of some of these products are within the system bandwidth, and the bit error rate of up-link signals may therefore significantly increase. In order to avoid such incidences, highly selective filters with steep filter skirts are required. As depicted in Figure 1.2 (b), such filters are able to reduce interfering signals to power levels that do not cause nonlinearity of the LNA. However, only filters consisting of resonators with high unloaded quality factors can possess both, steep filter skirts as well as low insertion loss.

Modern microwave communication systems, especially the one described above, require high-performance narrow-band bandpass filters having low insertion-loss and high selectivity together with linear phase or flat group delay in the passband. Usually, these criteria are fulfilled using waveguide cavity or dielectric resonator loaded cavity filters because of their low loss. However, in order to reduce size, weight and cost, there has been a growing interest in planar structures. Planar microstrip resonators made of high temperature superconducting (HTS) materials have been the preferred solution to meet the requirements of highly selective preselects filters. HTS resonators can achieve unloaded quality factors which are significantly higher than those of any conventional resonator, and the planar technology offers the opportunity for miniaturisation. However, this technology requires cryogenic temperatures between 60 K and 80 K, which negates the miniaturisation advantage and is very expensive to maintain.

The increasing demands of wireless communication applications necessitates RF transceivers operating in multiple separated frequency bands so that users can access various services with a single multimode handset or terminal. For example, global systems for mobile communications (GSMs) operate at both 900 and 1800 MHz, wireless code-division multiple-access (WCDMA) operate at 2 GHz. IEEE 802.11b and IEEE 802.11a wireless local area network (LAN) products operate in the unlicensed industrial–scientific medical (ISM) 2.4 and 5 GHz bands, respectively. Therefore, dual-band filters have recently received much attention. One way of designing a dual-band filter is to combine two bandpass filters designed for two different passbands, but, it requires an implementation area twice that of a single-band filter and additional external combining networks. Thus, an integrated filter with a dual passband response is in high demand.

Microwave filters are integral components in all wireless telecommunication systems. The high demand in the use of the electromagnetic spectrum for the new applications and the limited bandwidth that is available to mobile phone service providers necessitates the need for high performance narrowband band-pass filters which have high selectivity and a wide stop band response. Traditionally, some of these criteria were fulfilled using waveguide cavity or dielectric resonator loaded cavity filters. However, such filters are large and heavy, as well as being costly to manufacture. In order to reduce the size, weight and cost, planar microstrip structures were developed to provide a viable alternative to waveguide cavity or dielectric resonator filters. A common example of a planar microstrip band-pass filter includes a parallel-coupled filter, which is widely used because of its simple design procedure and a relatively wide pass-band. The parallel-coupled structure is relatively large at low microwave frequencies, which makes it unattractive for applications that need to be small and portable. In addition, spurious bands at the harmonics of the operating frequency are inherent to such types of filter, which degrades the performance. This is because the presence of such undesired spurious bands or harmonics is a fundamental limitation of microwave filters as these unwanted responses can cause out-of-band interference in other receivers. Therefore this research will first focus on the development of novel resonant structures for filter applications that are small relative to their operating wavelength and that provide a high degree of out-of-band isolation.

With the increase in the demand for high-performance and small microwave filters to meet the evolving standards in communication systems, the objective of this research was to investigate novel microwave resonant structures that enable fabrication of compact narrowband microwave filters. Hence, this thesis introduces novel microstrip filter structures and presents numerous designs and experimental results. The filters proposed in the thesis are highly selective planar filters having a quasi-elliptic filter response, a relatively narrow-band, low passband insertion-loss and high return-loss, dual passbands, and high out-of-band rejection in order to minimize the unwanted radiation interfering with other wireless systems. These stringent requirements are demanded for mobile and satellite communication systems. The proposed filters are miniature and highly compact compared to traditional filter designs, light weight, low cost and can be easily integrated into a wireless communication system. In addition, the structure of the filter is amenable to either microwave integrated circuit technology (MIC) or monolithic microwave integrated circuit technology (MMIC).

1.2 Organisation Of The Thesis

This dissertation is organised into seven Chapters. Chapter 2 provides an overview on the recent research developments in planar microstrip filter technology for wireless microwave communication systems. Chapter 3 reviews the salient parameters that characterise microwave resonators, and briefly discusses the evolution of bandpass filters including open-loop resonators and the various coupling strategies. The 'C-shape' resonant structure is theoretically modelled and analyzed to gain insight of its properties (see Chapter 4). This structure is used to develop quasi-elliptical microstrip microwave filters. Several variants of the compact 'C-shape' resonator are developed in Chapter 5 that suppress spurious responses across an ultra-wideband frequency range. The new topologies include the 'Embedded-Square' and 'Embedded-Triangle' C-shape resonators and the Quasi-Elliptic Bandpass Filter. Chapter 6 presents novel structures microstrip dual-band bandpass filter applications. The first structure was developed by modifying the open-loop 'C-shape' resonator described in Chapter 4. The upper passband of the proposed filters is shown to have the ability to be tuned relative to the lower passband. The second structure employs symmetric resonators interconnected with an inter-digital capacitor. Overall conclusion of the work undertaken is provided in Chapter 7.

1.3 Reference

[1] UK Official Licence Auction Site: Information Memorandum *(*3G Mobile Appendix*)* http://www.three-g.net/3g_appendix.pdf]

Chapter 2 Recent Advances in Microstrip Filter Technology

2.1 Recent Developments in Microstrip Filters

This chapter presents an overview of the recent developments in planar microstrip filter technology, which is driven by the need of next generation microwave communication systems for high-performance and small-size bandpass filters required to enhance the system performance, enable full integration of communication transceiver front-ends, and to reduce the fabrication cost. In order to reduce interference by keeping out-band signals from reaching a sensitive receiver, a high-performance filter with wider upper stop-band is also required. However, the planar bandpass filters made of $\lambda/2$ resonators inherently have the spurious passbands at multiples of the centre frequency (nf_o, n = 2, 3...), which limit the rejection frequency range of the upper stopband. Hence, to satisfy these requirements numerous filter geometries have been investigated comprising of differently shaped resonators. These resonant structures constitute either a single or dual-band passband filter with the advantage of improved characteristics of passband insertion-loss and return-loss, high out-of-band rejection due to additional attenuation poles, as well as reduced physical size.

2.2 Planar Bandpass Filters

Conventionally, microstrip bandpass filters are designed with several identical resonators. It is well known that to obtain sharp cutoff frequency responses, filters need more sections, but increasing the number of sections also increases the size and insertion-loss of filters. In 1989, the miniaturised hairpin resonator [1] was developed, where the coupled lines at the ends are folded to enhance the capacitive nature of open-ends and, therefore, the resonator is much smaller than the traditional hairpin resonators. In fact, this type of resonator is a variation of stepped impedance resonators (SIRs) [2]. One of the advantages of the SIR is its compactness by controlling the impedance ratio. In [3], a stepped impedance hairpin resonator was introduced to achieve compact size and sharp cutoff frequency response. Further progress in size reduction is made by the cross-coupled hairpin resonators [4], where a resonator-embedded topology is adopted and two transmission zeros close to the passband are also realised. In 2004, J.L. Li et al. [5] reported a miniaturised bandpass filter using stepped impedance ring resonators with direct-connected feed lines, as shown in Figure 2.1. The resonator consists of four radial stubs connected to the ends of a high impedance segment; the resonator element is an improved hairpin resonator with half-ring contours. The filter was designed for the fundamental resonant frequency of 3.40 GHz and fabricated on a 0.8 mm-thick substrate with a relative dielectric constant of 9.6. Figure 2.2 shows the measured results. At the centre frequency of 3.37 GHz, the fabricated filter has a 3 dB fractional bandwidth of approximately 6.8%. Two transmission zeros adjacent to the passband have been realised at 3.1 and 3.62 GHz with the attenuations over 40 dB; additionally, a third transmission zero is located at 5.34 GHz and the attenuation is better than 45 dB. The proposed resonator enables a filter to be designed that has a size of 12 × 12 mm.

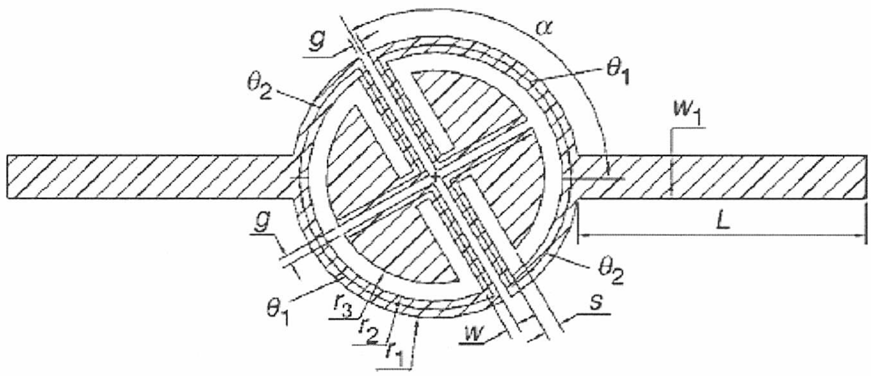

Figure 2. 1 Layout of the miniaturised bandpass filter using stepped impedance ring resonators with direct-connected feed lines [5].

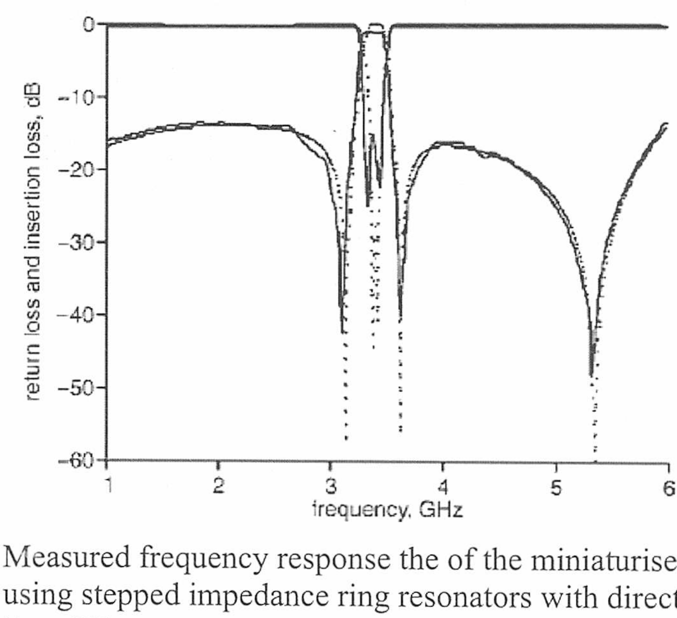

Figure 2. 2 Measured frequency response the of the miniaturised bandpass filter using stepped impedance ring resonators with direct-connected feed lines [5].

Deng, P-H., et al. [6] Presented a compact microstrip bandpass filters based on the folded quarter-wavelength (λ/4) resonators by placing a cross-coupling capacitor C2 directly between the input and output ports, as shown in Figure 2.3. The two (λ/4) resonators are mainly coupled through the shunt inductor *L*, which is realized by a metal via to the ground. This structure creates a pair of transmission zeros that improves the filter's selectivity. The measured and simulated results of the proposed filter are shown in Figure 2.4.

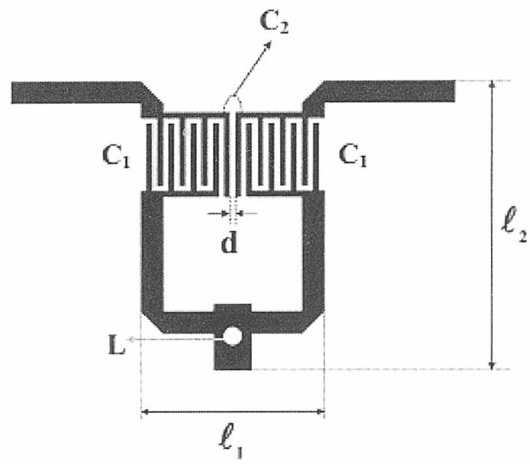

Figure 2. 3 Layout of microstrip bandpass filter based on the folded quarter-wavelength ($\lambda/4$) resonators (l_1 = 9.9 mm, and l_2 = 15.65 mm) [6].

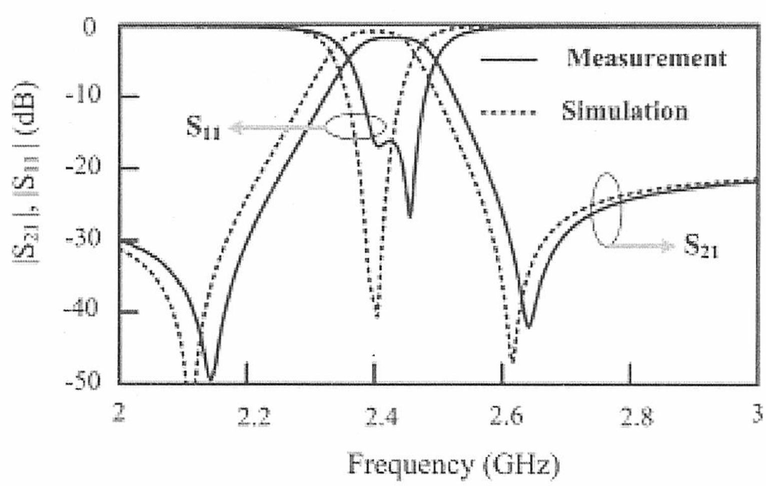

Figure 2. 4 Measured and simulated results of the second-order microstrip filter based on the folded quarter- wavelength ($\lambda/4$) resonators [6]

A compact double-mode cross-coupled microstrip bandpass filter with an asymmetric frequency characteristic and three transmission zeros was presented by Tu, W-H. [7]. The bandpass filter consists of a cross-coupled gap and a double-mode resonator of a half-wavelength line with a shunt-stepped-impedance open stub, as shown in Figure 2.5. The photograph of the final circuit and the simulated and measured results are shown in Figure 2.6. From 2.3 to 2.5 GHz, the return-loss is better than 10 dB and the insertion loss is <1.5 dB. There are three transmission zeros in the upper stopband at 2.8, 3.4 and 4.9 GHz. The size of the proposed resonator is 7.7 mm × 7.9 mm, whereas the size of the conventional square loop dual-mode resonator to obtain the same fundamental frequency is 12.2 mm × 12.2 mm, which shows that the proposed resonator achieves a 59 % size reduction.

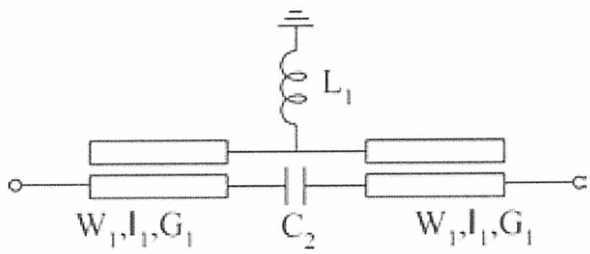

Figure 2. 5 Schematic of bandpass filters with cross coupling and lumped inductor [7].

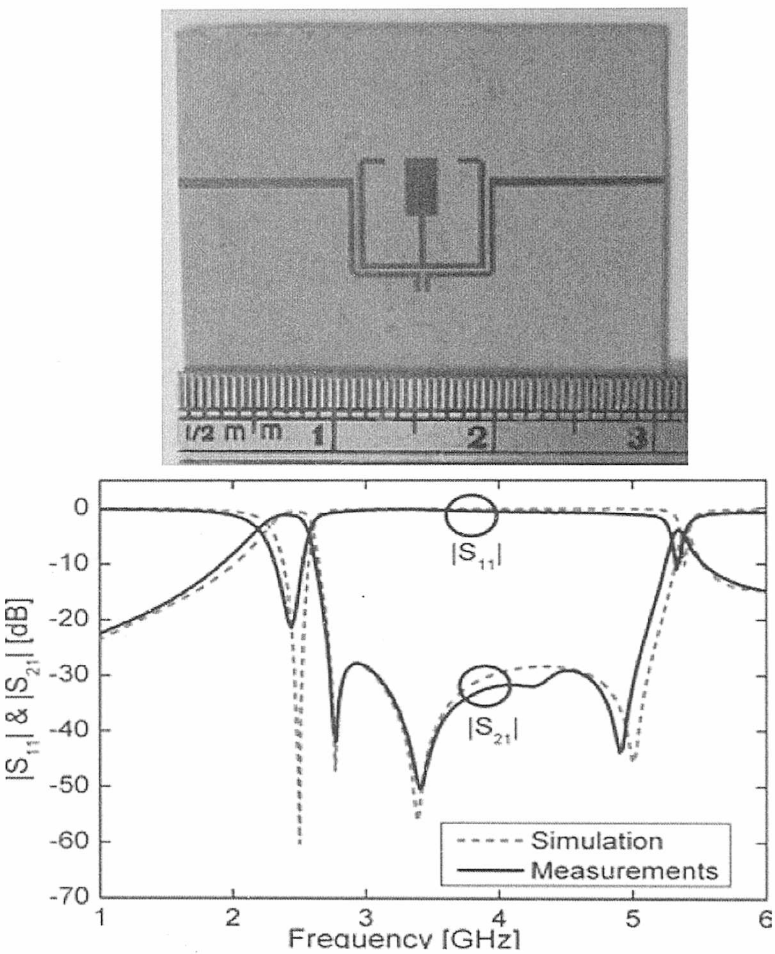

Figure 2. 6 Photograph, insertion-loss and return-loss frequency response of the double-mode cross-coupled microstrip bandpass filter [7].

The increasing demands of wireless communication applications necessitates RF transceivers operating in multiple separated frequency bands so that users can access various services with a single multimode handset or terminal. For example, global systems for mobile communications (GSMs) operate at both 900 and 1800 MHz. IEEE 802.11b and IEEE 802.11a wireless local area network (LAN) products operate in the unlicensed industrial–scientific–medical (ISM) 2.4 and 5 GHz bands, respectively. Therefore, dual-band filters have recently received much attention [8–11].

The stepped impedance resonator (SIR) has been used in dual-band bandpass filter design as it can easily realise compact size and tuneable passbands. With step-impedance resonators incorporated in a comb-filter topology [8], a dual-band bandpass filter with one transmission zero between the two passbands was designed. A high-performance dual-band filter was obtained using the equal-length coupled-serial shunted lines and the z-transform technique [9]. In [10], a dual-band bandpass filter was proposed with two half-wavelength stepped-impedance resonators cascaded. Meanwhile, a tapped coupling structure combined with the SIR was employed to achieve a dual-band bandpass filter [11].

J. Wang, et al. [12] developed a highly selective dual-band bandpass filter. The filter consists of two T-shape coupling (input and output) lines and two symmetrical radial SIRs, as shown in Figure 2.7. The passbands are generated by adjusting the structure parameters of the radial SIR. High selectivity is obtained by the introduction of two finite transmission zeros by extending the open ends of the input/output lines to T-shaped lines. The measured results in Figure 2.8 show two finite transmission zeros located between the passbands with attenuation of around 56 and 54 dB at 2.76 and 4.92 GHz, respectively, which realises a high out-of-band rejection.

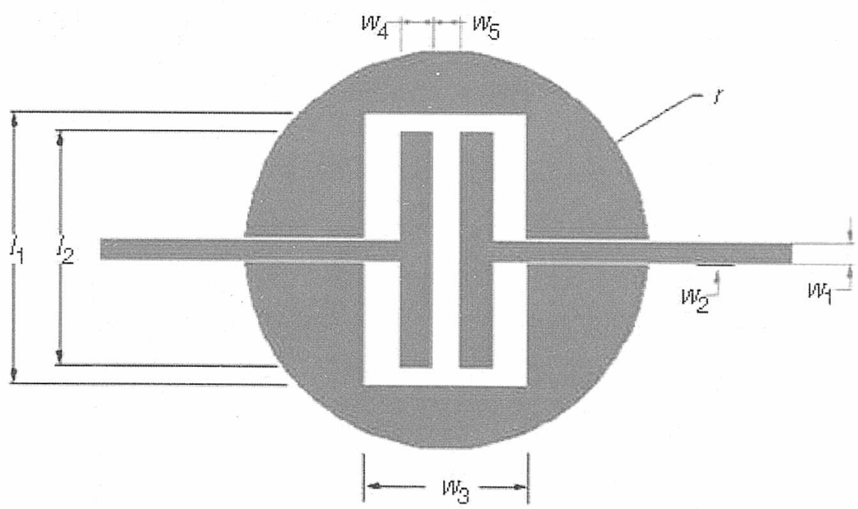

Figure 2. 7 Stepped-impedance dual-band bandpass filter [12].

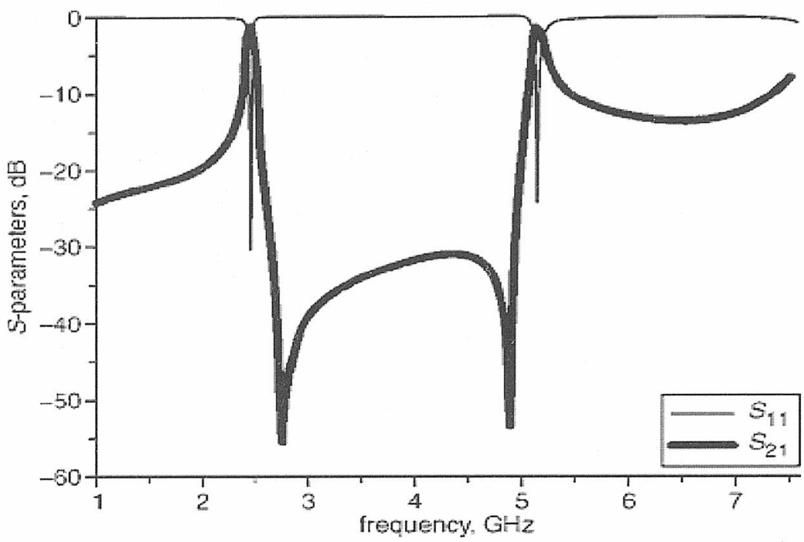

Figure 2. 8 Measured results of stepped-impedance dual-band bandpass filter [12].

A dual-mode microstrip bandpass filter reported by Liu, H.W., et al. [13] uses a triangular shaped patch, as illustrated in Figure 2.9. The filter uses two triangular patches with a coupling gap to obtain a one-pole passband. The filter also incorporates a pair of input/output spur-lines that are use to perturb the fields of the patch resonators and excite degenerate modes. The dual-mode filter was designed at about 10.4 GHz and fabricated on RT/Duriod substrates with a relative dielectric constant of 10.2 and thickness of 25 mil. The measured result is shown in Figure 2.10. The filter has a return loss better than 15 dB within 9.8–10.6 GHz and the insertion-loss is less than 0.9 dB within 9.9–10.8 GHz. The maximum return-loss is 44.6 dB at 10.6 GHz. The proposed filter is compact, simple, and attractive for modern communication applications.

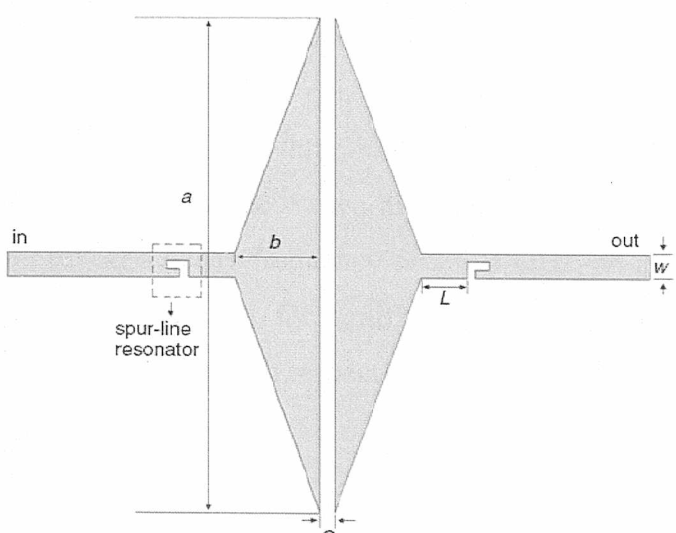

Figure 2. 9 Layout of dual-mode bandpass filter uses two triangular patches with a coupling gap [13].

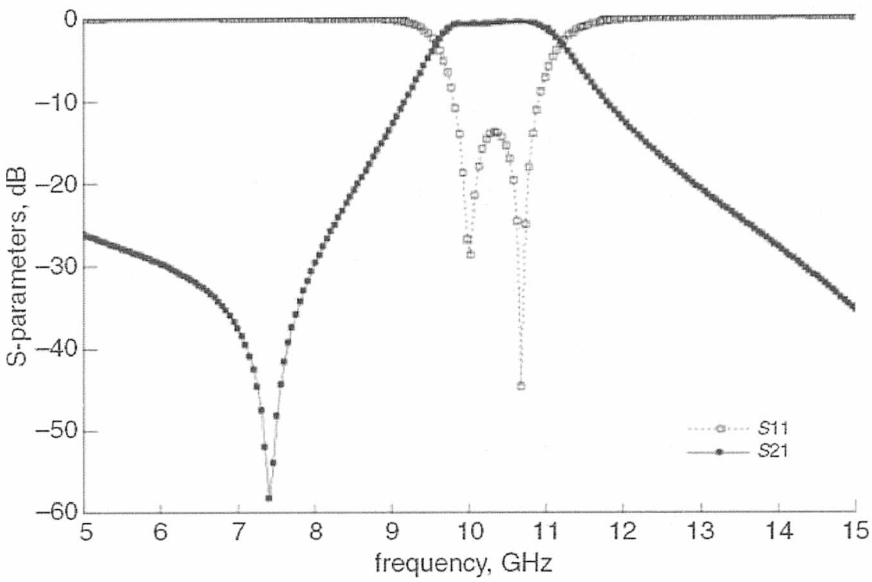

Figure 2. 10 Measured response of the dual-mode bandpass filter uses two triangular patches with a coupling gap [13].

Ring resonators have found application in many devices including oscillators, filters, and tuned amplifiers among others. The resonant frequencies of a ring resonator are all those frequencies for which the circumference of the ring represents an integral number of wavelengths. If a perturbation is added to the ring, in the form of a stub, for example, dual modes will be excited because of the asymmetry introduced into the ring [14]. These dual modes can be exploited to design narrowband bandpass filters by aligning the modes so that their response coincides as closely as possible. This is done by Fraresso, J. et al. [15] where a modification to the square resonators is implemented by employing corrugated quarter-wave couplers on all sides of the ring by adding a square perturbation in the inner corner of the resonator, as shown in Figure 2.11. The resonator is used as a constituent to construct a bandpass filter comprising two resonators coupled together with a three-line corrugated coupling structure. The simulated and experimental results are shown in Figure 2.12. The experimental results of the bandpass filter reveal a centre frequency of 2.604 GHz, an insertion-loss of 6.15 dB, and a percent bandwidth of 2.0%. Of significant importance is the 39 dB rejection of the second harmonic at 5.2 GHz with respect to the fundamental frequency.

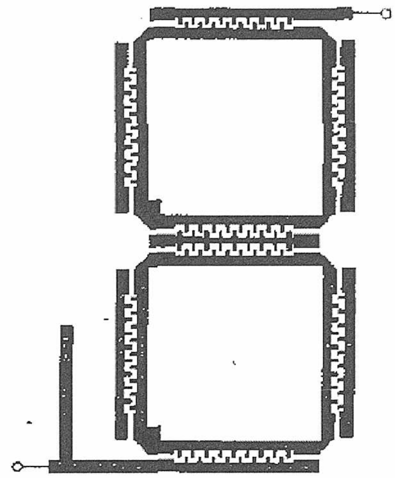

Figure 2. 11 Narrow-band bandpass filter layout [15].

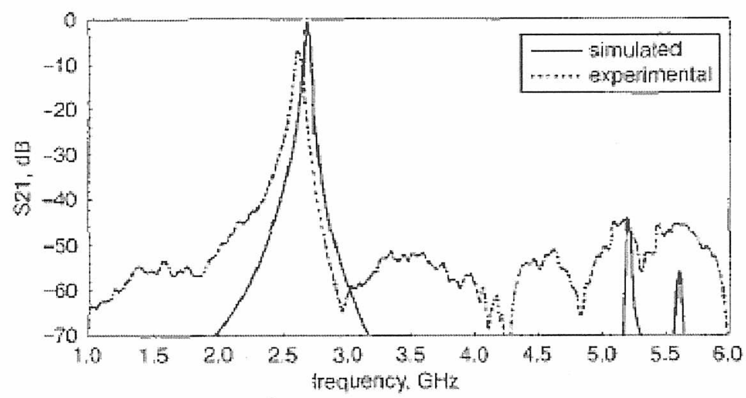

Figure 2. 12 Filter response of Figure 2.11 [15].

Modern wireless communication systems require the use of more than one frequency band. Hence, bandpass filters with a dual- and/or multi-passband response are required for such systems. An example of a triple-band bandpass filter was proposed by Guan, X., et al. [16]. This filter consists of two pairs of stepped impedance resonators, as illustrated in Figure 2.13. The longer resonators are designed to resonate at 2.4GHz and 5.7GHz, and the shorter resonators are designed to resonate at 3.8GHz. These resonators are capacitively coupled to the input and output port. The measured response of the bandpass filter is shown in Figure 2.14.

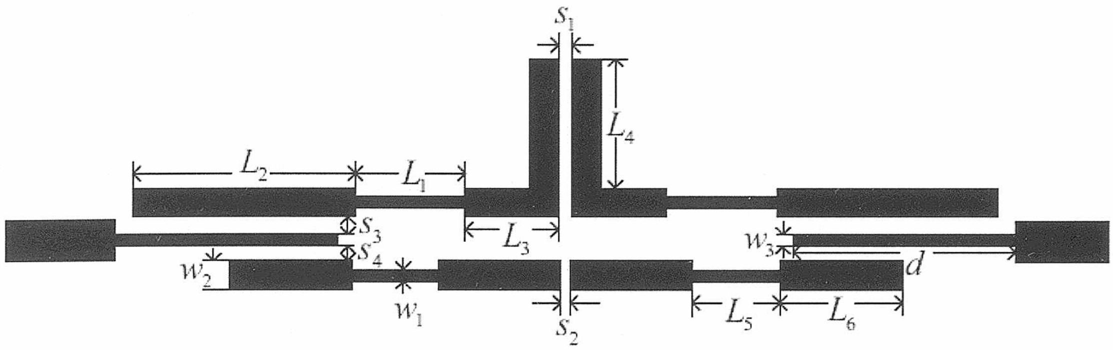

Figure 2. 13 Configuration of a triple-band bandpass filter [16].

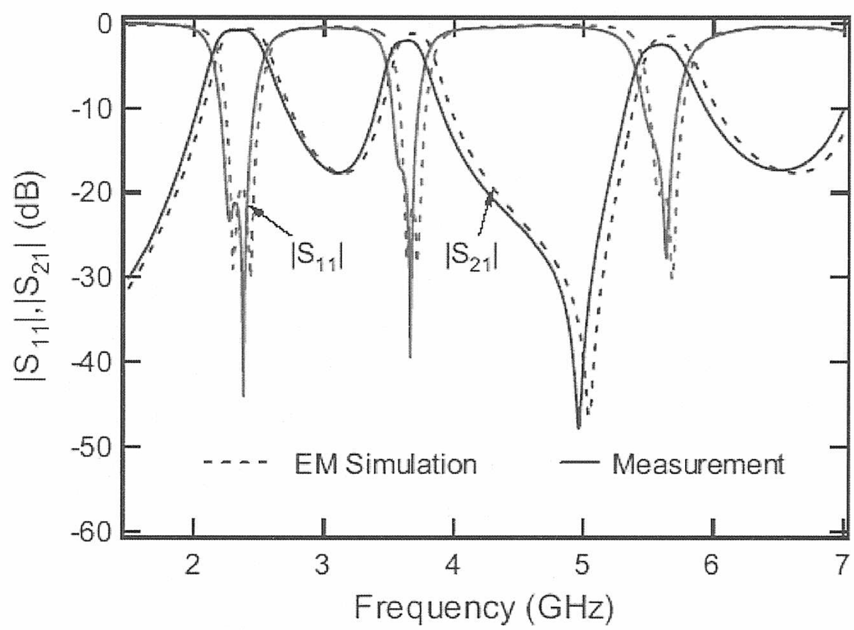

Figure 2. 14 Measured result of the tri-band bandpass filter in Figure 2.13 [16].

Like other filters open-loop bandpass filters are also haunted by spurii. Suppression of spurious responses in open-loop bandpass filters has been investigated by Tu, W-H., et al [17]. This is achieved by adding small shunt open stubs in the centre of the resonators to realise upper stopband suppression. It was discovered that by adding a short open stub in the centre of the half-wavelength resonator, as shown in Fig. 2.15, the fundamental resonant frequency remains unchanged, and the second harmonic resonance is eliminated at twice the fundamental frequency. The resonators with different stubs have different second resonant frequencies. Resonator with L5 = 5 mm has the second resonant frequency at 3.3 GHz, and resonator with L6 = 7 mm has the second resonant frequency at 2.84 GHz. Fig. 2.16 shows the simulated and measured results of the filter. It can be seen that from 1.7935 to 1.8835 GHz, the measured return-loss is better than 10 dB. The insertion-loss is 3 dB at 1.8385 GHz.

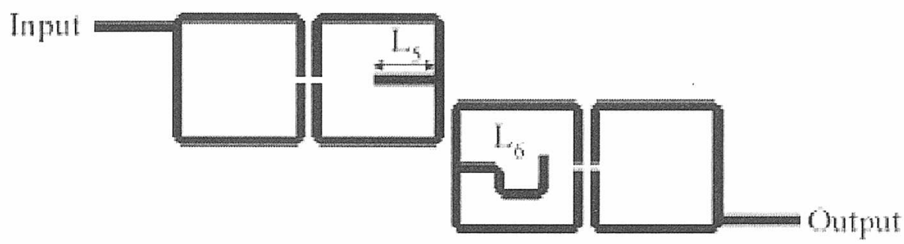

Figure 2. 15 Schematic of filter with different short open stubs [17].

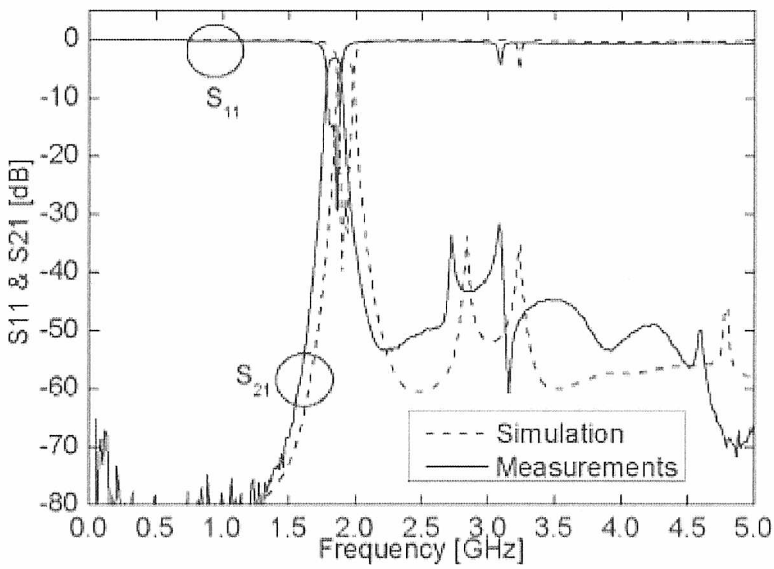

Figure 2. 16 Measured results of the bandpass filter with different short open stubs in Figure 2.15 [17].

Another design approach for the synthesis of compact microstrip filters, based on the use of complementary split-ring resonators (CSRRs), has been presented by Bonache, J., et al. [18]. The basic filter cell consists of the combination of CSRRs, shunt stubs, and series gaps. CSRR-based filters, depicted in Figure 2.17, consists of a CSRR etched in the ground-plane (underneath the conductor strip), combined with two series gaps and two shunt connected metallic wires, which are grounded by means of vias. This prototype device has been fabricated on a Rogers RO3010 substrate with dielectric constant $\varepsilon_r = 10.8$ and thickness $h = 0.635$ mm. The measured frequency response is depicted in Figure 2.18 and compared to that obtained from the equivalent-circuit model (by electrical simulation using Agilent ADS). Measured in-band insertion and return losses are IL = 1.9 dB and RL > 13 dB, respectively.

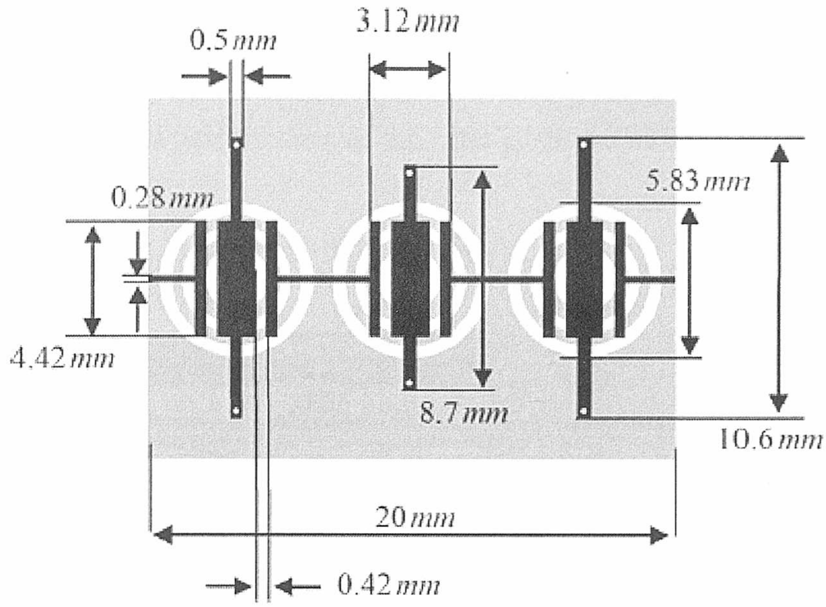

Figure 2. 17 Layout of the fabricated prototype Chebyshev bandpass filter [18].

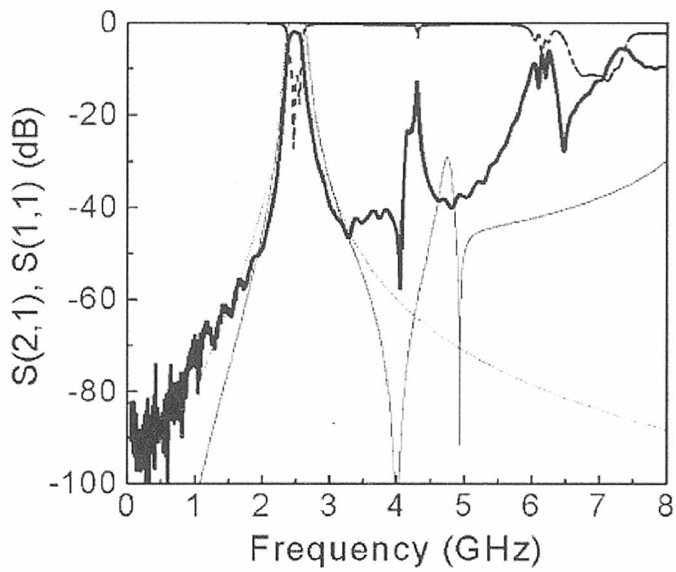

Figure 2. 18 Measured insertion-loss (solid line) and return-loss (dashed line) of the filter in Figure 2.17 [18].

An interesting approach to design microwave coupled-resonator dual-band bandpass planar filters is reported by Sanchez-Renedo, M., et al. [19]. It exploits the use of novel input/output double-coupled resonating feeding sections as key elements to produce the dual-passband filtering action, as illustrated in Figure 2.19. These feeding stages, forming triplets with their two adjacent resonators, allow dual-band bandpass filtering responses with close passbands and inter-band transmission zeros to be obtained from signal interference. Moreover, owing to their resonating behaviour, the orders of the dual passbands, and hence the filter selectivity, can be increased. A dual-passband microstrip filter circuit with bands within the 1.1–1.5-GHz range has been made on a substrate with relative dielectric constant $\varepsilon_r = 9.8$, and dielectric thickness $h = 1.19$ mm. The measured performance of the filter is shown in Figure 2.20.

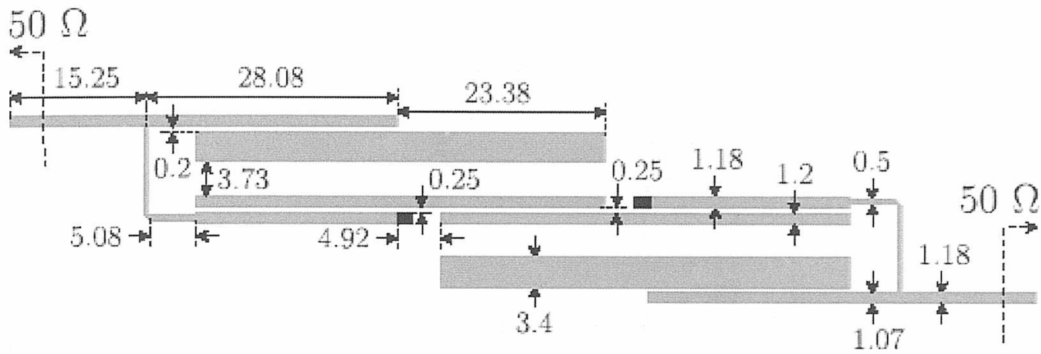

Figure 2. 19 Layout of microstrip dual-passband filter layout [19].

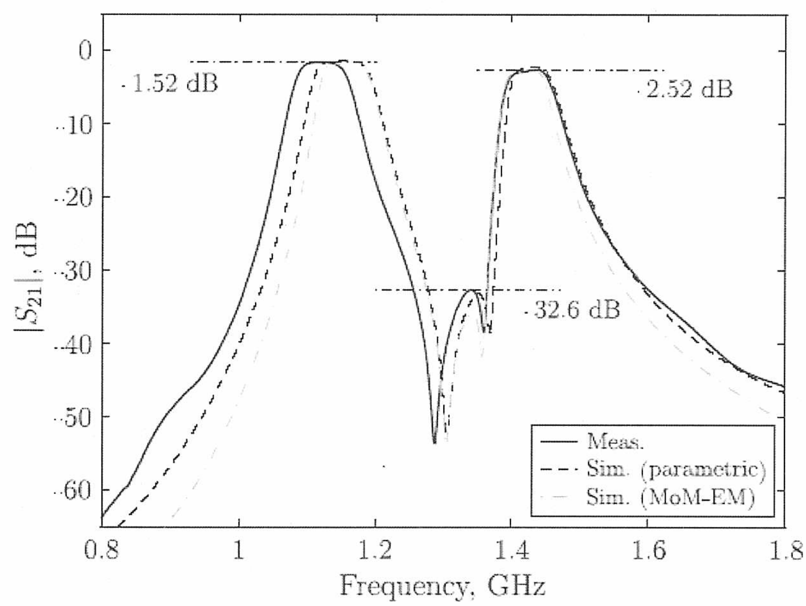

Figure 2. 20 Simulated and measured response of the microstrip dual-passband filter in Figure 2.19 [19].

Zhou, M., et al., [20] reported a compact microstrip dual band bandpass filter using novel E-type resonators. The E-type resonator is a short-circuited stub loaded hairpin resonator, as shown in Figure 2.21, The filter's two passband frequencies can be regulated by adjusting the characteristic impedance and electrical length of the hairpin and the stub. By combining pseudo-interdigital coupling structure, the coupling coefficients of two bands can be adjusted to a desired value in a relatively wide range. In addition, hook feed line is introduced to obtain desired external coupling degrees for two bands. Thus, controllable fractional bandwidths (FBWs) can be achieved. The two-order 2.45/5.25 GHz dual band bandpass filter with 3 dB FBW 5%/5% was designed on a substrate with a relative dielectric constant of 9.5 and a thickness of 0.635 mm. Figure 2.22 shows the filter's performance. The size of the filter is about 7 mm × 5.5 mm.

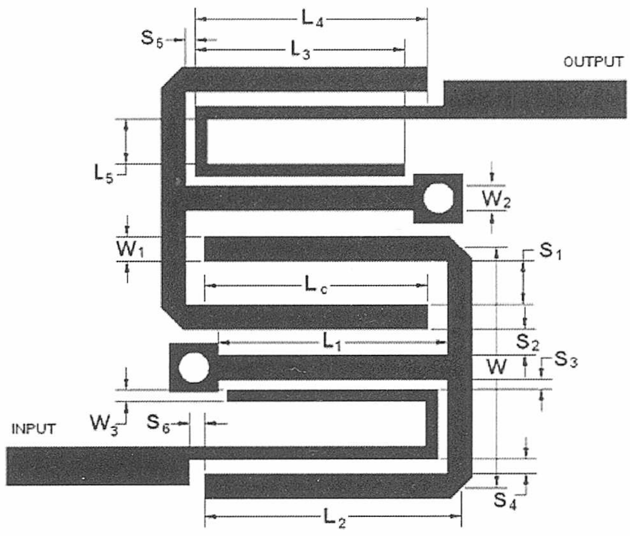

Figure 2. 21 Schematic of proposed dual band bandpass filter [20].

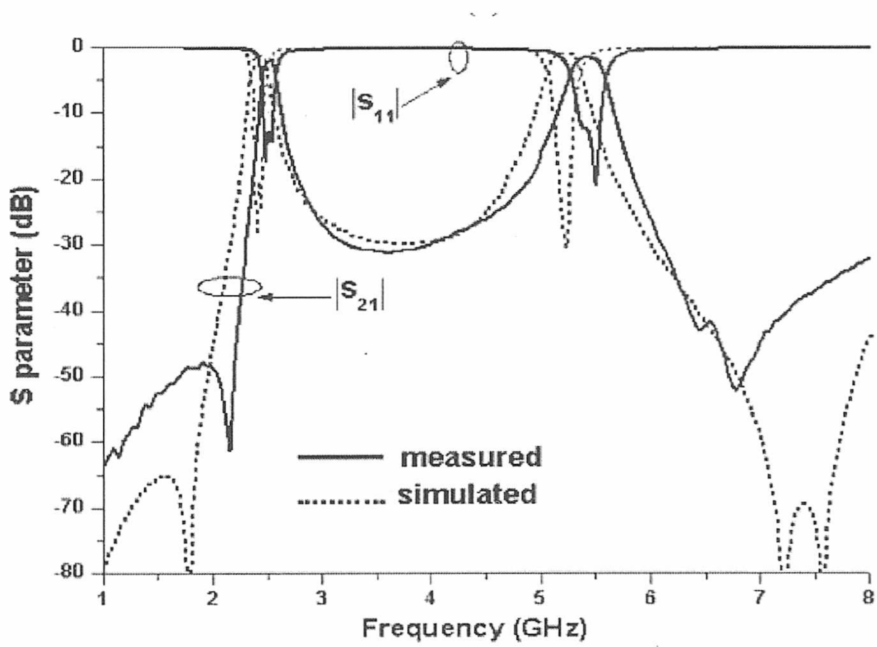

Figure 2. 22 Simulated and measured performance of the dual band bandpass filter in Figure 2.21 [20].

2.3 References

[1] Sagawa, M., Takahashi, K., and Makimoto, M.: 'Miniaturized hairpin resonator filters and their application to receiver front-end MIC's', IEEE Trans. Microw. Theory Tech., 1989, 37, (12), pp. 1991–1997.

[2] Makimoto, M., and Yamashita, S.: 'Microwave resonators and filters for wireless communication theory, design and application' (Springer, Berlin, 2001), Chaps. 2 and 4.

[3] Hsieh, L.-H., and Chang, K.: 'Compact lowpass filter using stepped impedance hairpin resonator', Electron. Lett., 2001, 37, (14), pp. 899–900.

[4] Lee, S.-Y., and Tsai, C.-M.: 'New cross-coupled filter design using improved hairpin resonators', IEEE Trans. Microw. Theory Tech., 2000, 48, (12), pp. 2482–2490.

[5] Li, J.L., Chen, J.X., Wang, J.P., Shao, W., Xue, Q., Xue, L.J., "Miniaturised microstrip bandpass filter using stepped impedance ring resonators", Electronics Letters, Vol. 40, Issue 22, 28 Oct. 2004, pages:1420–1421.

[6] Deng, P-H., Lin, Y-S., Wang, C-H., Chen, C-H., "Compact microstrip bandpass filters with good selectivity and stopband rejection IEEE Trans. Microw. Theory Tech., 2006, 54, (2), pp. 533-539.

[7] Tu, W-H., "Compact double-mode cross-coupled microstrip bandpass filter with tunable transmission zeros", IET Microwaves, Antennas & Propagation, Vol. 2, Issue 4, June 2008, pages 373 – 377.

[8] Chang, S.F., Jeng, Y.H., and Chen, J.L.: 'Dual-band step-impedance bandpass filter for multimode wireless LANs', Electron. Lett., 2004, 40, pp. 38–39.

[9] Tsai, L.C., and Hsue, C.W.: 'Dual-band bandpass filters using equal length coupled-serial-shunted lines and Z-transform technique', IEEE Trans. Microw. Theory Tech., 2004, 52, (4), pp. 1111–1117.

[10] Sun, S., and Zhu, L.: 'Compact dual-band microstrip bandpass filter without external feeds', IEEE Microw. Wireless Compon. Lett., 2005, 15, (10), pp. 644–646.

[11] Kuo, J.T., Yeh, T.H., and Yeh, C.C.: 'Design of microstrip bandpass filters with a dual-passband response', IEEE Trans. Microw. Theory Tech., 2005, 53, (4), pp. 1331–1337.

[12] Wang, J., Guo, Y.-X., Wang, B.-Z., Ong, L.C., Xiao, S., "High-selectivity dual-band stepped-impedance bandpass filter", Electronics Letters Vol. 42, Issue 9, 27 April 2006, pages 538-540.

[13] Liu, H.W., Cheng, Z.Q., Sun, L.L., "Dual-mode triangular-patch bandpass filter using spur-lines", Electronics Letters, Vol. 42, Issue 13, 22 June 2006, pages 762-763.

[14] Hsien, L.H., and Chang, K., "Dual-mode quasi-elliptic-function bandpass filters using ring resonators with enhanced coupling tuning Stubs", IEEE Trans. Microw. Theory, Tech., 2002, 50, (5), pp. 1340-1345.

[15] Fraresso, J., Saavedra, C.E., "Narrowband bandpass filter exhibiting harmonic suppression", Electronics Letters, Vol. 39, Issue 16, 7 Aug. 2003 pages 1189–1190.

[16] Guan, X., Ma, Z., Cai, P., "A novel compact bandpass filter with a triple-passband response", APMC Microwave Conference, 16-20 Dec. 2008, pages 1-4.

[17] Tu, W-H., Li, H., Michalski, K.A., Chang, K., "Microstrip Open-Loop Ring Bandpass Filter Using Open Stubs for Harmonic Suppression", IEEE MTT-S Microwave Symposium Digest, 11-16 June 2006, pages 357-360.

[18] Bonache, J., Gil, I., Garcia-Garcia, J., Martin, F., "Novel microstrip bandpass filters based on complementary split-ring resonators", IEEE Trans. Microw. Theory and Tech., Vol. 54, Issue 1, Jan. 2006, pages 265-271.

[19] Sanchez-Renedo, M., Gomez-Garcia, R., "Microwave dual-band bandpass planar filter using double-coupled resonating feeding sections", European Microwave Conference, Sept. 29 2009-Oct., 2009, pages 101-104.

[20] Zhou, M., Tang, X., Xiao, F., "Compact Dual Band Bandpass Filter Using Novel E-Type Resonators With Controllable Bandwidths", IEEE Microwave and Wireless Components Letters, Vol. 18, Issue 12, Dec. 2008, pages 779–781.

Chapter 3 Resonators and Filters

3.1 Resonator

A resonator is an element where the amplitude of the current flow into it becomes significant, which is when the signal frequency is close to its resonance (Eigenvalue). Resonance starts to occur when the size of the element is about half-wavelength [1]. Any structure that is able to contain at least one oscillating electromagnetic field is called microstrip resonator [2]. Combinations of L and C elements form resonators. Four types of L and C combinations are shown in Figure 3.1, while Figure 3.2 shows their corresponding equivalent circuits at resonant frequencies [3].

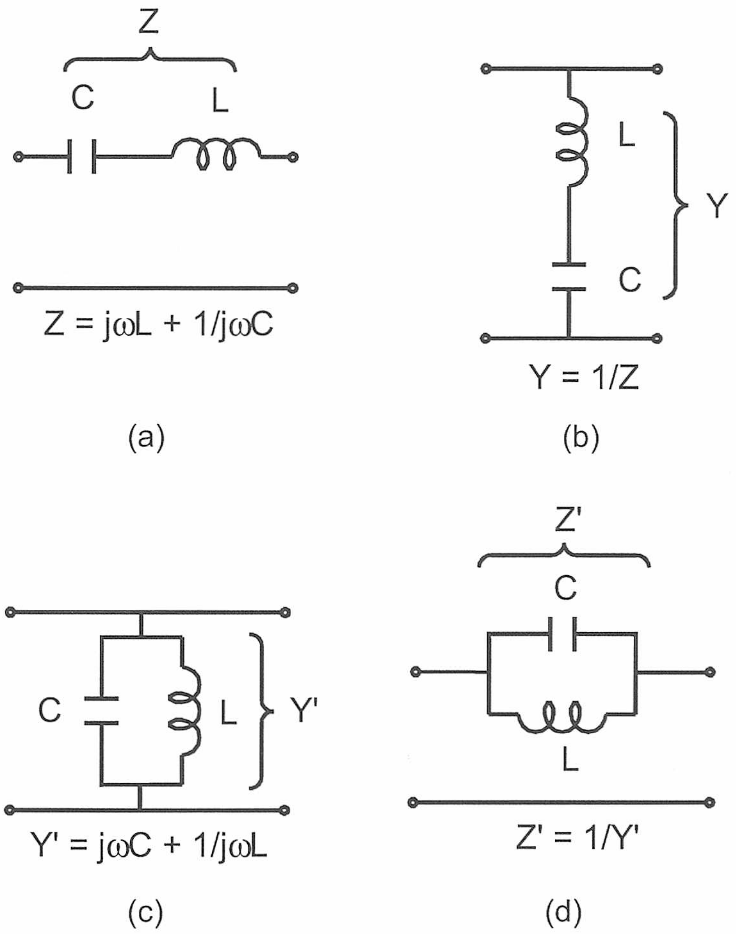

Figure 3. 1 Four different basic resonant circuits.

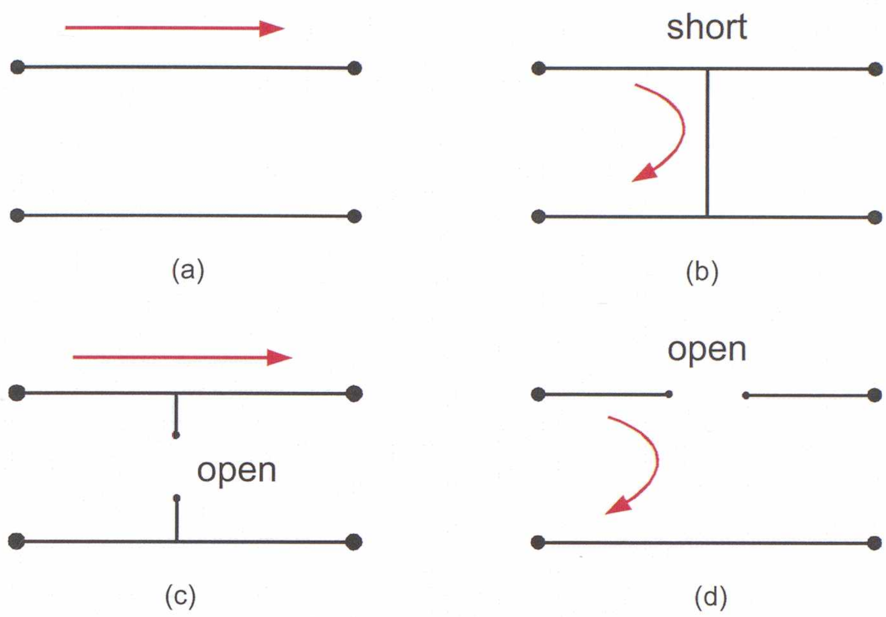

Figure 3. 2 The equivalent circuits at resonance for the four resonant circuits shown in Figure 3.1.

Resonators in practice include losses, and Figure 3.3 shows the resonator circuits in Figure 3.1(a) and 3.1(c) with loss elements *R* and *G* associated with resonators.

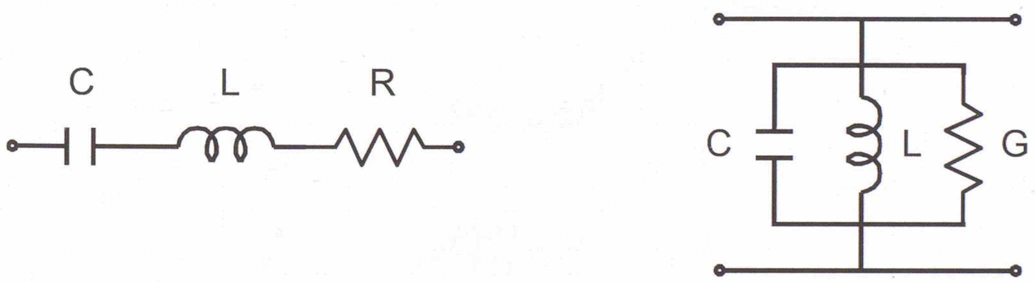

Figure 3. 3 Resonators with lossy elements *R* and *G*.

Resonant frequency occurs when the impedance of a series resonant circuit is minimum or maximum for a parallel resonant circuit. It is given by [4]

$$\omega_o^{\,2} = \frac{1}{LC} \tag{3.1}$$

or

$$f_o = \frac{1}{2\pi\sqrt{LC}} \tag{3.2}$$

Where f_o = resonant frequency (in Hertz)
L = inductance (in Henries)
C = capacitance (in Farads)

Figure 3.4 shows the commonly used resonators for microstrip circuits. Each resonator structure resonates at a certain frequency, which is limited by the boundary condition [3]. Patch resonators have lower conductor losses and higher power handling capability as compared with narrow microstrip line resonators [2].

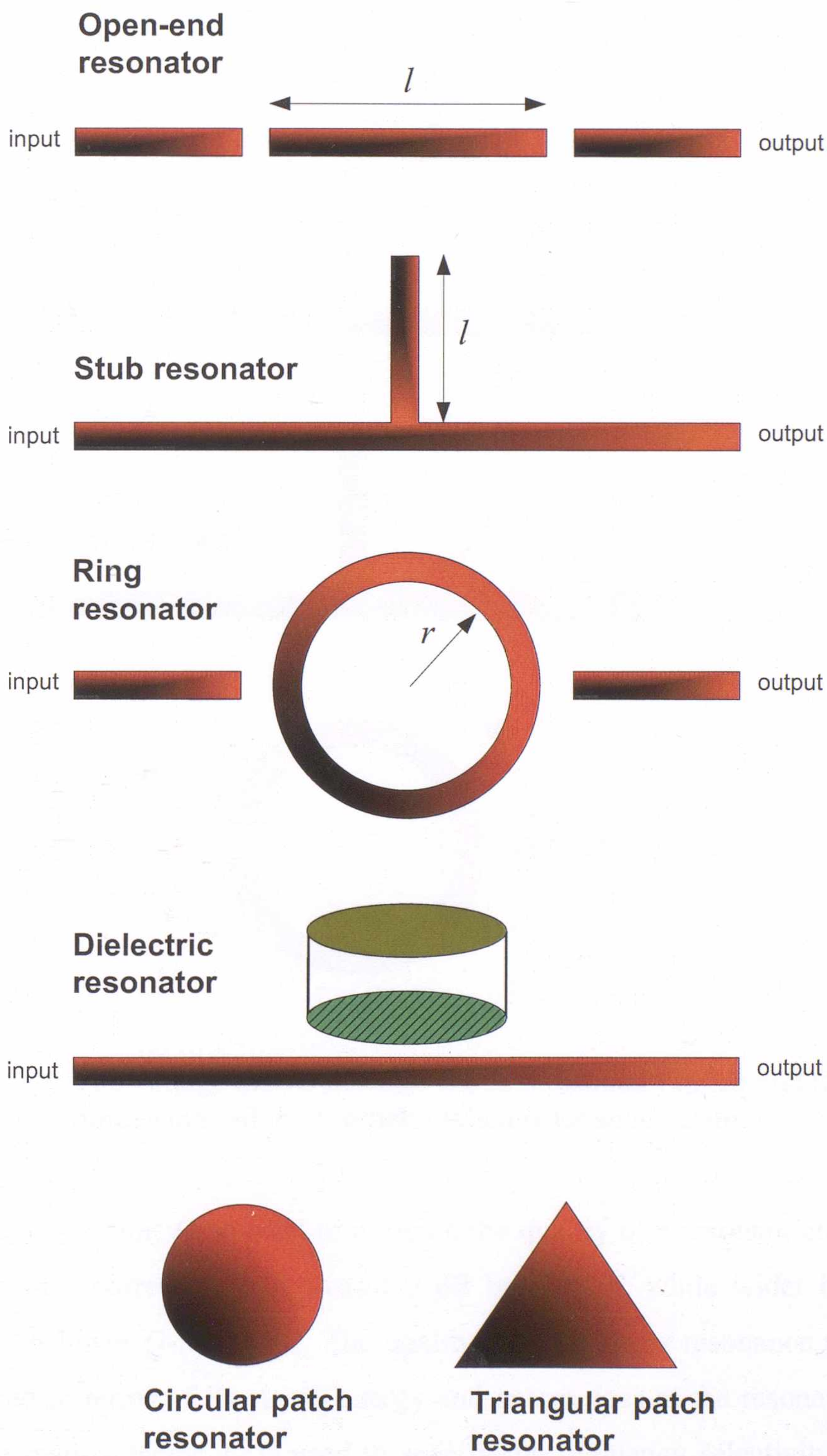

Figure 3. 4 Commonly used resonators for microstrip circuits.

The voltage distribution for the first resonator mode and the dimension of the resonator when resonance occurs for various structures is shown in Figure 3.5. The resonant frequency can be obtained by using the following relationship [3]

$$\lambda_g = \frac{\lambda_o}{\sqrt{\varepsilon_{eff}}} = \frac{c}{f\sqrt{\varepsilon_{eff}}} \tag{3.3}$$

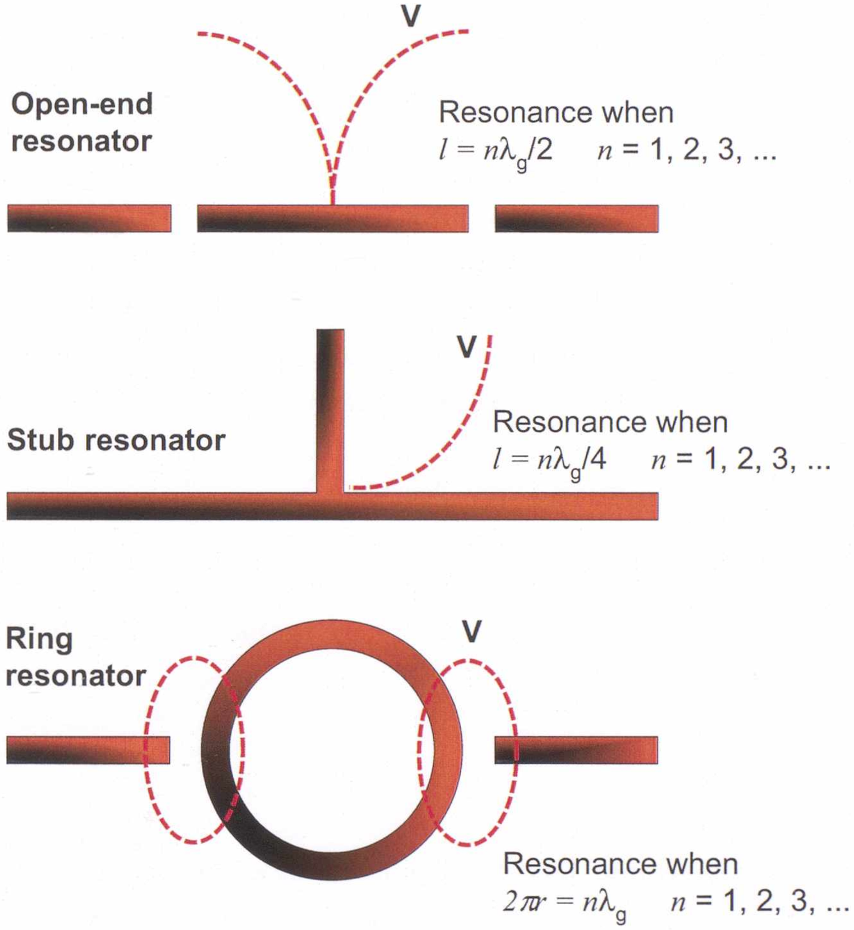

Figure 3. 5 The voltage distribution for the first resonator mode and the dimension of the resonator when resonance occurs.

The quality factor, Q, is used to measure the quality of a resonant circuit. A high value of Q-factor corresponds to narrow 3-dB bandwidth, while wider bandwidth is associated with lower Q-factor [4]. The quality factor for any resonance phenomenon can be defined in terms of its stored energy and energy loss at the resonant frequency [5]. Also the quality factor, Q is used to specify the frequency selectivity and energy loss. For a parallel resonator,

$$Q = \frac{R}{\omega L} \tag{3.4}$$

On the other hand, for a series resonator,

$$Q = \frac{1}{\omega CR} \tag{3.5}$$

$$Q = 2\pi \left.\frac{energy\ stored}{energy\ loss\ per\ cycle}\right|_{at\ \omega_o} = \left.\frac{energy\ stored}{average\ power\ loss}\right|_{at\ \omega_o} \tag{3.6}$$

Where ω_o is the resonant frequency.

In any circuit application the resonator is always coupled to external circuit load. Hence the net resistance and the Q-factor are changed by this loading effect [3].

Three Q-factors, Q_U, Q_E and Q_L are defined as:

Unloaded-Q
$$Q_U = \omega_o \left.\frac{energy\ stored\ in\ the\ resonant\ circuit}{power\ loss\ in\ the\ resonant\ circuit}\right|_{at\ \omega_o} \tag{3.7}$$

External-Q
$$Q_E = \omega_o \left.\frac{energy\ stored\ in\ the\ resonant\ circuit}{power\ loss\ in\ the\ external\ circuit}\right|_{at\ \omega_o} \tag{3.8}$$

Loaded-Q
$$Q_L = \omega_o \left.\frac{energy\ stored\ in\ the\ resonant\ circuit}{total\ power\ loss}\right|_{at\ \omega_o} \tag{3.9}$$

and they are related with this relationship:

$$\frac{1}{Q_L} = \frac{1}{Q_E} + \frac{1}{Q_U} \tag{3.10}$$

The unloaded Q-factor is related with loaded Q-factor and insertion-loss (IL) by [3]:

$$Q_U = \frac{Q_L}{1 - 10^{-IL/20}} \tag{3.11}$$

For a frequency response of a network, the loaded-Q factor is obtained using:

$$Q_L = \frac{f_o}{f_2 - f_1} = \frac{resonant\ frequency}{3\ dB\ (half - power)\ bandwidth} \tag{3.12}$$

Where $f_o = \sqrt{f_1 f_2}$ and f_1 and f_2 are the frequencies at which the current or voltage is 0.707 of its magnitude at resonance. These frequencies correspond to the half-power point on a power versus frequency curve.

The common losses in a microstrip resonator are attributed to the conductor, dielectric substrate and radiation. However, for filter applications, radiation Q-value can be replaced by Q-factor associated with the housing loss, because microstrip resonators are normally shielded in package housing [2]. Figure 3.6 shows a typical resonance response. A typical *Q*-value of a microstrip resonator line is < 200, and for a dielectric resonator is around 1000 [3].

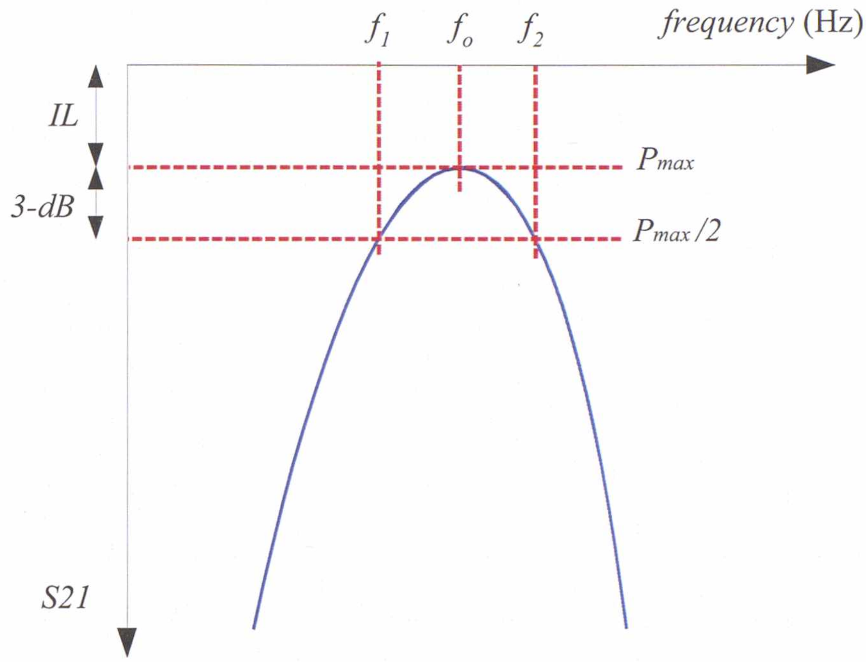

Figure 3. 6 Resonator frequency response.

3.2 Evolution of Bandpass Filters

Microwave filters belong to the most commonly used passive components in all microwave communication systems. They are, by nature, distributed networks that usually consist of periodic structures to exhibit passband and stopband characteristics in various frequency bands. It is desirable that a design method would be able to determine the physical dimensions of a filter structure having the desired frequency characteristics. Research on microwave filters has spanned more than sixty years, and the number of contributions devoted to the design methods of microwave filters is enormous.

A generalized design procedure is shown in Figure 3.7 as a flow chart. The design begins with the desired filter performance, which is usually determined by the requirement of a microwave system and expressed in terms of electrical, mechanical, and environmental parameters. Commonly used electrical parameters include: centre frequency, 3-dB bandwidth, insertion-loss, gain, flatness, return-loss, stopband attenuation, group delay or phase linearity, and power handling capability. Mechanical requirements are usually characterized by constraints of the maximum volume, weight, and filter interfaces.

Environmental requirements include the vibration test and the thermal drifting limitation (i.e., the electrical performance must be maintained in the considered environments). Even though the objective of a design is to satisfy all the given specifications, sometimes a compromise has to be made between the electrical, mechanical and environmental requirements to obtain a feasible physical structure. Therefore, final specifications of a filter design are usually decided with the consideration of the system requirements, design feasibility, physical realisation, and the cost.

The evolution of microwave microstrip bandpass filter traces the following steps:

1. End coupled resonator
2. Parallel coupled resonator
3. Hairpin resonator
4. Improved hairpin and open loop resonator
5. Miniaturised and compact resonator

End-coupled and parallel-coupled resonators constitute two basic forms of microwave bandpass filters in microstrip line, and they are named by the method of coupling energy into the resonators [6]. The simple structure of end-coupled bandpass filter, shown in Figure 3.8, shows how capacitive coupling between adjacent resonators is achieved at the resonator's open-ends. Each resonator is approximately a half-guided wavelength long at the mid-band frequency, f_o of the bandpass filter [2]. The smaller the gap between the $\lambda_g/2$ resonators, the larger the capacitive coupling which leads to a larger bandwidth. Unfortunately, this type of filter occupies a large area.

One of the difficulties of using capacitive coupled resonators is that the series coupling capacitance may be of such large value that it may be difficult to implement in practice. In this situation, the gap separation between the adjacent resonators becomes very small presenting a potential problem for fabrication. In many instances, a very precise capacitance value is needed for a desired filter response. Hence, this is a major problem in the main as it limits the use of end-coupled bandpass filters in many applications.

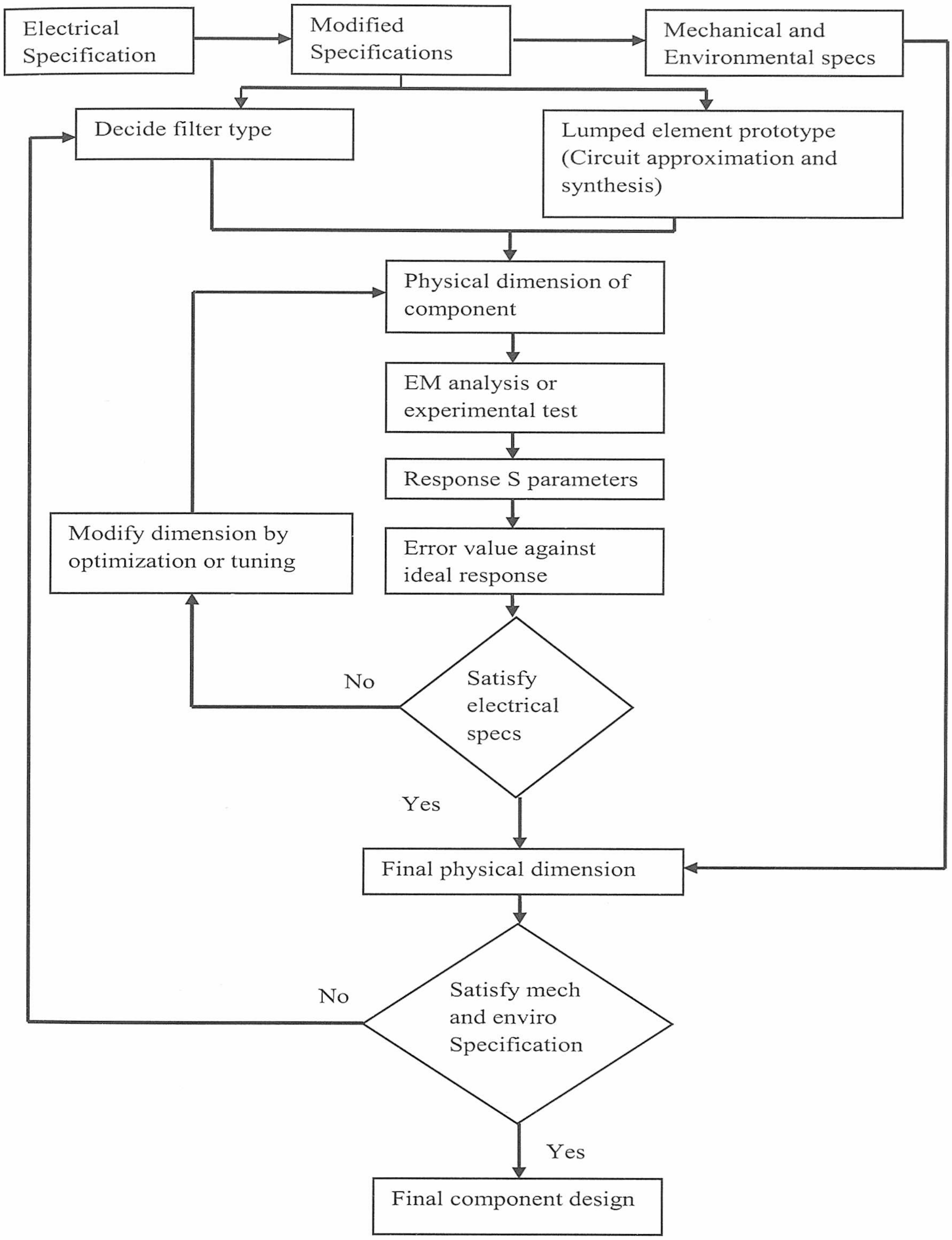

Figure 3. 7 Generalized design procedure.

This dilemma is illustrated in the following example [2]. An end-coupled bandpass filter design having a fractional bandwidth of 2.8% at the mid-band frequency of 6 GHz, with Chebyshev passband ripple of 0.1 dB can be implemented with three-poles. The coupling capacitances between the input and the first resonator ($C_g^{0,1}$) or between the third resonator and output ($C_g^{3,4}$) are 0.11443 pF; and the coupling capacitances between the first and second resonators ($C_g^{1,2}$) or between the second and third resonators ($C_g^{2,3}$) are 0.021483 pF. The dimensions of the microstrip gaps that produce the desired capacitances are $S_{0,1} = S_{3,4} = 57$ µm and $S_{1,2} = S_{2,3} = 0.801$ mm when fabricated on a substrate with $\varepsilon_r = 10.8$ and $h = 1.27$ mm. These gaps are very difficult to realise precisely using conventional manufacturing processes, which makes this type of bandpass filter configuration practically unfeasible and unpopular.

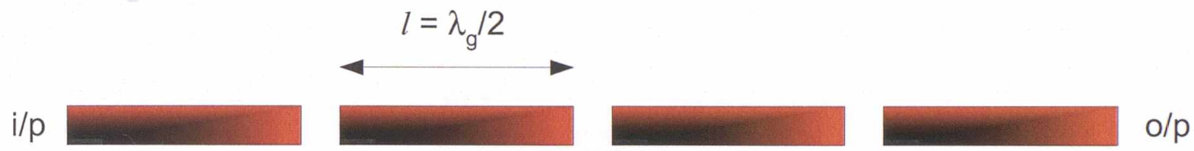

Figure 3. 8 Structure of microstrip-line end-coupled filter.

Resonance occurs for an open-end resonator when the length of resonator is

$$l = n\lambda_g/2 \qquad \text{where } n = 1, 2, 3, \ldots \tag{3.13}$$

Figure 3.9 shows the topology of a parallel-coupled filter, which consist of $\lambda_g/2$ resonators that coupled through the even- and odd-mode fields along the edge of the lines.

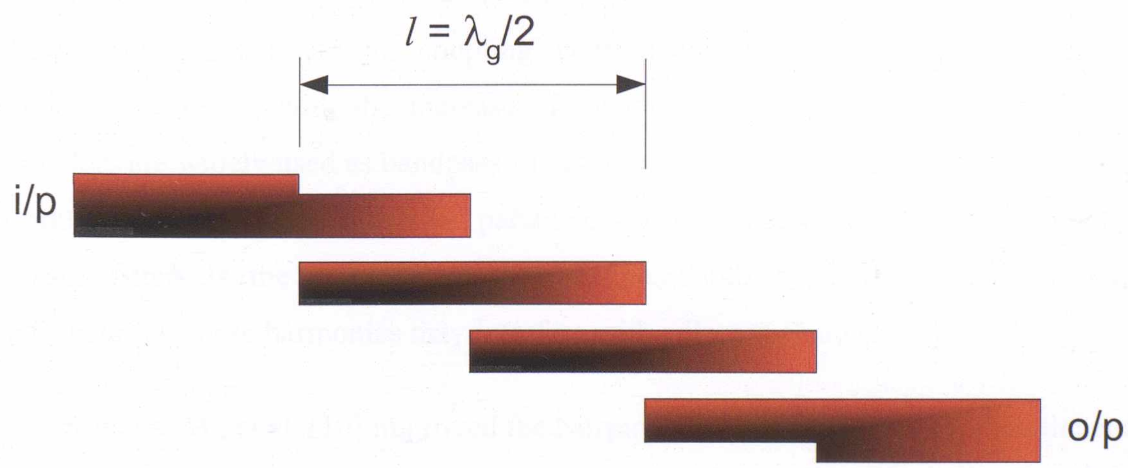

Figure 3. 9 Microwave parallel-coupled filter.

The parallel-coupled sections of the resonator structure compensate for the relatively small resonator-to-resonator spacing encountered in end-coupled filters. This type of filter was first reported by Cohn, S.B. in 1958 [7]. This parallel arrangement enables relatively large coupling with a given spacing, thus it is easier to generate a wider bandwidth as compared to the end-coupled structure [2]. Conventional planar filters consisting of parallel-coupled $\lambda_g/2$ resonators are also relatively large in size, have a low in attenuation rate, in addition to unwanted spurious passband responses at 2, 3, and 4 times the centre frequency, f_o, of the filter.

Cristal, E.G. et al. [8] reported the improved version of coupled filter, as illustrated in Figure 3.10, by folding the resonator to form a 'U' shape open-line hairpin resonator order to reduce the circuit size, as illustrated in figure 3.10.

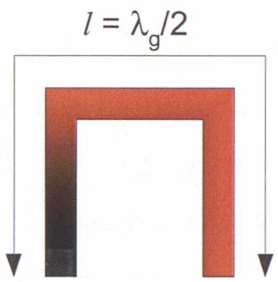

Figure 3. 10 The basic structure of the hairpin filter.

The design equations for the parallel-coupled, half wavelength resonator filters are valid for this hairpin resonator as well. However, by folding the resonator, there is reduction of the coupled-line lengths, which reduces the coupling between resonators. In addition, if the two arms of each hairpin resonator are closely spaced, they function as a pair of coupled line, which can have an effect on the coupling as well [2]. As with other coupled structures the coupling coefficient between two adjacent hairpin resonators decreases with the increase of the distance. Parallel-coupled and hairpin resonators are widely used as bandpass filters in microwave systems because of the ease of implementation and well defined parameters. Unfortunately, one intrinsic limitation of such filters is the presence of spurious passbands appearing at the harmonic frequencies, as these harmonics may interfere with adjacent channels [9].

Sagawa, M., et al. [10] improved the hairpin resonator by further bending the ends of the hairpin so that the open-ends are parallel-coupled, as illustrated in Figure 3.11. The advantages of this type of resonator include:

- small size, with no Q-value degradation
- expansion of the applicable frequency range
- easy adjustment of resonance frequency

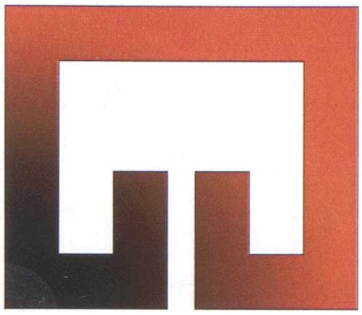

Figure 3. 11 Improved hairpin resonator.

Various modifications have been done to improve the frequency response of the classical coupled-lines narrow bandpass filters. Miniaturised and compact filters are currently under investigating for application in next generation wireless communications systems. Desired featured sought include improvement in filter performance in terms of improved sharpness, low passband insertion-loss, wideband spurious free response, and small size. In response to these stringent requirements Prigent, G. et al. [11] have managed to create an additional transmission zero (attenuation pole) by replacing the input and output coupled lines with tapped feeding lines. This modification of the geometry favours the coupling between non-adjacent resonators, as illustrated in Figure 3.12.

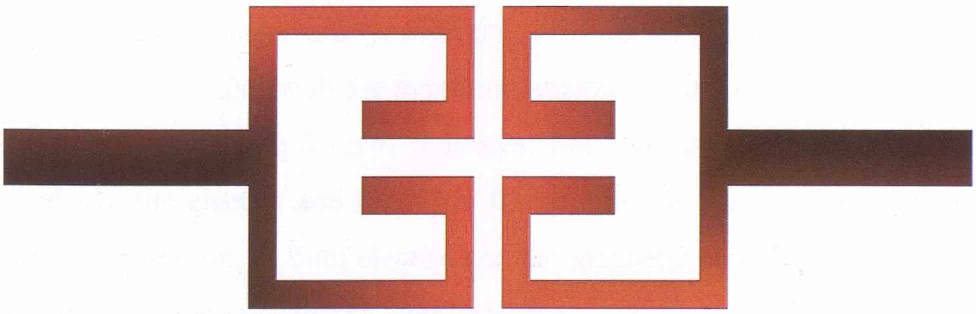

Figure 3. 12 The open-loop resonators with tapped feeding lines.

The choices of resonator type are determined by factors such as [12]:

- The size, as a function of the distributed capacitance and inductance within the geometry
- The relationship of spacing or coupling factors between adjacent
- The ability to realise coupling of different phase between adjacent resonators, i.e. electric and magnetic coupling type. This enables the realisation of quasi-elliptic function filters.

- The location of the first spurious response
- The ability to tune

3.2 Coupling Types and Zones

There is a general technique to design coupled resonator filters, which is based on coupling coefficient of inter-coupled resonators and the external quality factors of the input and output of resonators. This technique can be applied to any type of resonator despite its physical structure [2]. Figure 3.13 shows various types of coupled microstrip resonators. These coupled structures results from different orientations of a pair of open-loop resonators, which are separated by a spacing s. It is obvious that any coupling in these structures is proximity coupling, which is, basically, through fringe fields. The nature and the extent of the fringe fields determine the nature and strength of the coupling. It can be shown that at resonance of the fundamental mode, each of the open-loop resonators has the maximum electric field density at the side with an open gap, and the maximum magnetic field density at the opposite side. Because the fringe field exhibits an exponentially decaying character outside the region, the electric fringe field is stronger near the side having the maximum electric field distribution, whereas the magnetic fringe field is stronger near the side having the maximum magnetic field distribution. It follows that the electric coupling can be obtained if the open sides of two coupled resonators are in proximity, as Figure 3.13 (a) suggests. Magnetic coupling can be obtained when the sides with the maximum magnetic field of two coupled resonators are in proximity, as Figure 3.13(b) indicates. For the coupling structures in Figures 3.13(c) and (d), the electric and magnetic fringe fields at the coupled sides may have comparative distribution, so both electric and the magnetic couplings occur. In this case the coupling is referred to as mixed coupling [2].

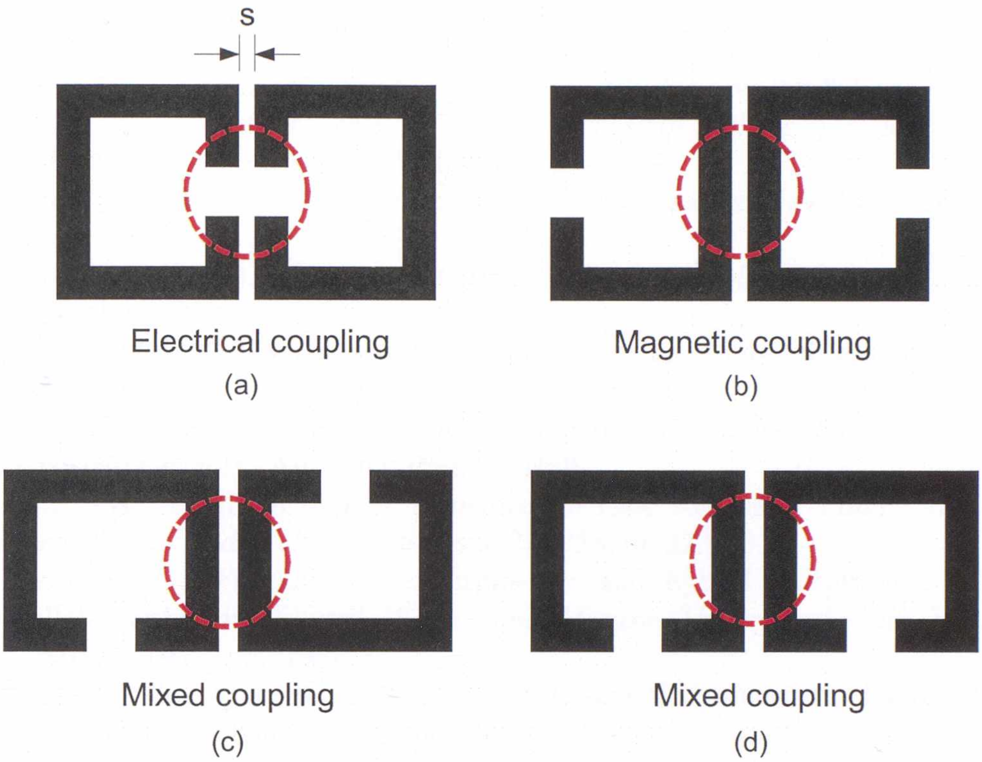

Figure 3. 13 Typical coupling structures of coupled resonators with (a) electric coupling, (b) magnetic coupling, (c) and (d) mixed coupling.

The coupling coefficient, k, of coupled resonators, regardless of whether it is electric, magnetic or mixed coupling is given by [2]

$$k = \pm \frac{f_2^2 - f_1^2}{f_2^2 + f_1^2} \tag{3.14}$$

Where f_1 = first attenuation pole (transmission zero)
f_2 = second attenuation pole (transmission zero)

3.3 References

[1] Gardiol, F. (1994). *Microstrip Circuit*, New York: John Wiley & Sons

[2] Hong, J.S., Lancaster, M.J., (2001). *Microstrip Filters for RF/Microwave applications*, New York: John Wiley & Sons

[3] Chang, K. (2000). *RF and Microwave Wireless Systems*, New York: John Wiley & Sons.

[4] Tooley, M. (2002). *Electronics Circuits: Fundamentals and Applications*, (2^{nd} Ed.) Woburn: Newnes.

[5] Rizzi, P.A.(1988). *Microwave Engineering Passive circuit*. New Jersey: Prentice Hall.

[6] Fooks, E.H. & Zakarevicius, R.A. (1990). *Microwave Engineering Using Microstrip Circuits*. Australia: Prentice Hall.

[7] Cohn, S.B, "Parallel-Coupled Transmission Line Resonator Filter", *IRE Trans. Micro. Theory and Tech.,* Vol. 6, Issue 2, 1958, pp.223-231.

[8] Cristal, E. G., Frankel, S., "Hairpin-line and hybrid hairpinline/ half-wave parallel-coupled-line filters", *IEEE Trans. Microw. Theory and Tech.,* Vol. MTT-22, No. 11, 1972, pp.719-728.

[9] Sung, Y., Ahn, C.S., Kim, Y.-S., "Parallel-coupled microstrip bandpass filters with a wide stopband using spur lines", *Microwave and Optical Technology Letters*, Vol. 43, Issue 1, 2004, pp. 9 – 11.

[10] Sagawa, M., Takabashi, K., Makimoto, M., "Miniaturised hairpin resonator filters and their application to receive front-end MIC's", *IEEE Trans. Microwave Theory Tech.* Vol 37, No.12, 1989, pp.1991-1997.

[11] Prigent, G., Rius, E., Le Pennec, F., Le Maguer, S., Le Floch, Ma., Ney, M., "A New Coplanar Band-pass Filter Topology For Improving The Control of Narrowband Band-pass Filter Response", *European Microwave Conference*, Oct. 2001, pp.1 – 4.

[12] Joubert, J., "Spiral Microstrip Resonators For Narrow-Stopband Filters", *IEE Proc. Microw. Antennas Propag*, Vol 150, No.6, 2003, pp.493-496.

Chapter 4 C-Shapes Microstrip Resonator

4.1 Introduction

This chapter introduces a C-shape resonant structure that is theoretically modeled and analyzed to gain insight of its properties. This structure is used to develop quasi-elliptical microstrip microwave filters.

4.2 Theory

Figure 4.1 shows the configuration of C-shape resonator with asymmetric feed line tapping, which improves the rejection as will be shown later. This filter with cross-coupling between nonadjacent resonators is able to create two transmission zeros between the passband and a 3rd transmission zero at higher frequency to achieve high selectivity characteristic, as will be shown later.

The resonator is divided by the input and output feed lines into two sections, l_1 and l_2, as shown in Figure 4.1, where $l_1 + l_2 = \lambda_g/2$, and C_g = capacitance between the two electrically coupled sections. Note $l_1 \neq l_2$.

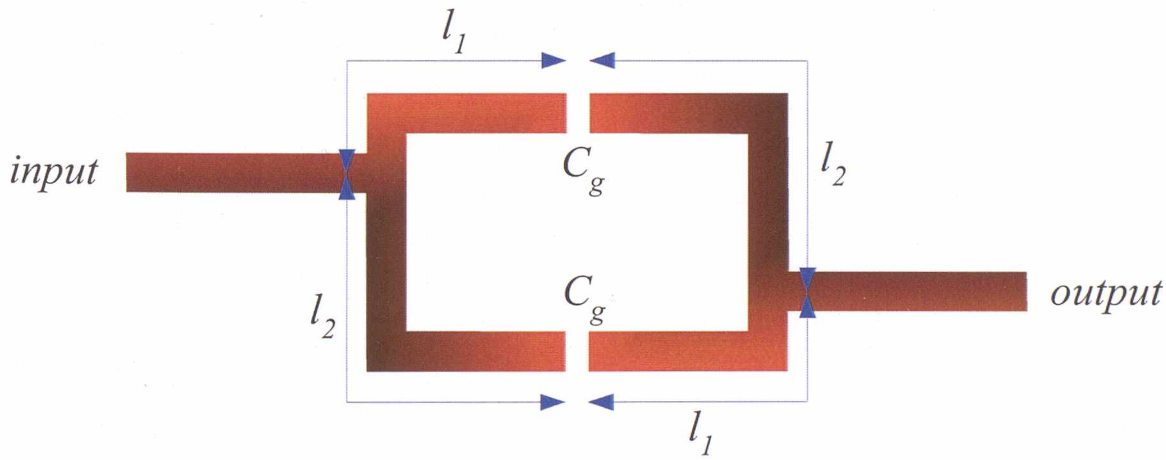

Figure 4. 1 Configuration of C-shape resonator which is divided into two sections.

This configuration represents a shunt circuit with upper and lower sections consisting of l_1, l_2 and C_g. In a lossless case, the ABCD matrix of the *upper section* is

$$\begin{bmatrix} A & B \\ C & D \end{bmatrix}_{upper} = M_1 M_2 M_3 \tag{4.1}$$

Where

$$M_1M_2=\begin{bmatrix}\cos\beta\ell_1 & jZ_0\sin\beta\ell_1\\ jY_0\sin\beta\ell_1 & \cos\beta\ell_1\end{bmatrix}\begin{bmatrix}1 & z_c\\ 0 & 1\end{bmatrix}=\begin{bmatrix}\cos\beta l_1 & z_c\cos\beta l_1+jZ_o\sin\beta l_1\\ jY_o\sin\beta l_1 & jz_cY_o\sin\beta l_1+\cos\beta l_1\end{bmatrix}$$

$$M_1M_2M_3=\begin{bmatrix}\cos\beta l_1 & z_c\cos\beta l_1+jZ_o\sin\beta l_1\\ jY_o\sin\beta l_1 & jz_cY_o\sin\beta l_1+\cos\beta l_1\end{bmatrix}\begin{bmatrix}\cos\beta\ell_2 & jZ_0\sin\beta\ell_2\\ jY_0\sin\beta\ell_2 & \cos\beta\ell_2\end{bmatrix}$$

$$=\begin{bmatrix}\cos\beta l_1\cos\beta l_2+jY_o\sin\beta l_2(z_c\cos\beta l_1+jZ_o\sin\beta l_1) & jZ_o\sin\beta\ell_2\cos\beta\ell_1+\cos\beta\ell_2(z_c\cos\beta l_1+jZ_o\sin\beta l_1)\\ jY_o\sin\beta l_1\cos\beta l_2-jY_o\sin\beta l_2(jz_cY_o\sin\beta l_1+\cos\beta l_1) & -\sin\beta l_1\sin\beta l_2+\cos\beta l_2(jz_cY_o\sin\beta l_1+\cos\beta l_1)\end{bmatrix}$$

(4.2)

where β= propagation constant

ω= angular frequency

$z_c=1/j\omega C_g$ = impedance of the gap capacitance

$Z_o=1/Y_o$ = characteristic impedance of the resonator

The ABCD matrix of the *lower section* is

$$\begin{bmatrix}A & B\\ C & D\end{bmatrix}_{lower}=M_3M_2M_1 \tag{4.3}$$

where

$$M_3M_2=\begin{bmatrix}\cos\beta\ell_2 & jZ_0\sin\beta\ell_2\\ jY_0\sin\beta\ell_2 & \cos\beta\ell_2\end{bmatrix}\begin{bmatrix}1 & z_c\\ 0 & 1\end{bmatrix}=\begin{bmatrix}\cos\beta l_2 & z_c\cos\beta l_1+jZ_o\sin\beta l_2\\ jY_o\sin\beta l_2 & jz_cY_o\sin\beta l_2+\cos\beta l_2\end{bmatrix}$$

$$M_3M_2M_1=\begin{bmatrix}\cos\beta l_2 & z_c\cos\beta l_1+jZ_o\sin\beta l_2\\ jY_o\sin\beta l_2 & jz_cY_o\sin\beta l_2+\cos\beta l_2\end{bmatrix}\begin{bmatrix}\cos\beta\ell_1 & jZ_0\sin\beta\ell_1\\ jY_0\sin\beta\ell_1 & \cos\beta\ell_1\end{bmatrix}$$

$$=\begin{bmatrix}\cos\beta l_1\cos\beta l_2+jY_o\sin\beta l_1(z_c\cos\beta l_2+jZ_o\sin\beta l_2) & jZ_o\sin\beta\ell_1\cos\beta\ell_2+\cos\beta\ell_1(z_c\cos\beta l_2+jZ_o\sin\beta l_2)\\ jY_o\sin\beta l_2\cos\beta l_1-jY_o\sin\beta l_1(jz_cY_o\sin\beta l_2+\cos\beta l_2) & -\sin\beta l_1\sin\beta l_2+\cos\beta l_1(jz_cY_o\sin\beta l_2+\cos\beta l_2)\end{bmatrix}$$

(4.4)

The Y-parameters of the upper and lower sections are obtained from (4.2) and (4.4) and given by

$$\begin{bmatrix}Y_{11} & Y_{12}\\ Y_{21} & Y_{22}\end{bmatrix}=\begin{bmatrix}D_j/B_j & (B_jC_j-A_jD_j)/B_j\\ -1/B_j & A_j/B_j\end{bmatrix} \tag{4.5}$$

Where j = *upper* or *lower* is for upper or lower sections.

The Y-parameters of the *upper section* are

$$y_{11u} = \frac{D}{B} = \frac{-\sin\beta l_1 \sin\beta l_2 + \cos\beta l_2 (jz_c Y_o \sin\beta l_1 + \cos\beta l_1)}{jZ_o \sin\beta\ell_2 \cos\beta\ell_1 + \cos\beta\ell_2 (z_c \cos\beta l_1 + jZ_o \sin\beta l_1)} \tag{4.6a}$$

$$y_{12u} = \frac{BC - AD}{B}$$

$$= \frac{\left\{\begin{array}{l} (jZ_o \sin\beta\ell_2 \cos\beta\ell_1 + \cos\beta\ell_2 (z_c \cos\beta l_1 + jZ_o \sin\beta l_1))(jY_o \sin\beta l_1 \cos\beta l_2 - jY_o \sin\beta l_2 (jz_c Y_o \sin\beta l_1 + \cos\beta l_1)) \\ -(\cos\beta l_1 \cos\beta l_2 + jY_o \sin\beta l_2 (z_c \cos\beta l_1 + jZ_o \sin\beta l_1))(-\sin\beta l_1 \sin\beta l_2 + \cos\beta l_2 (jz_c Y_o \sin\beta l_1 + \cos\beta l_1)) \end{array}\right\}}{jZ_o \sin\beta\ell_2 \cos\beta\ell_1 + \cos\beta\ell_2 (z_c \cos\beta l_1 + jZ_o \sin\beta l_1)} \tag{4.6b}$$

$$y_{21u} = \frac{-1}{jZ_o \sin\beta\ell_2 \cos\beta\ell_1 + \cos\beta\ell_2 (z_c \cos\beta l_1 + jZ_o \sin\beta l_1)} \tag{4.6c}$$

$$y_{22u} = \frac{\cos\beta l_1 \cos\beta l_2 + jY_o \sin\beta l_2 (z_c \cos\beta l_1 + jZ_o \sin\beta l_1)}{jZ_o \sin\beta\ell_2 \cos\beta\ell_1 + \cos\beta\ell_2 (z_c \cos\beta l_1 + jZ_o \sin\beta l_1)} \tag{4.6d}$$

The Y-parameters of the *lower section* are

$$y_{11L} = \frac{-\sin\beta l_1 \sin\beta l_2 + \cos\beta l_1 (jz_c Y_o \sin\beta l_2 + \cos\beta l_2)}{jZ_o \sin\beta\ell_1 \cos\beta\ell_2 + \cos\beta\ell_1 (z_c \cos\beta l_2 + jZ_o \sin\beta l_2)} \tag{4.7a}$$

$$y_{12L} = \frac{\left\{\begin{array}{l} (jZ_o \sin\beta\ell_1 \cos\beta\ell_2 + \cos\beta\ell_1 (z_c \cos\beta l_2 + jZ_o \sin\beta l_2))\times \\ (jY_o \sin\beta l_2 \cos\beta l_1 - jY_o \sin\beta l_1 (jz_c Y_o \sin\beta l_2 + \cos\beta l_2)) \\ -(\cos\beta l_1 \cos\beta l_2 + jY_o \sin\beta l_1 (z_c \cos\beta l_2 + jZ_o \sin\beta l_2))(-\sin\beta l_1 \sin\beta l_2 + \cos\beta l_1 (jz_c Y_o \sin\beta l_2 + \cos\beta l_2)) \end{array}\right\}}{jZ_o \sin\beta\ell_1 \cos\beta\ell_2 + \cos\beta\ell_1 (z_c \cos\beta l_2 + jZ_o \sin\beta l_2)} \tag{4.7b}$$

$$y_{21L} = \frac{-1}{jZ_o \sin\beta\ell_1 \cos\beta\ell_2 + \cos\beta\ell_1 (z_c \cos\beta l_2 + jZ_o \sin\beta l_2)} \tag{4.7c}$$

$$y_{22L} = \frac{\cos\beta l_1 \cos\beta l_2 + jY_o \sin\beta l_1 (z_c \cos\beta l_2 + jZ_o \sin\beta l_2)}{jZ_o \sin\beta\ell_1 \cos\beta\ell_2 + \cos\beta\ell_1 (z_c \cos\beta l_2 + jZ_o \sin\beta l_2)} \tag{4.7d}$$

Since $l_1 + l_2 = \lambda_g / 2$, the trigonometric identities can be simplified to

$$\sin\beta l_1 \sin\beta l_2 = \sin^2 \beta l_1 \tag{4.8a}$$

$$\sin\beta l_1 \cos\beta l_2 = -\sin\beta l_1 \cos\beta l_1 \tag{4.8b}$$

$$\sin\beta l_2 \cos\beta l_1 = \sin\beta l_1 \cos\beta l_1 \tag{4.8c}$$

$$\cos\beta l_1 \cos\beta l_2 = -\cos^2 \beta l_1 \tag{4.8d}$$

The simplified Y-parameters of the *upper section* is

$$y_{11u} = \frac{1 + jz_c Y_o \sin\beta l_1 \cos\beta l_1}{Z_o \cos^2 \beta l_1} \tag{4.9a}$$

$$y_{12u} = \frac{1}{z_c \cos^2 \beta l_1} \tag{4.9b}$$

$$y_{21u} = \frac{1}{z_c \cos^2 \beta l_1} \tag{4.9c}$$

$$y_{22u} = \frac{1 - jz_c Y_o \sin\beta l_1 \cos\beta l_1}{Z_o \cos^2 \beta l_1} \tag{4.9d}$$

The simplified Y-parameters of the *lower section* are

$$y_{11L} = \frac{1 - jz_c Y_o \sin\beta l_1 \cos\beta l_1}{Z_o \cos^2 \beta l_1} \tag{4.10a}$$

$$y_{12L} = \frac{1}{z_c \cos^2 \beta l_1} \tag{4.10b}$$

$$y_{21L} = \frac{1}{z_c \cos^2 \beta l_1} \tag{4.10c}$$

$$y_{22L} = \frac{1 + jz_c Y_o \sin\beta l_1 \cos\beta l_1}{Z_o \cos^2 \beta l_1} \tag{4.10d}$$

The total Y-parameter of the whole circuit is given by

$$\begin{bmatrix} Y_{11} & Y_{12} \\ Y_{21} & Y_{22} \end{bmatrix} = \begin{bmatrix} Y_{11} & Y_{12} \\ Y_{21} & Y_{22} \end{bmatrix}_{upper} + \begin{bmatrix} Y_{11} & Y_{12} \\ Y_{21} & Y_{22} \end{bmatrix}_{lower} \tag{4.11}$$

where

$$y_{11} = \frac{2}{z_c \cos^2 \beta l_1} \tag{4.12a}$$

$$y_{12} = \frac{2}{z_c \cos^2 \beta l_1} \tag{4.12b}$$

$$y_{21} = \frac{2}{z_c \cos^2 \beta l_1} \tag{4.12c}$$

$$y_{22} = \frac{2}{Z_o \cos^2 \beta l_1} \tag{4.12d}$$

This leads to the calculation of insertion-loss S_{21} of the circuit, which is given as

$$S_{21} = \frac{-2Y_{21}Y_o}{(Y_{11} + Y_o)(Y_{22} + Y_o) - Y_{12}Y_{21}}$$

$$= \frac{4z_c Y_o \cos\beta l_1 \cos\beta l_2}{(2 - z_c Y_o \cos\beta l_1 \cos\beta l_2)^2 - 4} \tag{4.13}$$

The transmission zero (attenuation poles) can be found by letting $S_{21} = 0$, which gives

$$4z_c Y_o \cos\beta l_1 \cos\beta l_2 = 0 \tag{4.14}$$

By substituting $\beta = 2\pi f \sqrt{\varepsilon_{eff}} / c$ into (4.14), this gives the relationship between tapping positions and transmission zero as below

$$f_1 = \frac{nc}{4l_2\sqrt{\varepsilon_{eff}}} \tag{4.15a}$$

and $$f_2 = \frac{nc}{4l_1\sqrt{\varepsilon_{eff}}} \tag{4.15b}$$

Where f_1 = frequency at first attenuation pole

f_2 = frequency at second attenuation pole

ε_{eff} = effective dielectric constant

n = mode number for n = 1, 3, 5...

c = speed of light in free space = 3×10^8 m/s

Therefore, at transmission zero, S_{21} = 0, there is maximum rejection. On the other hand, when $l_1 = l_2$, there is no transmission zero (attenuation pole).

4.2 Verification of C-Shape Resonator Theoretical Model

In this section, the validity of Equations (4.15a) and (4.15b), defined for the resonant structure in Figure 4.1, are verified using a power EM simulator from Agilent Technologies, i.e. ADS-momentum, that uses method of moment. The schematic of C-shape resonator is shown in Figure 4.2. For this C-shape resonator, the simulated frequencies and phase responses for $l_1 = l_2$ = 15.63 mm, and $l_1 \neq l_2$, e.g. l_1 = 13.63 mm and l_2 = 17.63 mm, are shown in Figure 4.3 and Figure 4.4, respectively.

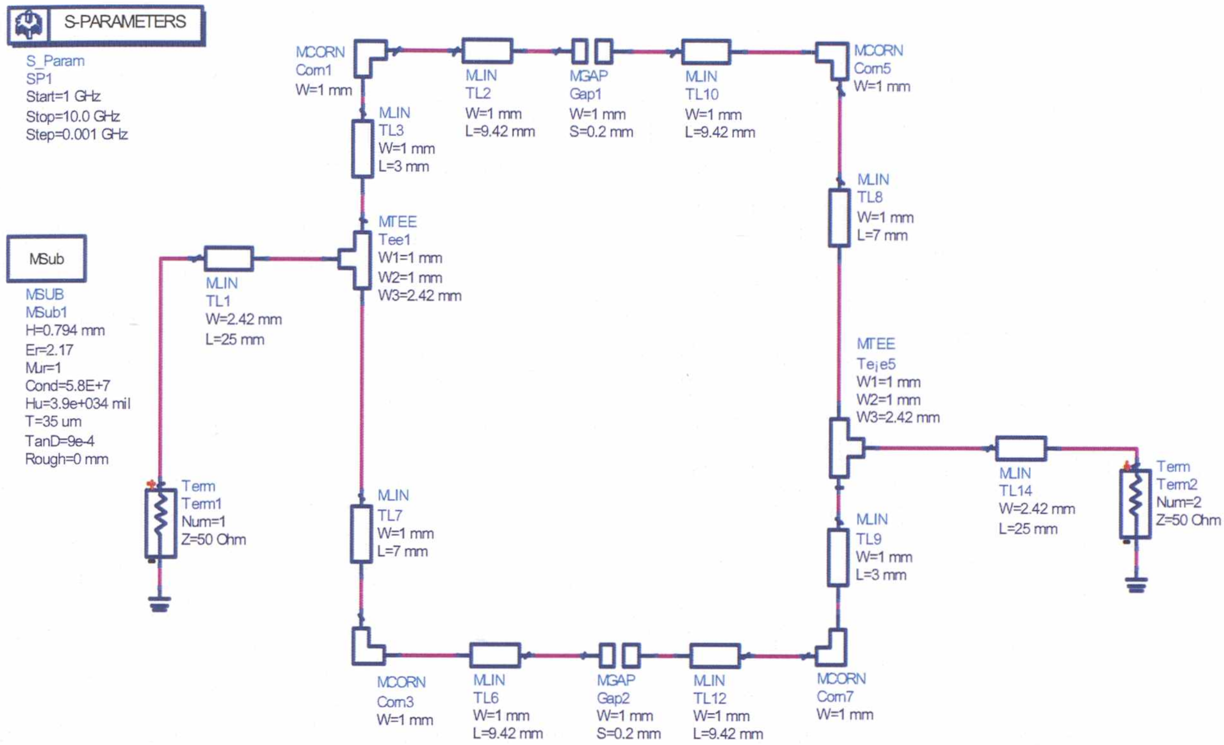

Figure 4. 2 The schematic of C-shape resonator

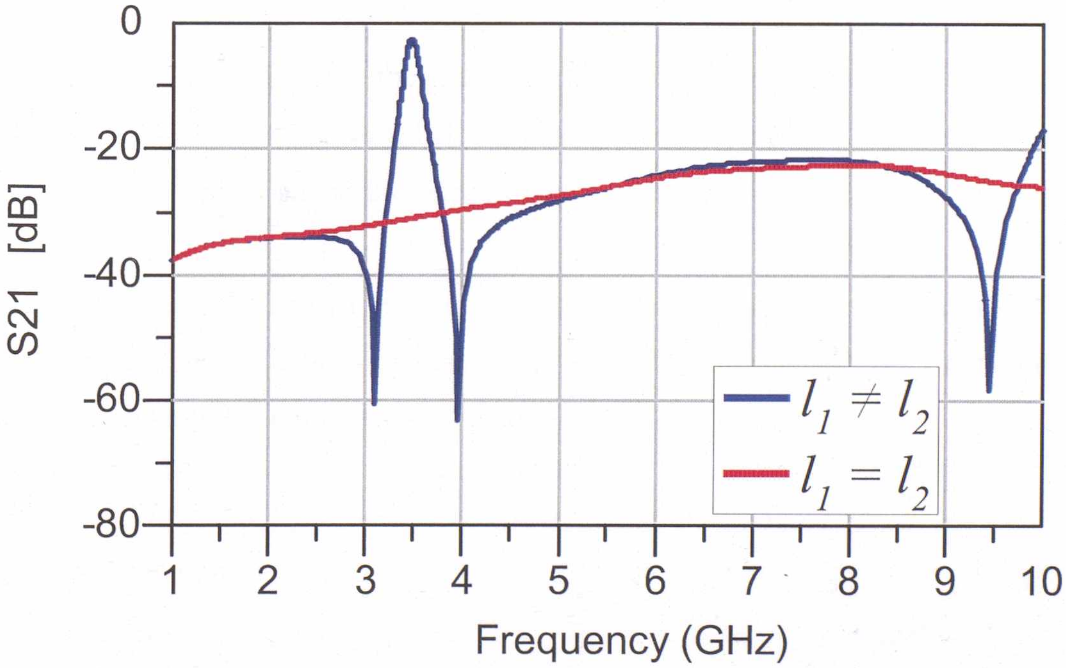

Figure 4. 3 The simulated frequency responses for $l_1 = l_2$ and $l_1 \neq l_2$.

Figure 4.3 shows the quasi-elliptical function filter obtained has the centre frequency and the upper and lower transmission zero poles located at 3.465 GHz, 3.093 GHz and 3.953 GHz, respectively.

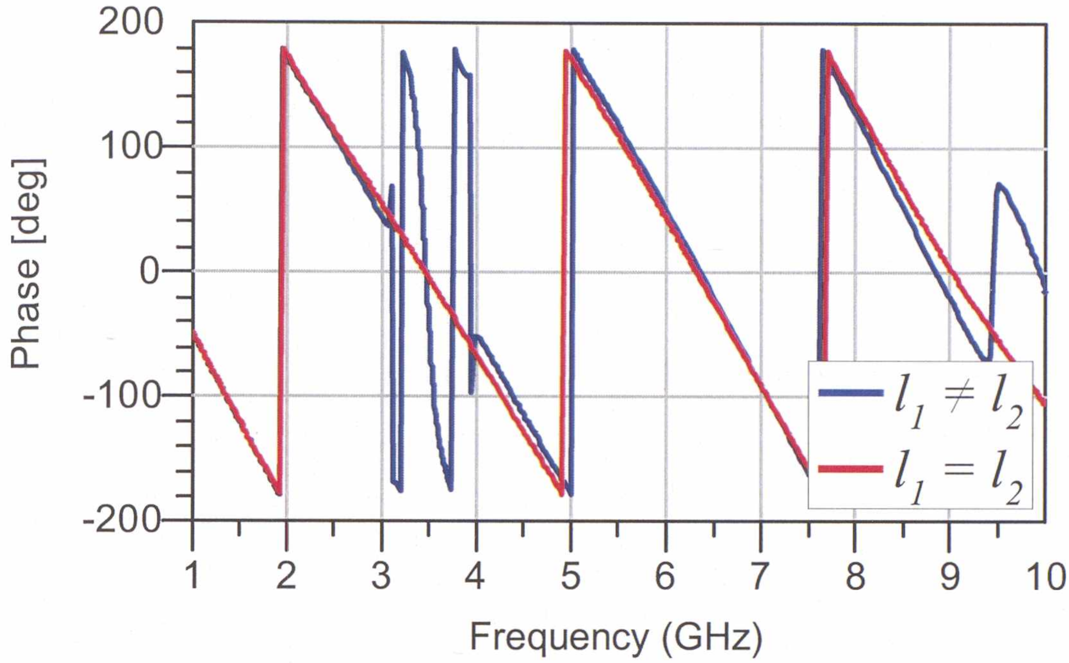

Figure 4. 4 The simulated phase responses of S_{21} for $l_1 = l_2$ and $l_1 \neq l_2$.

From the simulated response in Figure 4.4, it can be seen that for the symmetrical input/output tapping feed lines (i.e. $l_1 = l_2$), the phase changes linearly between approximately 2-5 GHz range, therefore no transmission zeros occur in this case. In addition, at the passband centre frequency of 3.465 GHz the phase is zero degrees. However, for the case of $l_1 \neq l_2$, the phase changes erratically between approximately 3-4 GHz. It should be pointed out that the phase changes near the passband decreases linearly but very sharply and at the centre frequency it is zero degree.

For the schematic shown in Figure 4.2, the calculated transmission zero locations can be obtained from Equations (4.15a) and (4.15b). The following substrate parameters were used to calculate the transmission zeros:

$\varepsilon_r = 2.17$

$h = 0.794$ mm

$T = 35$ μm

$\sigma = 5.8 \times 10^{7}$ S/m

$\tan \delta = 9 \times 10^{-4}$

$w = 1$ mm (line width)

$f_o = 3.465$ GHz

$l_1 = 13.63$ mm

$l_2 = 17.63$ mm

The data obtained from LineCal analysis are:

$Z_o = 83.19\ \Omega$

$\lambda_g/2 = 32.61\,mm$

$\varepsilon_{eff} = 1.76$

It is noted that $l_1 + l_2 = \lambda_g/2 = 31.26\,mm$ from the schematic in Figure 4.2. However, from LineCal, part of ADS, $\lambda_g/2 = 32.61\,mm$.

Hence, the percentage error in $\lambda_g/2 = [(32.61 - 31.26)/31.26] \times 100\% = 4.32\%$

From Equations (4.15a) and (4.15b), where $n = 1$,

$$f_1 = \frac{nc}{4l_2\sqrt{\varepsilon_{eff}}} = \frac{1 \times 3 \times 10^8}{4 \times 17.63 \times 10^{-3}\sqrt{1.76}} = 3.207\ GHz$$

$$f_2 = \frac{nc}{4l_1\sqrt{\varepsilon_{eff}}} = \frac{1 \times 3 \times 10^8}{4 \times 13.63 \times 10^{-3}\sqrt{1.76}} = 4.148\ GHz$$

Table 4.1 shows the comparison of simulated and calculated transmission zero locations and the error in percentage for both results.

Transmission zero	*Simulated* (GHz)	*Calculated* (GHz)	*Error relative to simulation* (%)
f_1 (1st pole)	3.093	3.207	3.69
f_2 (2nd pole)	3.953	4.148	4.93

Table 4. 1 The simulated and calculated transmission zero locations

The above analysis indicates that the worst-case error obtained using Equations (4.15a) and (4.15b) is around 5%. This discrepancy is attributed to the lossless modelling in calculation by using Equations (4.15a) and (4.15b). It should be noted that the total length of $l_1 = l_2$ in the schematic does not include the four corner sections. Hence, there is a very small discrepancy of 4.32% between the schematic and LineCal results for $\lambda_g/2$. This discrepancy contributes to the error as shown in Table 4.1.

However, the above-calculated results prove that the theoretical analysis in section 4.1 is valid.

4.3 Compact C-Shape

A more compact filter is derived from the C-shape structure in Figure 4.1 using two open-loop ring resonators as illustrated in Figure 4.5, where g is the capacitive coupling between the transmission line open-ends.

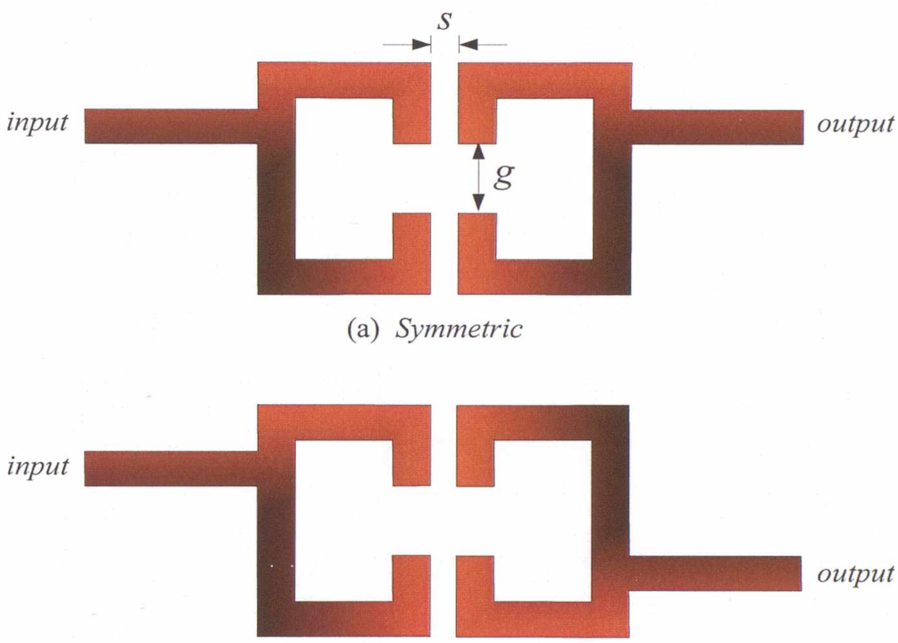

(a) *Symmetric*

(b) *Asymmetric*

Figure 4. 5 Compact C-shape with symmetric and asymmetric tapped feed lines.

For the symmetric case in Figure 4.5(a), the simulated frequency response for one configuration of feed line location is shown in Figure 4.6. This result shows that the filter response selectivity is moderate. The schematic of Figure 4.5(a) with one configuration of feed line location is shown in Figure 4.7.

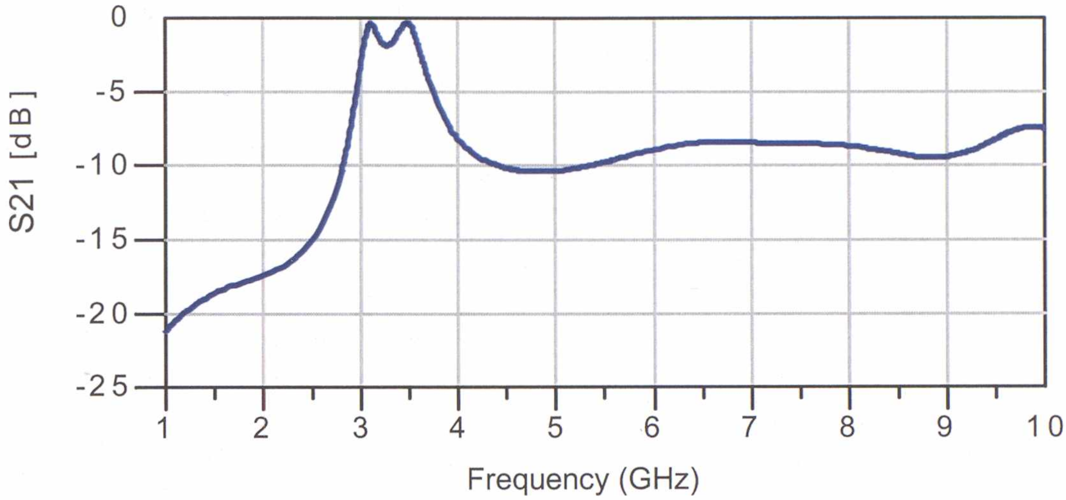

Figure 4. 6 The simulated frequency response for Figure 4.5 (a).

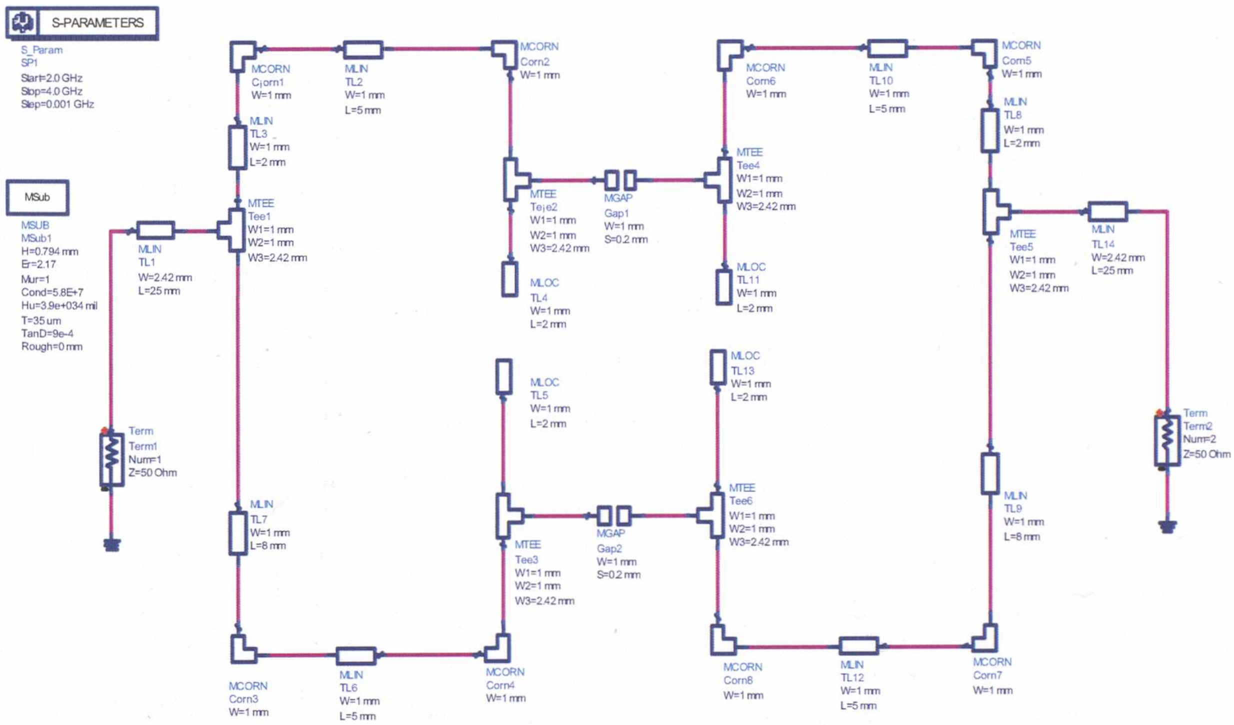

Figure 4. 7 The schematic of compact C-shape resonator.

In contrast, for the asymmetric case in Figure 4.5(b), the simulated frequency response for one configuration of feed line location is shown in Figure 4.8.

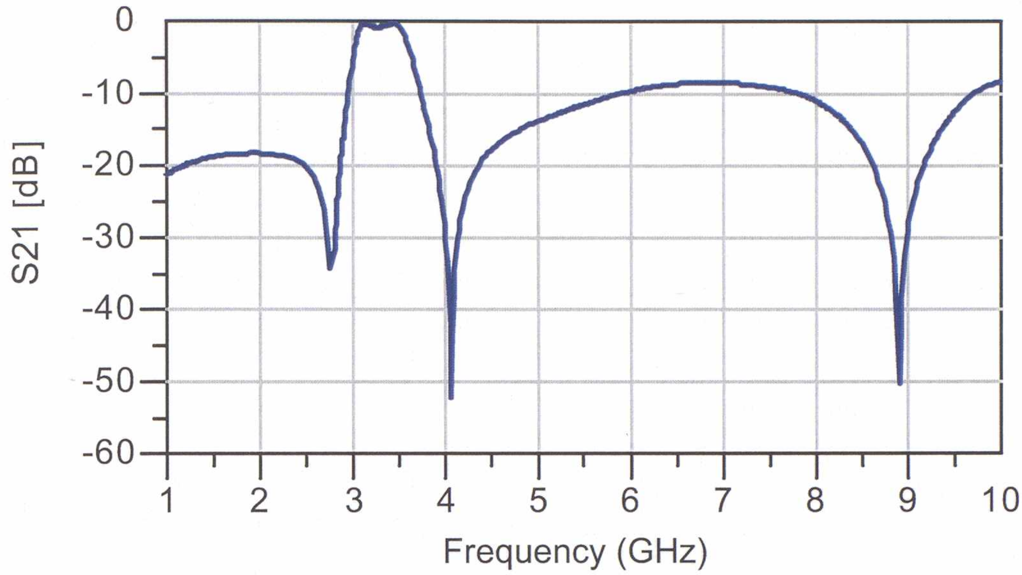

Figure 4. 8 The simulated frequency response for Figure 4.5 (b).

In this case the filter response has two poles (transmission zeros) on either side of the passband making the filter highly selective compared to the symmetric case. Hence, the following analysis will be for only the asymmetric compact C-shape filter except for the symmetric case of $l_1 = l_2$.

In Figure 4.5(b), the resonator has the same dimension as Figure 4.1 except that the open ends have been bending by 90° inwards and with coupling gap g within the two open ends. The locations of the transmission zero can be predicted using Equations (4.15a) and (4.15b). The schematic diagram of this Figure 4.5(b) is shown in Figure 4.9 while its simulated frequencies response for $l_1 = l_2 = 15.63$ mm and $l_1 \neq l_2$, i.e. $l_1 = 13.63$ mm and $l_2 = 17.63$ mm are shown in Figure 4.10. From this figure, it is shown that the passband centre frequency and the upper and lower transmission zero poles are at 3.288 GHz, 2.909 GHz and 3.803 GHz, respectively.

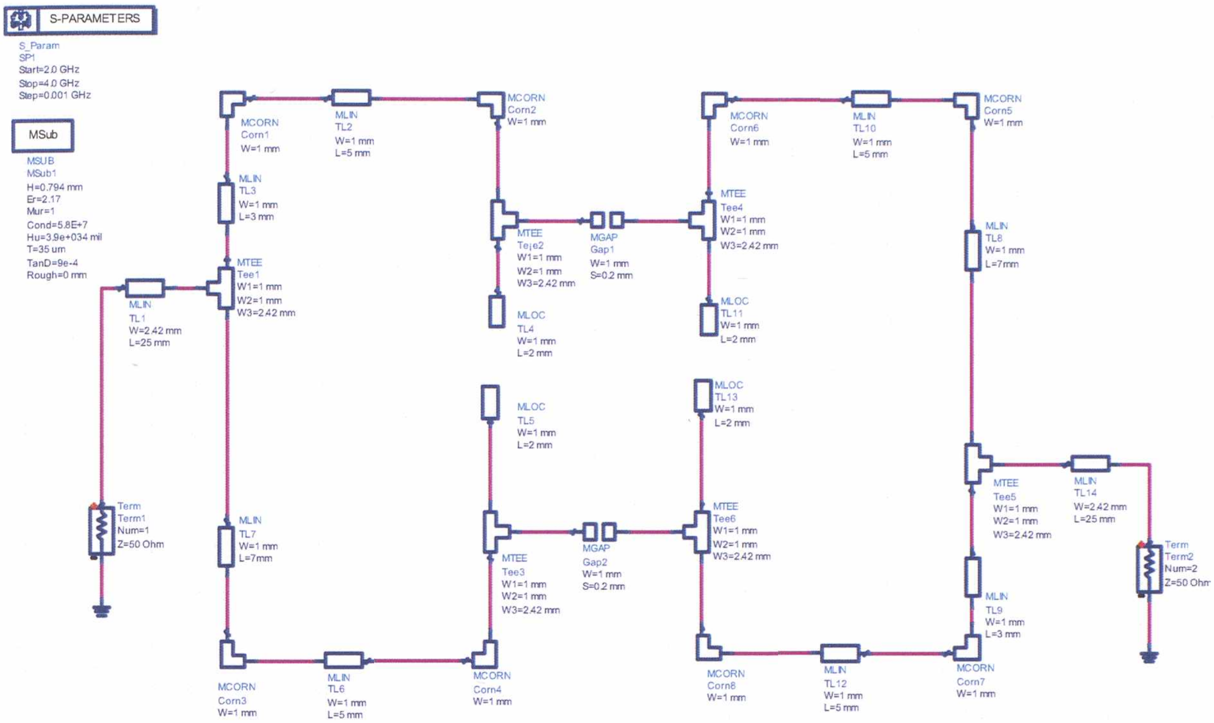

Figure 4. 9 The schematic of compact C-shape resonator.

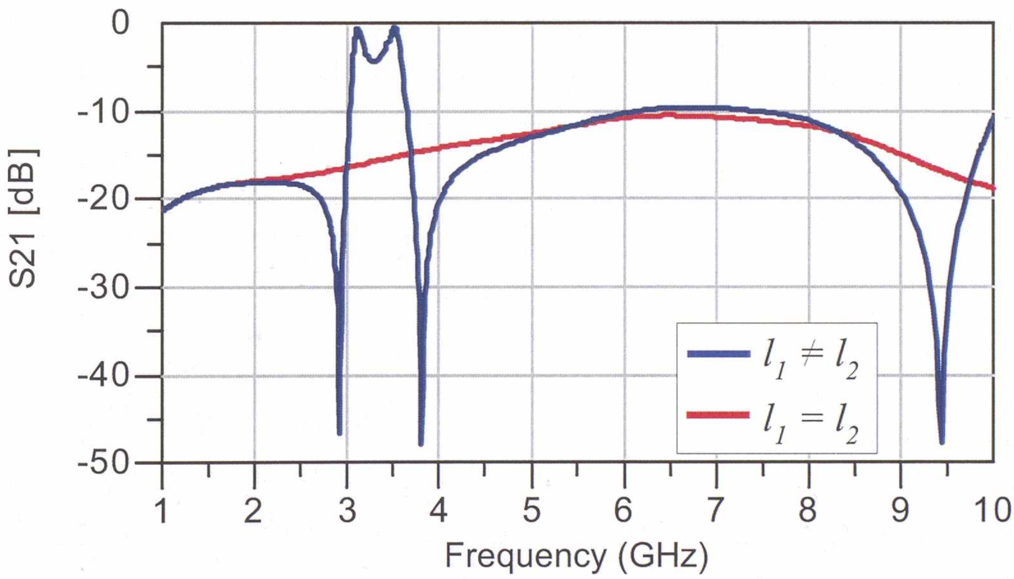

Figure 4. 10 The simulated frequencies response for $l_1 = l_2$ and $l_1 \neq l_2$.

For the schematic shown in Figure 4.9, the calculated transmission zero locations can be obtained from Equations (4.15a) and (4.15b). The following parameters were used to calculate the transmission zeros:

$\varepsilon_r = 2.17$

$h = 0.794$ mm

$T = 35$ µm

$\sigma = 5.8 \times 10^{7}$ S/m

$tan\ \delta = 9 \times 10^{-4}$

$w = 1$ mm (line width)

$f_o = 3.288$ GHz

$l_1 = 13.63$ mm

$l_2 = 17.63$ mm

The data obtained from LineCal analysis are:

$Z_o = 83.19\ \Omega$

$\lambda_g/2 = 34.36\ mm$

$\varepsilon_{eff} = 1.76$

It is noted that $l_1 + l_2 = \lambda_g/2 = 31.26\ mm$ from the schematic in Figure 4.9. However, from LineCal, $\lambda_g/2 = 34.36\ mm$.

Hence, the percentage error in $\lambda_g/2 = [(34.36 - 31.26)/31.26] \times 100\% = 9.92\%$

From Equations (4.15a) and (4.15b), where $n = 1$,

$$f_1 = \frac{nc}{4l_2\sqrt{\varepsilon_{eff}}} = \frac{1 \times 3 \times 10^8}{4 \times 17.63 \times 10^{-3}\sqrt{1.76}} = 3.207\ GHz$$

$$f_2 = \frac{nc}{4l_1\sqrt{\varepsilon_{eff}}} = \frac{1 \times 3 \times 10^8}{4 \times 13.63 \times 10^{-3}\sqrt{1.76}} = 4.148\ GHz$$

Table 4.2 shows the comparison of simulated and calculated transmission zero locations and the error in percentage for both results.

The above analysis indicates that the worst-case error obtained using Equations (4.15a) and (4.15b) is about 10%. This discrepancy is attributed to the lossless modelling in calculation by using Equations (4.15a) and (4.15b). It should be noted that the total length of $l_1 = l_2$ in the schematic does not include the eight corners sections as well as the coupling gap g. The theory in section 4.1 does not account for coupling gap g. Hence, there is a discrepancy of 9.92% between the schematic and LineCal results for $\lambda_g/2$ which contribute to the errors in Table 4.2. Despite this, the error between simulation and calculation are around 10%.

Transmission zero	*Simulated* (GHz)	*Calculated* (GHz)	*Error relative to simulation* (%)
f_1 (1st pole)	2.909	3.208	10.28
f_2 (2nd pole)	3.803	4.149	9.10

Table 4. 2 The simulated and calculated transmission zero locations

The analysis of feed line tapping positions was done next to determine the worst-case error. Table 4.3 shows the relative tapping positions resonance frequency and the $\lambda_g/2$ values obtained from LineCal.

l_1 (mm)	l_2 (mm)	f_o (GHz)	ε_{eff}	Z_o (Ω)	$\lambda_g/2$ from LineCal (mm)	$\lambda_g/2$ error relative to schematic (%)
11.63	19.63	3.242	1.759	83.19	34.85	11.48
12.63	18.63	3.233	1.759	83.19	34.95	11.80
13.63	17.63	3.288	1.759	83.19	34.36	9.92
14.63	16.63	3.280	1.759	83.19	34.45	10.20

Table 4. 3 The $\lambda_g/2$ error between LineCal and schematic results.

The Table 4.3 shows that the tapping position affects the centre frequency slightly, however the worst-case error in $\lambda_g/2$ when compared with 31.26 mm obtained from ADS schematic is 11.80%. This can be accounted to the corners section and the coupling gap g as mentioned earlier.

Tapping position		*Simulated results*			*Calculated results*		*Error relative to simulated* (%)		
l_1 (mm)	l_2 (mm)	f_o (GHz)	f_1 (GHz)	f_2 (GHz)	f_1 (GHz)	f_2 (GHz)	f_1 (GHz)	f_2 (GHz)	*Average error*
11.63	19.63	3.242	2.650	4.394	2.881	4.862	8.72	10.65	9.7
12.63	18.63	3.233	2.800	4.052	3.035	4.477	8.39	10.49	9.4
13.63	17.63	3.288	2.909	3.803	3.208	4.149	10.28	9.10	9.7
14.63	16.63	3.280	3.034	3.608	3.400	3.865	12.06	7.12	9.6

Table 4. 4 Comparison of error between calculated and simulated f_1 and f_2 results for different tapping lines positions.

Table 4.4 shows the various tapping positions resonance frequency with the upper and lower pole frequencies (i.e. f_1 and f_2) and the errors of the upper and lower pole frequencies between simulated and calculated.

It can be seen from Table 4.4 that as l_1 increases and as l_2 decreases, noting that $l_1 + l_2 = \lambda_g/2$, the error of lower pole frequency, f_1 increases but the upper pole frequency, f_2 decreases. The average combined error for both poles is around 9.7% at maximum.

4.3.1 Analysis of Compact C-Shape Structure

The structure in Figure 4.5(b) is investigated further in terms of the relationships between input/output feed line positions. The locations of the transmission zeros and the value of insertion loss (*IL*) as well as return loss (*RL*) corresponding to various dimension of l_1 and l_2 are shown in Table 4.5.

l_1 (mm)	l_2 (mm)	f_o (GHz)	f_1 (GHz)	f_2 (GHz)	*IL* (dB)	*RL* (dB)
11.63	19.63	3.242	2.650	4.394	0.285	18.526
12.63	18.63	3.233	2.800	4.052	0.357	9.217
13.63	17.63	3.288	2.909	3.803	3.559	2.222
14.63	16.63	3.280	3.034	3.608	8.211	0.492

Table 4. 5 Dimension of l_1 and l_2, and the corresponding locations of transmission zeros, the insertion-loss (IL) as well as the return-loss (RL).

The respective simulated frequency responses of various l_1 parameters are shown in Figure 4.11 while Figure 4.12 shows the return-loss (*RL*) for various value of l_1.

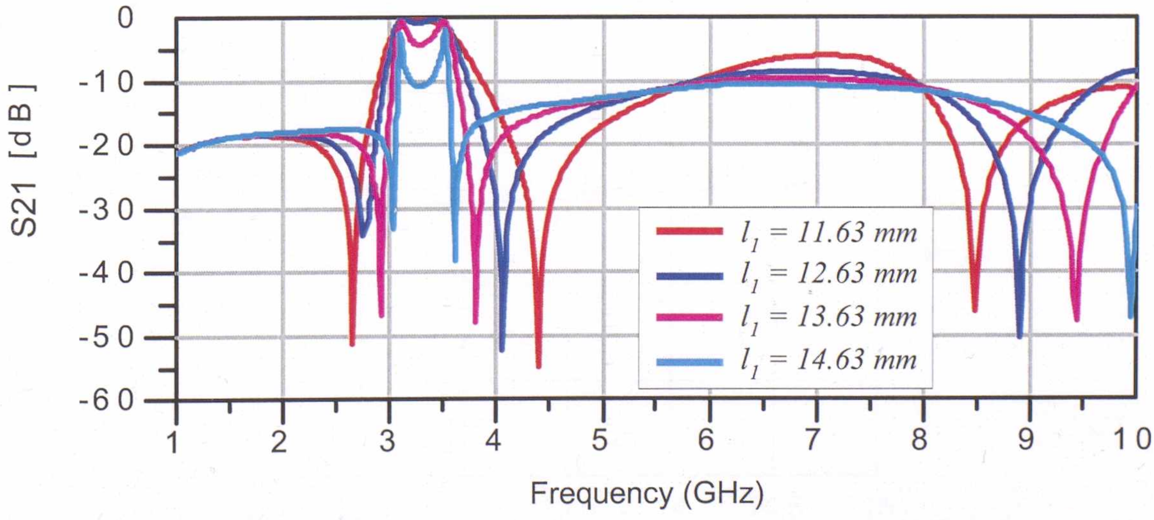

Figure 4. 11 The simulated frequency response of compact C-shape resonator for various length of l_1.

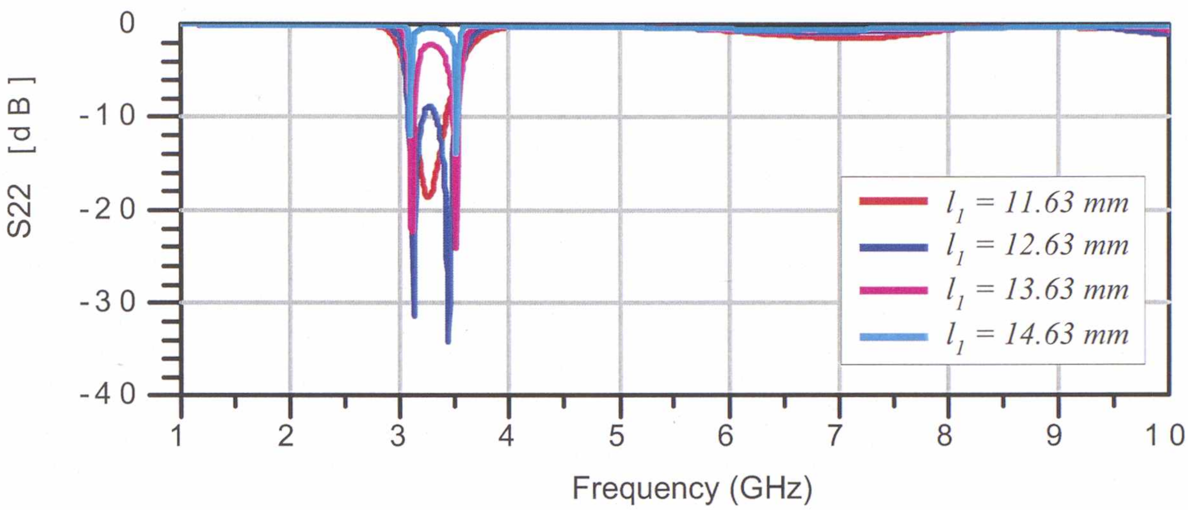

Figure 4. 12 The simulated return-loss of compact C-shape resonator for various l_1.

The results in Table 4.5 are shown in graphical form in Figure 4.13 and Figure 4.14 to illustrate the effect of changes by l_1.

This analysis shows that when l_1 decreases (or l_2 increases, the tapping positions move away from the centre), the insertion-loss decreases while return-loss increases; on the other hand, the location of f_1 pole is shifted to lower frequency while the location of f_2 pole is shifted to a higher frequency. Although the return-loss is reduced with the increase of l_1, however from Figure 4.11, it is shown that the coupling between the resonators also increases which results in a narrower and sharp response, but the passband dip or valley becomes significant. This renders the resonator practically unsuitable for real applications.

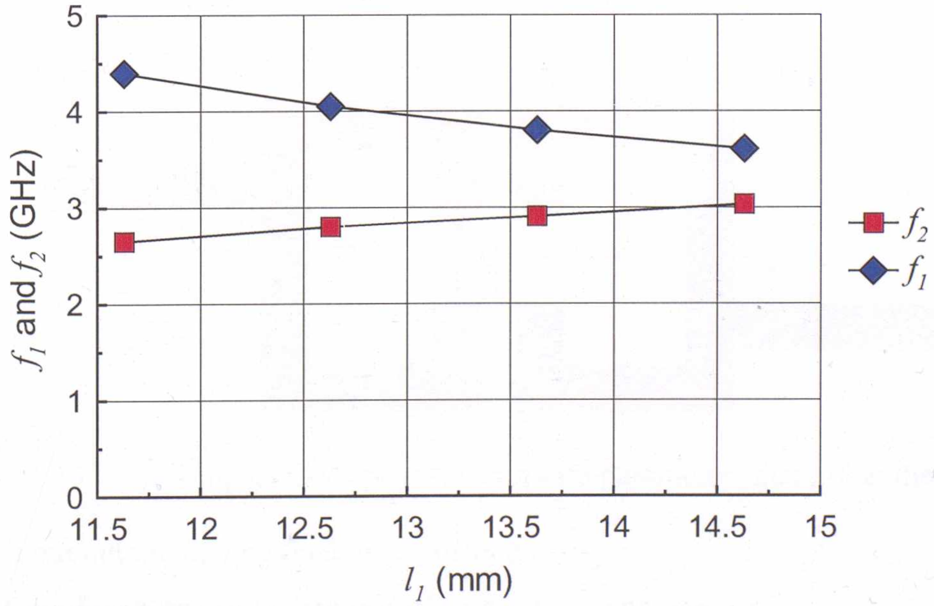

Figure 4. 13 Location of transmission zeros f_1 and f_2 corresponding to various l_1.

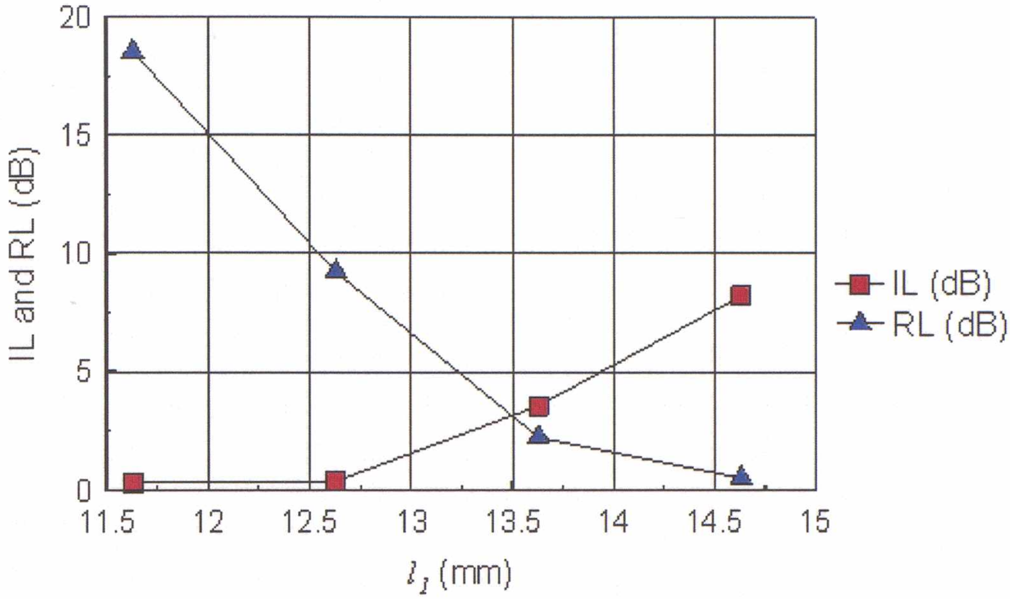

Figure 4. 14 The return-loss and insertion-loss corresponding to various l_1.

In conclusion, Figure 4.11 indicates that the tapping positions, which are l_1 and l_2, affect the location of the two transmissions zero. The optimum positions for l_1 and l_2 are at l_1 = 12.63 mm and l_2 = 18.63 mm because the sharpness of the skirt, i.e. rejection, is much better while the insertion-loss is relatively low, i.e. 0.357 dB, and the return-loss is 9.217 dB, as given in Table 4.5.

4.3.2 Effect of Coupling in the Compact C-Shape Structure

In this section, the significance of the electromagnetic coupling in the compact C-shape resonator is explored by varying the following parameters:

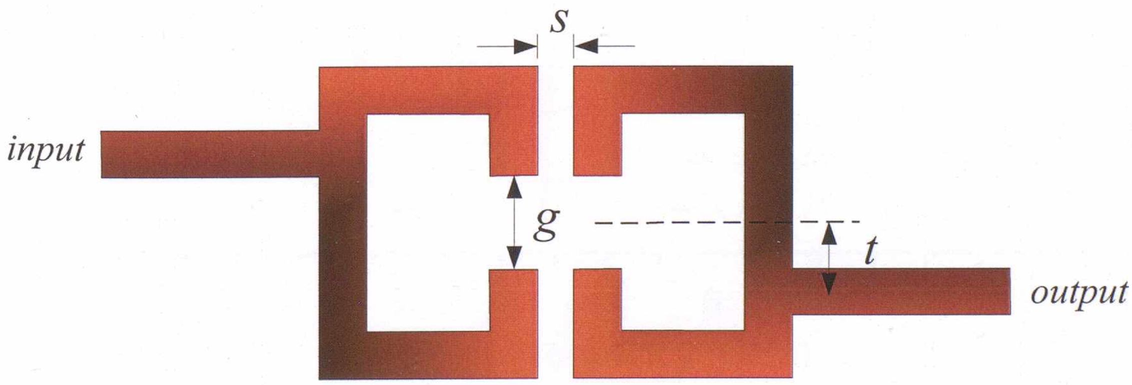

Figure 4. 15 Compact C-shape resonator with parameters that affect the coupling.

Input/output tapping feed lines position t

Coupling between the resonator's open ends with gap g

Coupling between the sides of the resonator's open ends with gap s

4.3.2.1 Effect of Changing Input/output Tapping Feed Lines Positions

Figure 4.16 shows the over coupled, critically coupled and no coupled cases when l_1 are 11.63 mm, 14.63 mm, and 15.63 mm (i.e. $l_1 = l_2$), respectively.

It is noticed that when the tapping position moves towards the centre, an over coupled condition occurs. The transmission zeros move closer to the passband which creates a high selectivity characteristic. However, the external quality factor Q_E becomes larger and causes a trough or dip within the passband. When the insertion-loss is high, it implies over coupled condition which is given by [1]

$$k > \frac{1}{Q_U} + \frac{1}{Q_E} \tag{4.16}$$

Where k = coupling coefficient

Q_U = unloaded-Q

Q_E = external-Q

and $$Q_E = \frac{f_o}{\Delta f_{3dB}} \tag{4.17}$$

Where Δf_{3dB} = 3 dB bandwidth

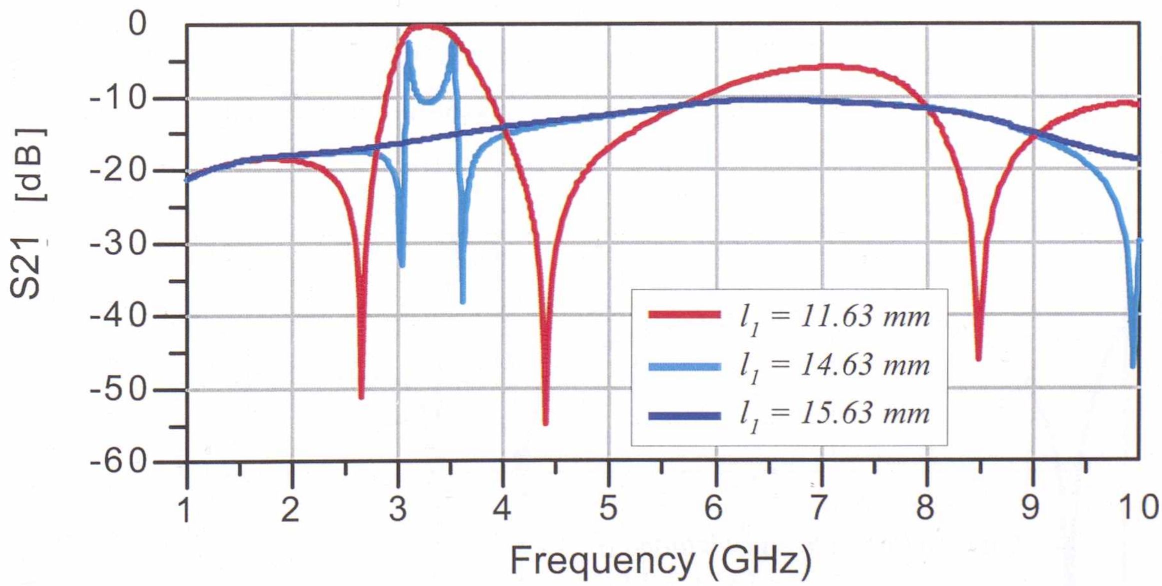

Figure 4. 16 Simulated frequency responses for over-coupled, critically coupled and no coupled cases.

Figure 4.17 shows that when the distance of *t* increases, i.e. input/output tap point is further from the centre, the stronger the coupling or the lower the external quality factor Q_E.

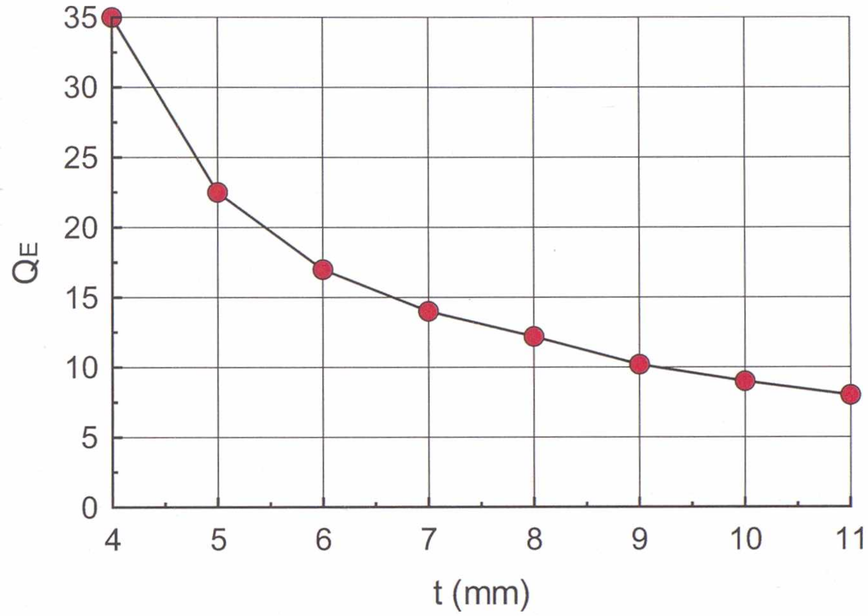

Figure 4. 17 The external quality factor as a function of tapping position *t*.

On the other hand, when the tapping positions at the centre, i.e. $l_1 = l_2 = 15.63$ mm there is no transmission zeros in the frequency response because the input/output tapping feed lines create an out of phase condition, where the output signal response is virtually flat of magnitude. Finally, the optimal value of $l_1 = 13.63$ mm and $l_2 = 17.63$ mm are selected as this configuration provides a reasonably sharp passband skirt with a relatively low passband insertion-loss as shown in Figure 4.18.

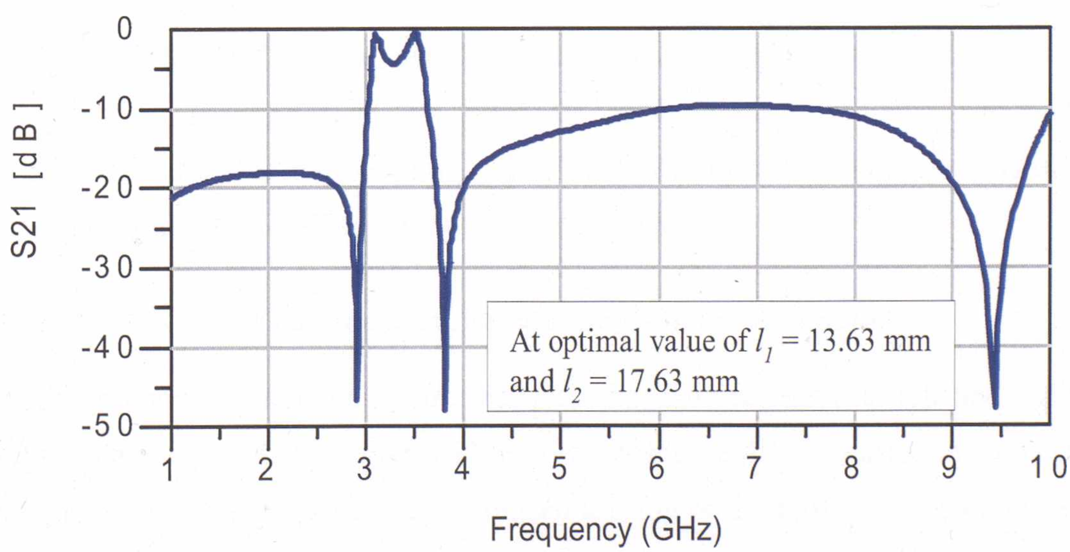

Figure 4. 18 The simulated frequency response of the compact C-shape resonator.

4.3.2.2 Effect of Open-End Coupling on the C-Shape Resonator

The coupling gap *g* at the open-end boundary as indicated in Figure 4.15 also plays a critical role in influencing the coupling conditions of the compact C-shape resonator. For this analysis, the coupling gap *g* is varied to study its effect while maintaining the resonator's line width at 1 mm. The optimal value of l_1 = 13.63 mm and l_2 = 17.63 mm are selected for this analysis based on results obtained from section 4.3.2.1. Figure 4.19 shows the simulated frequency responses for two different sizes of gap *g* (i.e. *g* = 0.58 mm and 5.58 mm).

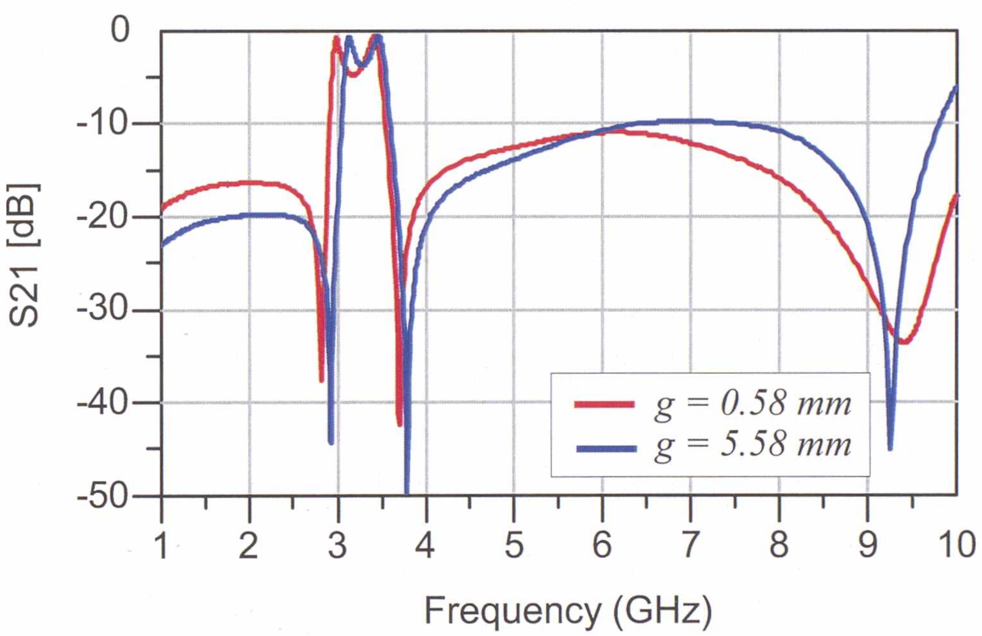

Figure 4. 19 Simulated frequency responses for different sizes of coupling gap *g*.

The above result shows that when the gap *g* is relatively large, i.e. 5.58 mm, the insertion-loss is 2.941 dB and the magnitude of coupling effect is less as compared to the case of smaller gap *g*, i.e. 0.58 mm, where the passband insertion-loss is 3.652 dB. This result concludes that the coupling gap *g* at 5.58 mm should be appropriate to produce minimal insertion-loss dip at the passband centre.

4.3.2.3 Effect of Open-End Side Coupling on the C-Shape Resonator

In this section, the coupling gap *s* between the two sections (i.e. left and right) constituting the compact C-shape resonator shown in Figure 4.15 is varied to study its effect on the resonator's coupling. The optimised tapping position of l_1 = 13.63 mm and l_2 = 17.63 mm, and coupling gap *g* at 0.58 mm, obtained in sections 4.3.2.1 and 4.3.2.2, were selected in the following analysis of gap *s*. The results of this analysis in Figure

4.20 shows that the coupling coefficient to reduce when the coupling gap s increases. When s is small, the electric coupling is dominant, while magnetic coupling dominates for bigger values of s [2]. This is because the electric coupling decays faster than magnetic coupling against the spacing.

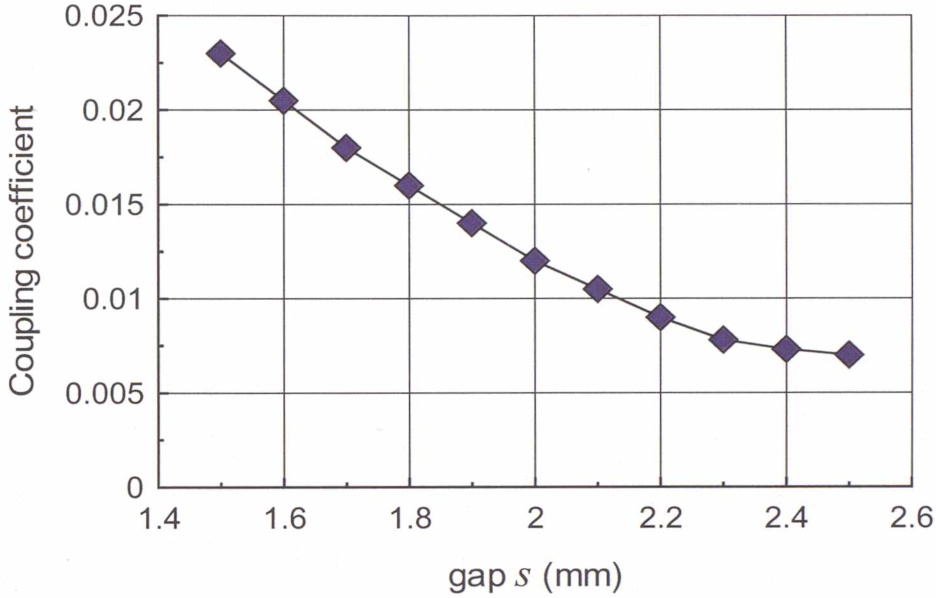

Figure 4. 20 Coupling coefficient versus coupling gap s.

Figure 4.21 shows the over-coupled, critically-coupled and under-coupled conditions for different values of s. The 3-dB bandwidths for the following three gap s values: 0.2 mm, 0.7 mm and 2.5 mm, are 489 MHz, 268 MHz and 99 MHz, respectively. Therefore, the gap s value of 0.2 mm is chosen as the optimised condition to attain a broader 3-dB bandwidth with acceptable attenuation of 2.355 dB as shown in Figure 4.21.

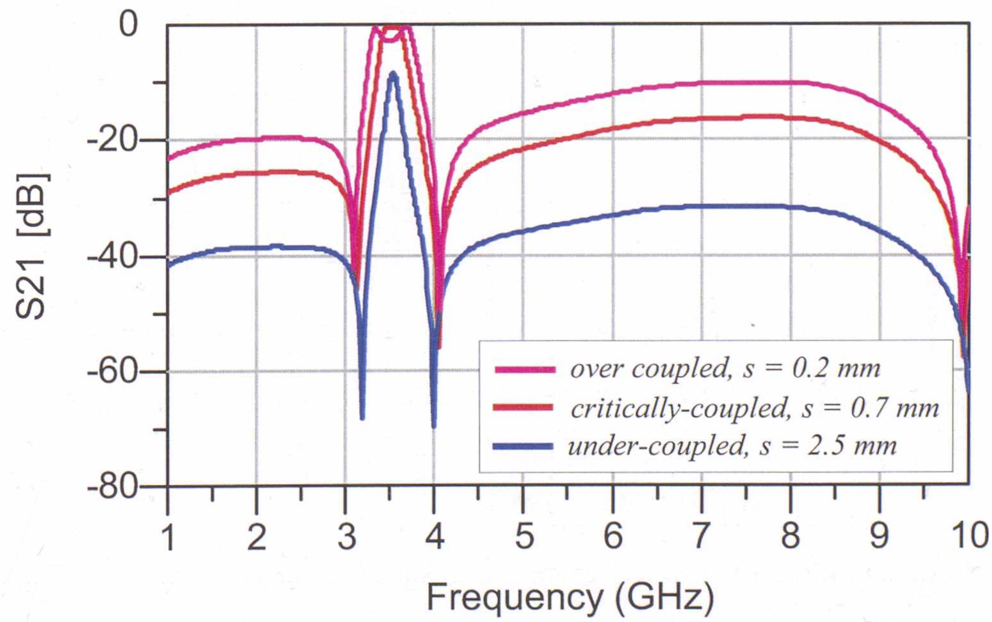

Figure 4. 21 Simulated frequency responses for different values of s.

In conclusion, all three parameters namely, the tapping positions, magnitudes of coupling gap *g* and *s*, defined in Figure 4.15, play a critical role in affecting the coupling conditions. The locations of the tapping positions directly influence the locations of the transmission zeros which affect the steepness of passband rejection with the trade-off of the passband's dip, i.e. the insertion-loss. The results also show that the smaller the gaps of *g* and *s*, the deeper the dip in the passband. In addition, the coupling effect of gap *s* is more significant as compared to the effect of gap *g*. The change in gap *s* also affects the 3-dB bandwidth, i.e. the smaller the gap *s*, the broader the 3-dB bandwidth.

4.3.3 Effect of the Resonator's Line Width on 3-dB Bandwidth

The compact C-shape structure is further investigated to determine how its line width, *w*, effects the resonator performance. For this analysis the other parameters of resonator were chosen at optimum condition, i.e.:

Tapping output/input lines positions:	l_1 = 13.63 mm and l_2 = 17.63 mm
Size of coupling gap of *g*:	5.58 mm
Size of coupling gap of *s*:	0.2 mm

The simulated frequency responses of four different widths on the C-shape resonator's response are shown in Figure 4.22.

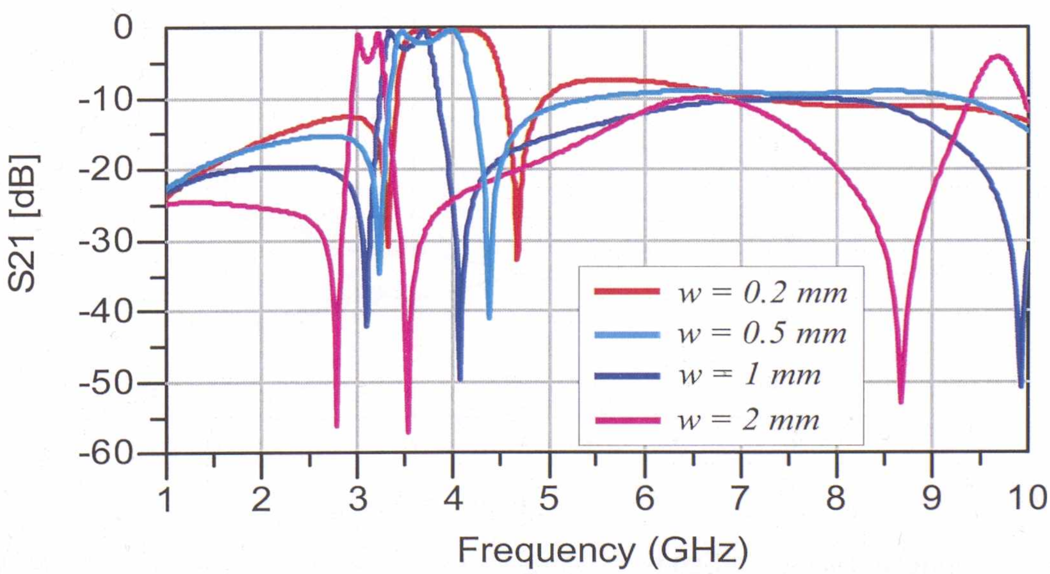

Figure 4. 22 The simulated frequency responses of four different line width.

The salient characteristics of the analysis for various values of line width *w* are given Table 4.6.

w (mm)	*3-dB bandwidth* (MHz)	*IL* (dB)	*RL* (dB)	f_o (GHz)	f_1 (GHz)	f_2 (GHz)
0.2	959	0.082	9.914	3.898	3.313	4.671
0.3	907	0.532	7.589	3.833	3.281	4.589
0.4	786	1.272	5.109	3.727	3.261	4.448
0.5	736	1.497	4.829	3.714	3.219	4.376
0.6	680	1.779	4.047	3.635	3.188	4.297
0.7	640	1.943	3.712	3.615	3.162	4.236
0.8	581	2.284	3.438	3.587	3.133	4.169
0.9	546	2.498	3.224	3.537	3.109	4.112
1.0	489	2.355	3.365	3.513	3.081	4.069
1.5	377	3.216	2.523	3.291	2.931	3.756
2.0	285	3.670	2.079	3.108	2.781	3.117

Table 4. 6 The insertion-loss, return-loss and 3-dB bandwidth corresponding to various values of line width *w*.

The results in Table 4.6 are also shown in graphical form in Figure 4.23 and Figure 4.24 to illustrate the effect of changes by the line width of the resonator's performance.

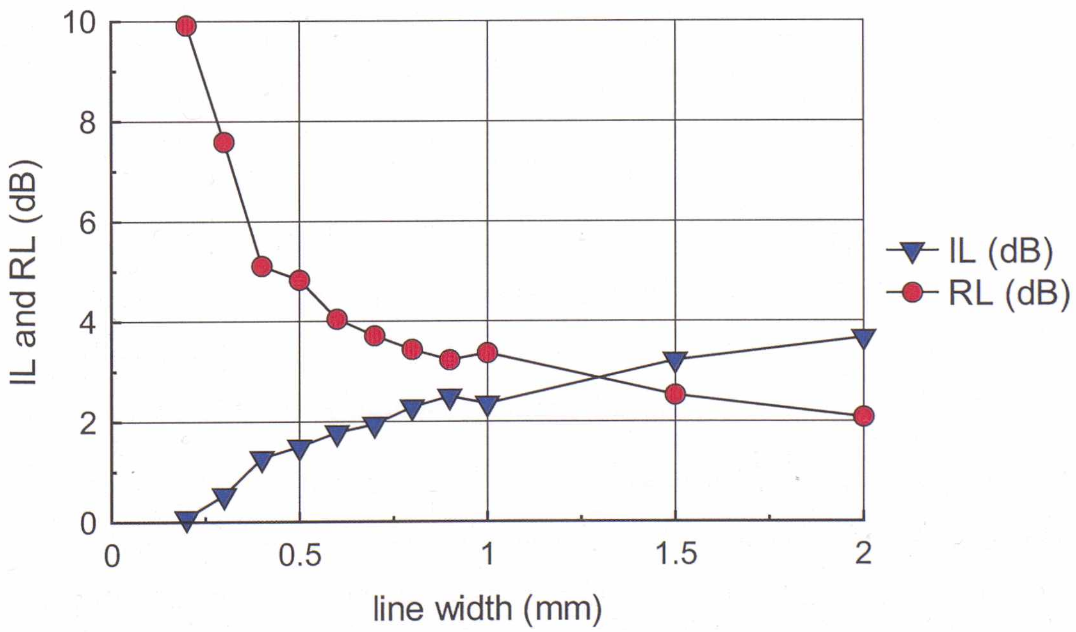

Figure 4. 23 The insertion-loss and return-loss corresponding to various line widths.

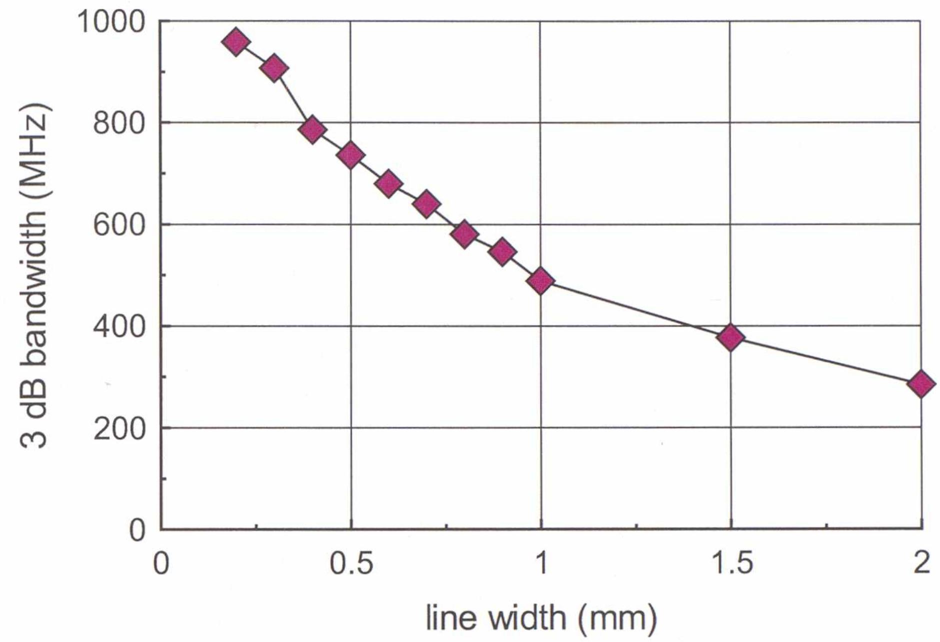

Figure 4. 24 The 3-dB bandwidths corresponding to various line widths.

The result shows that the smaller the line width, the higher the centre frequency and the broader the 3-dB bandwidth. The results also show that the 3-dB bandwidth can be controlled over a very large range extending from 285 MHz to 959 MHz, corresponding to a line width of 2 mm and 0.2 mm, respectively. It should be noted that there is no overhead in terms of insertion-loss and return-loss, i.e. the larger the 3-dB bandwidth, the lower the insertion-loss and the higher the return-loss. Therefore, the best and feasible line width for this resonator is determined to be 0.2 mm as it provides a very large 3-dB bandwidth of 959 MHz, which correspond to a fractional bandwidth of 24.6%. This property can be exploited to dynamically control the bandwidth. This can be accomplished by using capacitive varying devices such as varactor diodes to electronically control the microstrip-lines width. It is well known that a wider microstrip-line effectively represents a capacitive element. Thus, by using varactor diodes the microstrip-lines effective width can be tuned to control the resonator's bandwidth.

4.3.4 Analysis of Single Compact C-Shape Resonator

The compact C-shape resonant structure was analysed by splitting the resonator into left and right-hand sections to understand how it operated. This analysis was done at the resonator's optimum conditions obtained in the previous sections, i.e.:

Tapping output/input lines positions:	$l_1 = 13.63$ mm and $l_2 = 17.63$ mm
Size of coupling gap of g:	5.58 mm
Size of coupling gap of s:	0.2 mm
Line width of resonator w:	0.2 mm

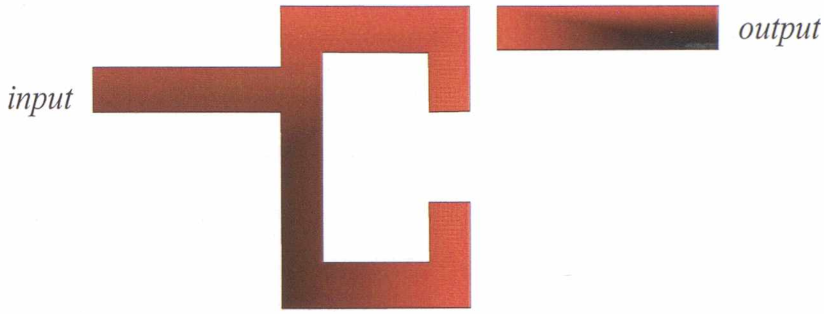

(a) *Input left and output taken from upper open-end point*

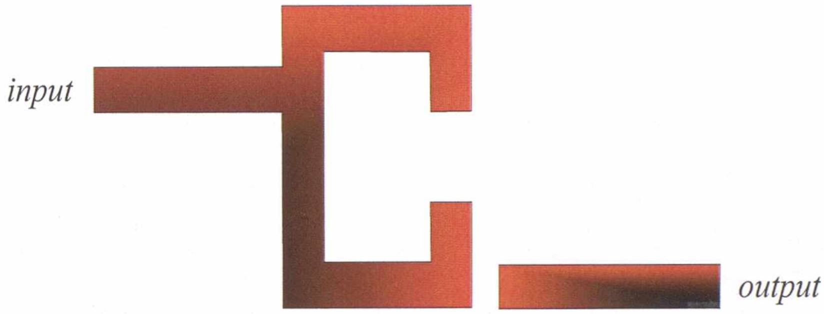

(b) *Input left and output taken from lower open-end point*

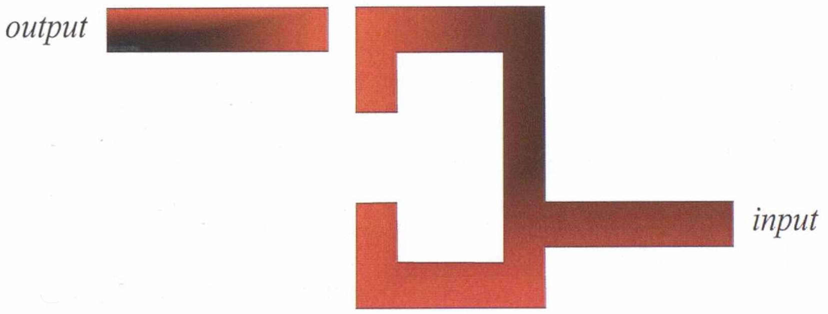

(c) *Input right and output taken from upper open-end point*

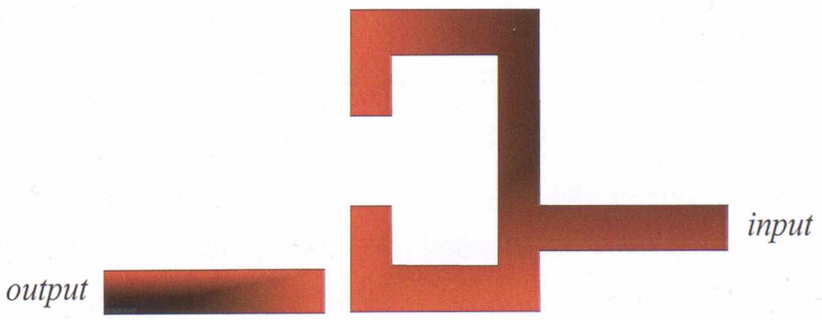

(d) *Input right and output taken from lower open-end point*

Figure 4. 25 The layout of four possible combinations representing the C-shape structure.

The layout of four possible combinations of the left and right-hand sections constituting the resonator with output port at two different locations is shown in Figure 4.25.

The results of the analyses show that the simulated frequency response for Figure 4.25(a) is same as Figure 4.25(d), while Figure 4.25(b) is same as Figure 4.25(c). This is expected because the l_1, which is the distance from the feed line tapping position to the output port position are the same for both set of combinations. Therefore, only the results for Figure 4.25(a) and Figure 4.25(c) are presented. For Figure 4.25(a), its simulated frequency response of transmission coefficient (S_{21}) and reflection coefficient (S_{22}) is shown in Figure 4.26.

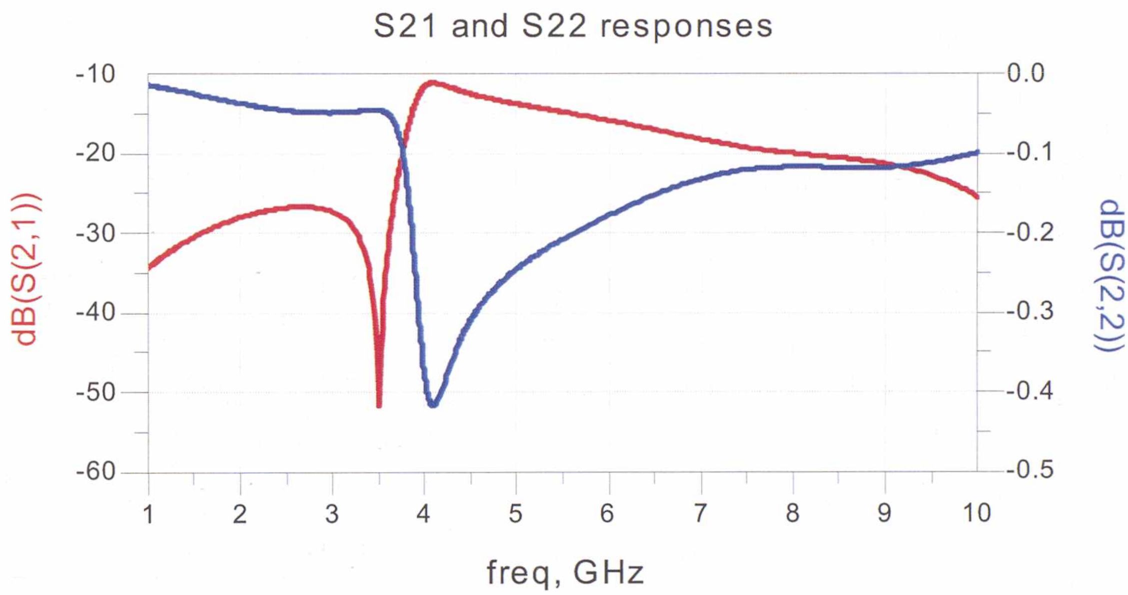

Figure 4. 26 The simulated frequency response of S_{21} and S_{22} for Figure 4.25(a).

The generation of one transmission zero at 3.514 GHz can be explained from the signal path which is split into two when entering the left-hand section of the resonator. The first path is taken through the upper part, which takes the distance of l_1 to reach the output port, whereas the other path is taken through the lower part and is reflected at the open-end boundary, which takes a distance of $2l_2 + l_1$ before emerging out at the output port. Since the distance taken by these two paths is not equivalent they create a phase difference at the output, hence generating a transmission zero. On the other hand, for Figure 4.25(c), its simulated frequency response is shown in Figure 4.27.

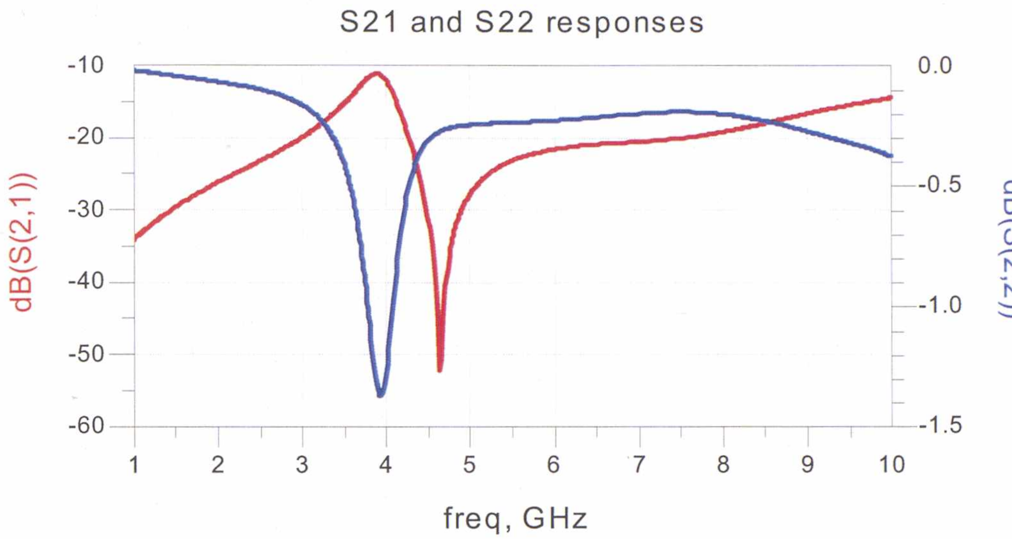

Figure 4. 27 The simulated frequency responses of S_{21} and S_{22} for Figure 4.25(c)

Using the same reasoning, the generation of one transmission zero at 4.633 GHz can be explained from the signal path which is split into two when entering the right-hand section of the resonator. The first path is through the upper part, which takes a distance l_2 to reach the output port, whereas the other path is through the lower part and is reflected at the open-end boundary, which takes a distance of $2l_1 + l_2$ before emerging out at the output port. Since the distance taken by these two paths is not equivalent they create a phase difference at the output, hence generating a transmission zero.

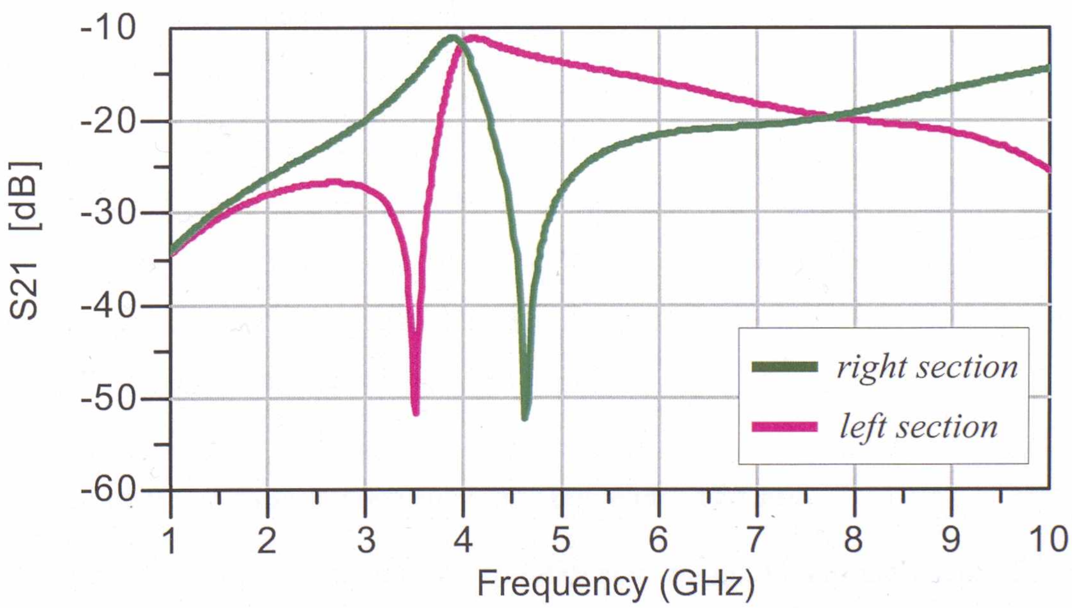

Figure 4. 28 The simulated frequency responses of S_{21} for the combination of two individual resonator sections.

This analysis shows that each individual resonator sections generate a transmission zero at different frequencies. Figure 4.28 shows the combination of these two results, and Figure 4.29 shows the combination of these two individual resonator sections (i.e. left and right-hand) forming a passband with two transmission zeros.

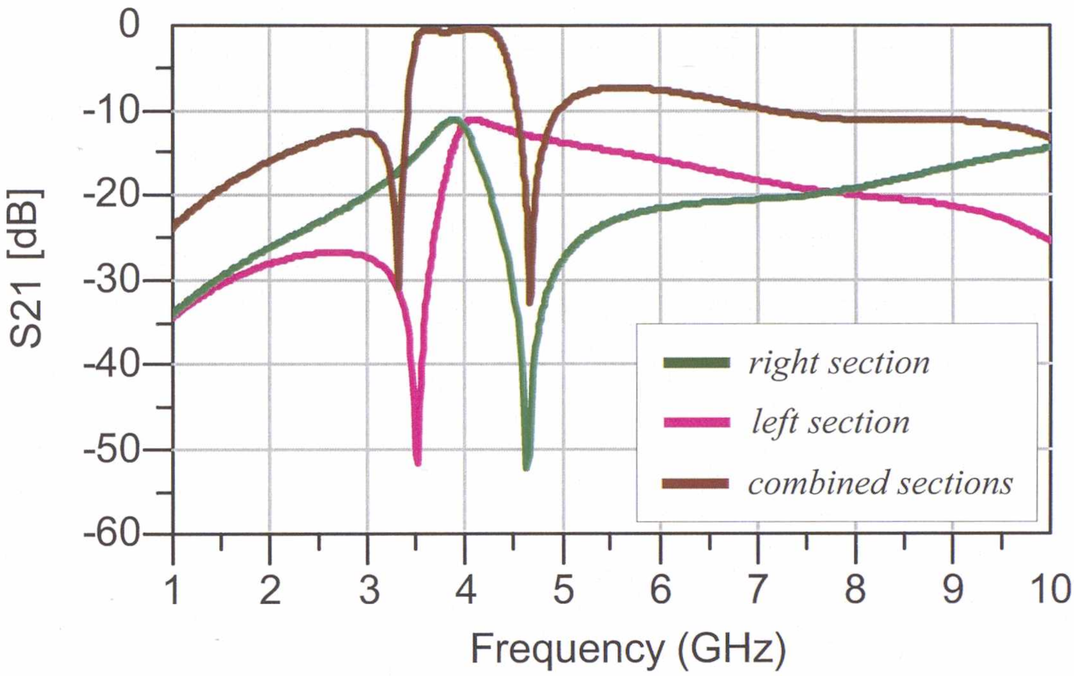

Figure 4. 29 The combination of two individual resonator sections forming a passband with two transmission zeros.

4.4 Comparison of Simulated and Measured Results

Two different line widths of compact C-shape structure, i.e. w = 1 mm and w = 0.2 mm, were fabricated, measured and tested to compare the 3-dB bandwidth, insertion-loss and return-loss results. The same substrate, i.e. 3M Cu-clad 217, with ε_r = 2.17, h = 0.794, t = 35 um, and tanδ = 0.0003) was used for both resonators for comparison purposes. The simulated and measured results were also compared to determine the degree of agreement between them.

4.4.1 Compact C-Shape Resonator with Line Width of 1 mm

Figure 4.30 shows the photograph of fabricated circuit with a line width of 1 mm having optimum dimensions: l_1 = 13.63 mm, l_2 = 17.63 mm, and g = 5.58 mm. The side gap s of 0.7 mm is used instead of the optimised value of 0.2 mm, in order to reduce the passband ripple. The simulated and measured frequency response (broadband) of this structure is shown in Figure 4.31 and 4.32, respectively. The narrow-band simulated and measured performance is shown in Figures 4.33 and 4.34.

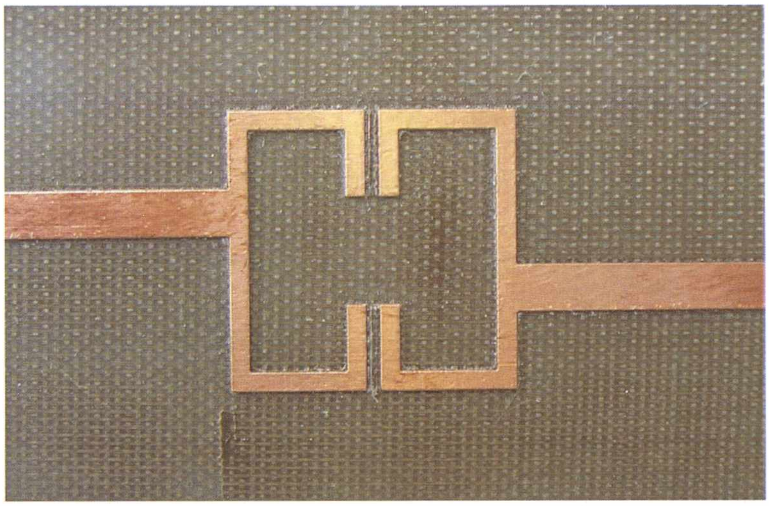

Figure 4. 30 Fabricated compact C-shape resonator filter with a line width of 1.0 mm.

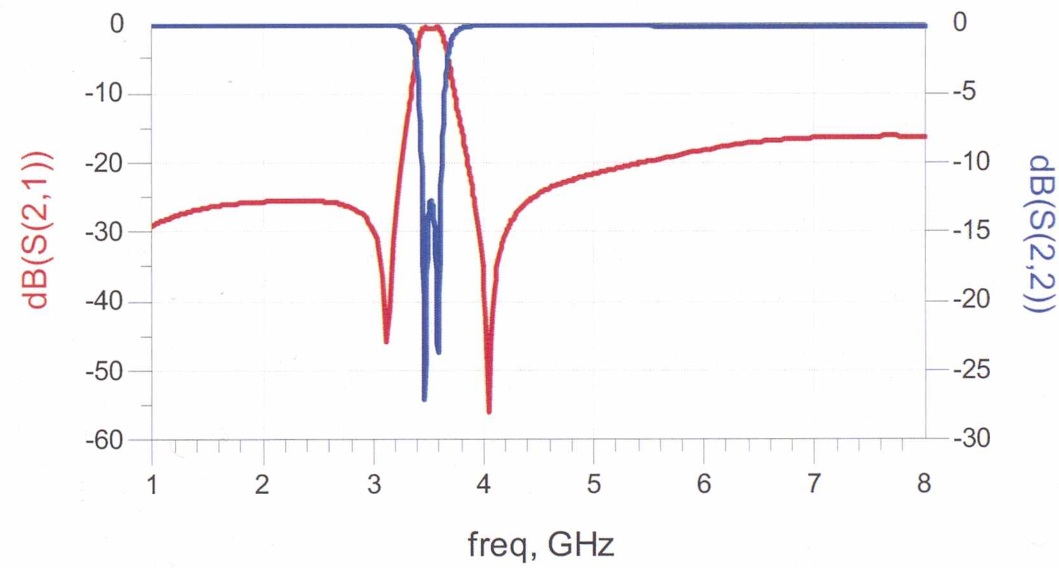

Figure 4. 31 The simulated frequency response for compact C-shape resonator (broad-band view).

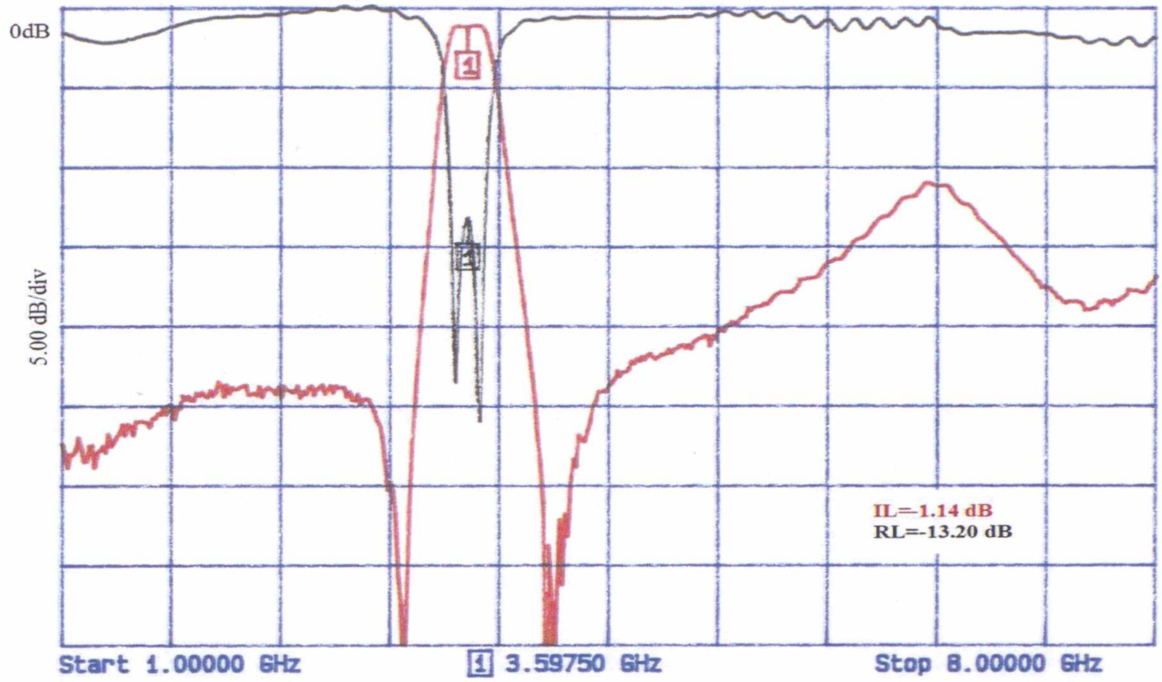

Figure 4. 32 The measured frequency response for compact C-shape resonator (broad-band view).

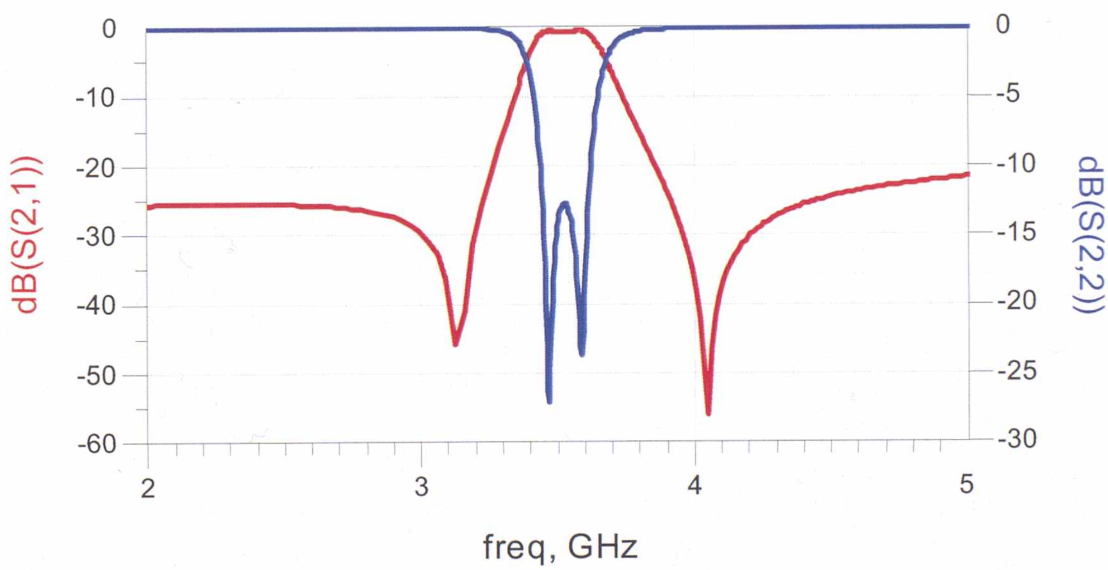

Figure 4. 33 The simulated frequency response for compact C-shape resonator (narrow-band view).

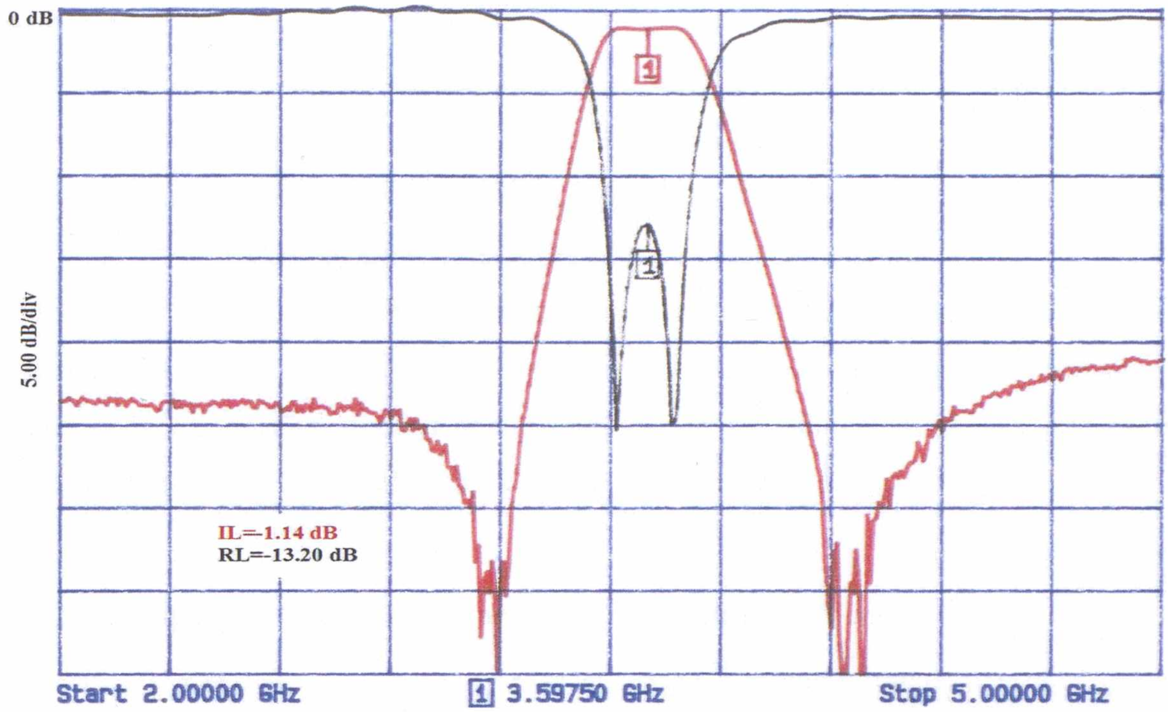

Figure 4. 34 The measured frequency response for compact C-shape resonator (narrow-band view).

The measured results indicate a very low insertion-loss of 1.14 dB and a high return-loss of 13.20 dB are obtained with this structure. A moderate value of 330 MHz for the 3-dB bandwidth (i.e. fractional bandwidth of 9.17%) is obtained at the centre frequency of 3.59750 GHz. The simulated result shows that the centre frequency, f_o is 3.530 GHz, and the two attenuation poles (i.e. f_1 and f_2) are at 3.126 GHz and 4.052 GHz, respectively. In addition, the two stop bands exhibit a rejection level of larger than 45 dB. This filter has a 3-dB bandwidth of 268 MHz with a fractional bandwidth of 7.59%, while the insertion-loss and return-loss are 0.699 dB and 12.823 dB, respectively. For ease of comparison these results are given in Table 4.7.

Results	*Centre frequency, f_o* (GHz)	*Insertion loss* (dB)	*Return loss* (dB)	3-dB *bandwidth* (MHz)	*Fractional Bandwidth* (%)
Simulated	3.530	0.699	12.823	268	7.59
Measured	3.59750	1.14	13.20	330	9.17
Error relative to simulation	1.91%	54.51%	0.60%	23.13%	1.58%

Table 4. 7 Comparison of frequency responses for measured and simulated results.

The above results indicate excellent agreement between the measured and simulated results in terms of centre frequency, return-loss, and fractional bandwidth with errors of only 1.91%, 0.60%, and 1.58%, respectively. However, the disagreement in insertion-loss is relatively high and can be attributed to the simulator models as well as the fabrication tolerance, resulting in significant conductor loss. This is because the prototype circuit was fabricated using a milling machine. Upon closed microscopic examination of the circuit shows the edges of the circuit to be erratic and rough which induces high insertion-loss. It is worth pointing out that the fabricated filter exhibits a wider 3-dB bandwidth than the simulated one, which is attributed to a smaller coupling gap s between the two sections of the resonator in the fabricated filter, as the 3-dB bandwidth is inversely related to the coupling gap s.

4.4.2 Compact C-shape Resonator with Line Width of 0.2 mm

Figure 4.35 shows the photograph of the fabricated circuit with line width w of 0.2 mm, and having optimised dimensions of l_1 = 13.63 mm, l_2 = 17.63 mm, gap g = 5.58 mm and gap s = 0.2 mm, which were obtained in sections 4.3.2 and 4.3.3.

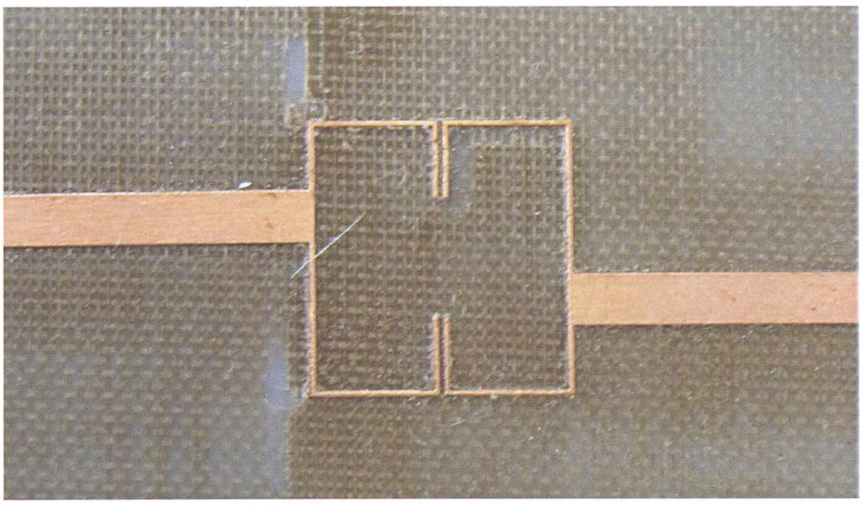

Figure 4. 35 Fabricated circuit of compact C-shape resonator with line width of 0.2 mm.

The simulated performance of the C-shape resonator in Figure 4.36 shows that the centre frequency, f_o is 3.898 GHz, with the two attenuation poles, f_1 and f_2 at 3.313 GHz and 4.671 GHz, respectively. Both attenuation poles have rejection of greater than 30 dB. The fractional bandwidth is 24.60% with a 3-dB bandwidth of 959 MHz, while the insertion-loss is 0.082 dB and return-loss is 9.914 dB. It can be observed from the measured results in Figure 4.37 that the insertion-loss at the centre frequency of 4.17 GHz is approximately 1.22 dB with a return-loss of approximately 13.16 dB. The measured 3-dB bandwidth is 1027 MHz with a fractional bandwidth of 24.63%. These results are given in Table 4.8 for ease of comparison.

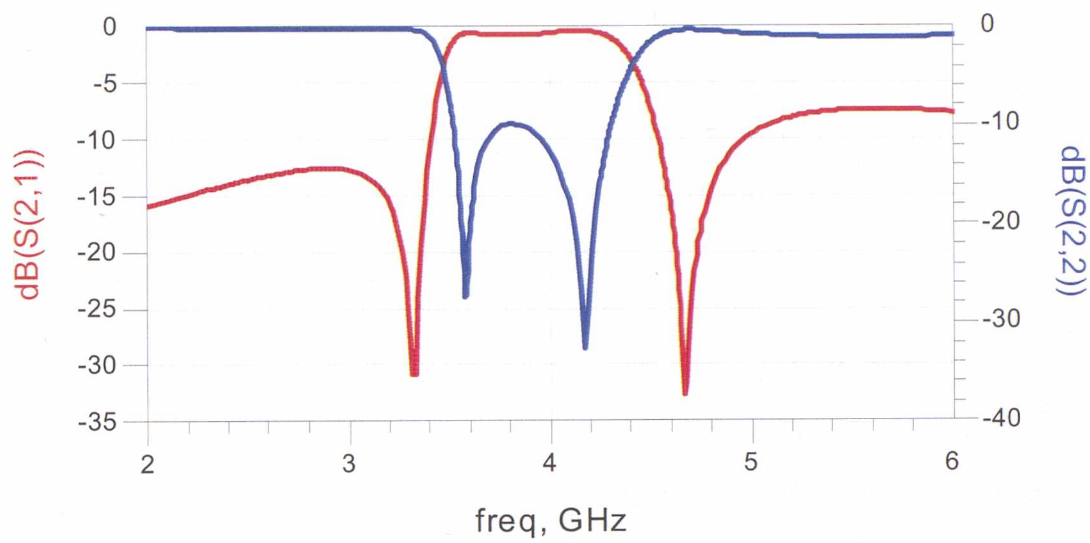

Figure 4. 36 The simulated frequency response for compact C-shape resonator (narrow-band view).

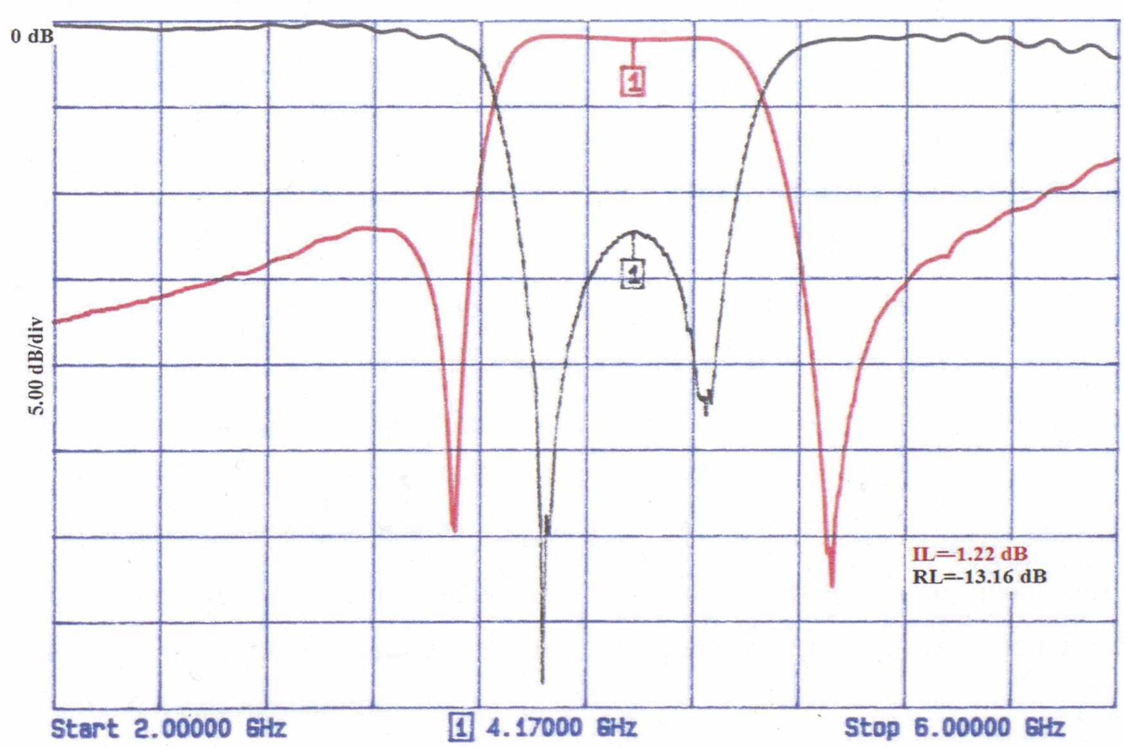

Figure 4. 37 The simulated frequency response for compact C-shape resonator (narrow-band view).

Results	*Centre frequency,* f_o (GHz)	*Insertion loss* (dB)	*Return loss* (dB)	*3-dB bandwidth* (MHz)	*Fractional Bandwidth* (%)
Simulated	3.898	0.082	9.914	959	24.60
Measured	4.1700	1.22	13.16	1027	24.63
Error relative to simulation	6.98%	1229%	24.07%	7.09%	0.03

Table 4. 8 Comparison of frequency responses for measured and simulated results.

For this resonator, the fabrication errors are higher because of the very thin line width (i.e. w = 0.2 mm). Hence, the centre frequency is out by about 7%, insertion-loss by about 1230% and return-loss by about 24%. However, it should be emphasised that the insertion-loss is about 1 dB, which is acceptable for numerous applications. The fabricated filter exhibits a wider 3-dB bandwidth than the simulation, which is attributed to a smaller coupling gap s between the two sections of the resonator. The fractional bandwidth of the simulated and measured results is 24.60% and 24.63%, respectively, while the error of 3-dB bandwidth is only about 7%. The agreement between the fractional bandwidth is excellent. The discrepancy between the simulated and measured results is attributed to the simulator models and the fabrication tolerance.

4.5 Additional Transmission Zero Generation with Modified Compact C-Shape Resonator

Further investigation was done on the C-shape resonator by increasing its length which led to the generation of the 4th transmission zero. It was also discovered that the position of this pole can be controlled by the size of the resonator's length. Hence, two resonators were developed here referred to as E-shape and G-shape resonators as illustrated in Figures 4.38 and 4.39, respectively. The total lengths of these resonators are longer than the C-shape resonator described above. The E-shape resonator has an additional 4 mm at the left and right section, and G-shape resonator has an additional 8 mm at the left and right section.

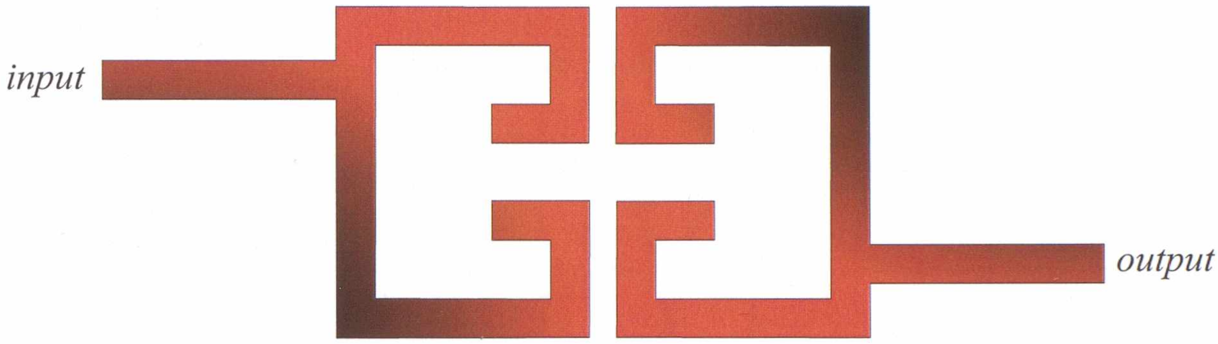

Figure 4. 38 The E-shape resonator.

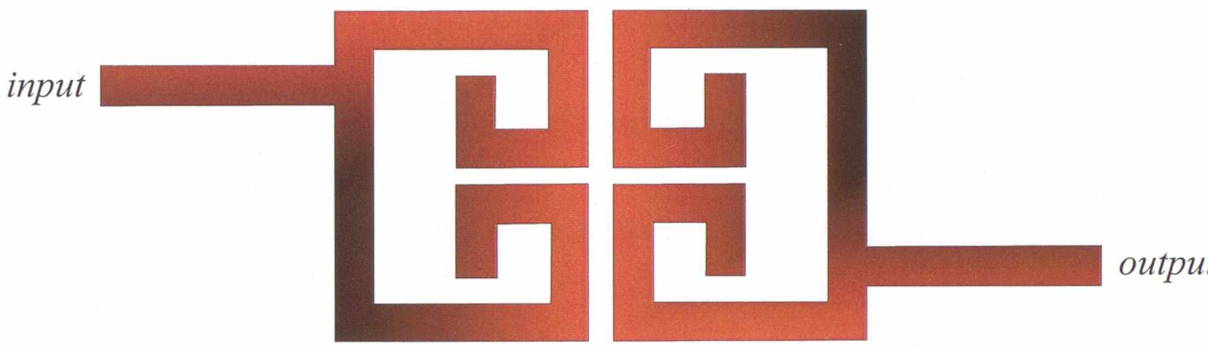

Figure 4. 39 The G-shape resonator.

The simulated frequency responses corresponding to the E-shape and G-shape resonators are shown in Figure 4.40 and 4.41, respectively. These results clearly show the modification leads to a 4th transmission zero that improves the out-of-band rejection of the filter.

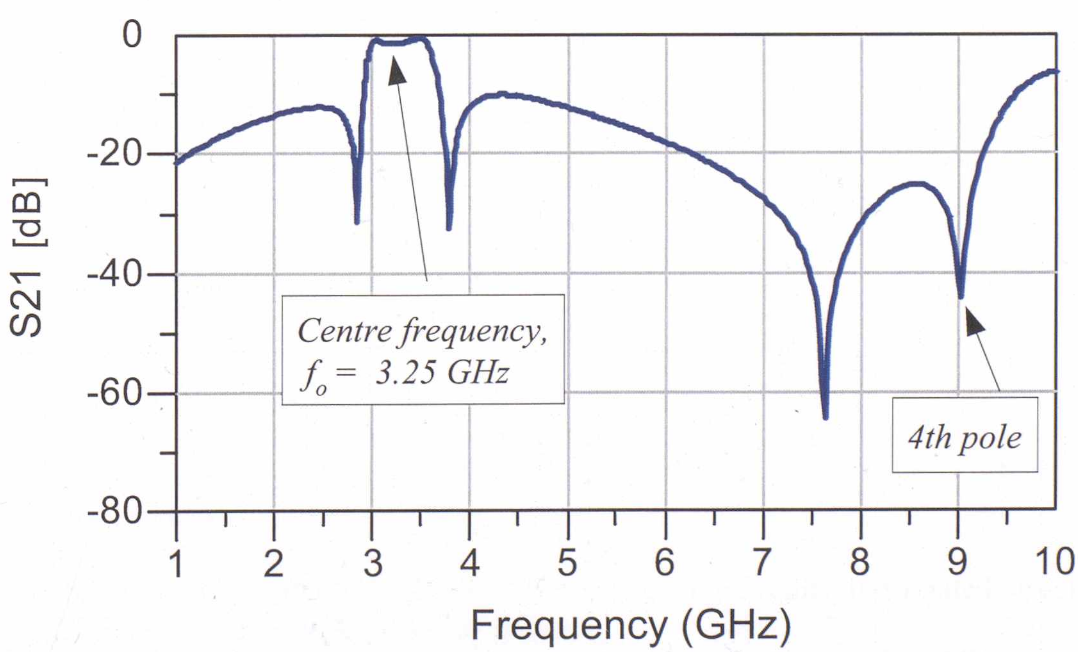

Figure 4. 40 The simulated frequency response of the E-shape resonator.

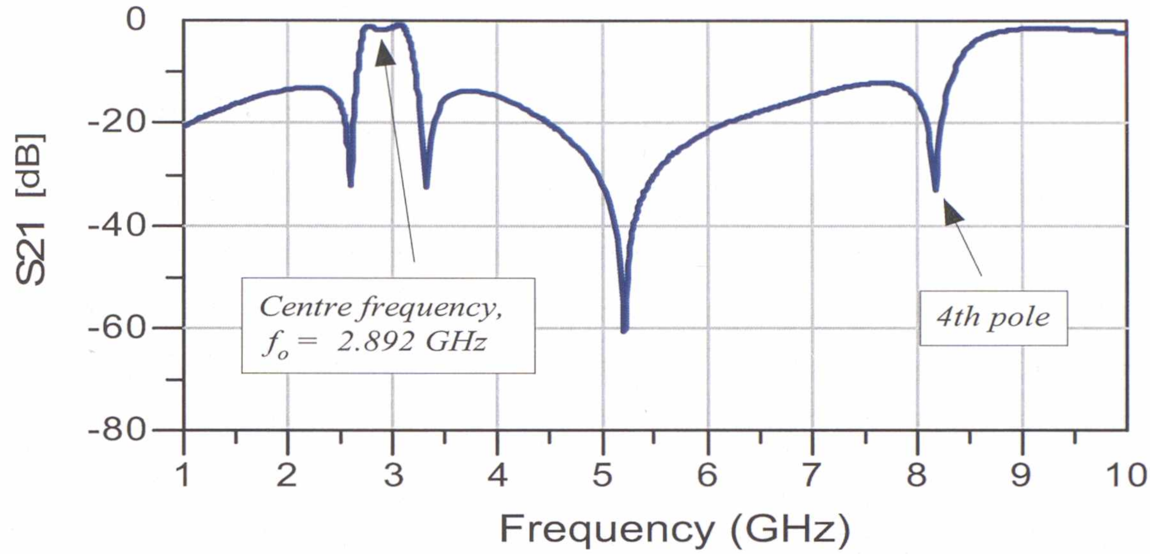

Figure 4. 41 The simulated frequency response of the G-shape resonators.

4.6 References

[1] Chang, K. & Hsieh, L.H. (2004). Microwave ring circuits and related structures (2nd Ed). New Jersey: John Wiley & Sons.

[2] Hong, J.S., Lancaster, M.J., (2001). *Microstrip Filters for RF/Microwave applications*, New York: John Wiley & Sons

Chapter 5 Compact Microstrip Filters

5.1 The Need for Spurious Free Filters

Expanding wireless and mobile communication systems have presented new challenges to the design of high-quality miniature microwave and RF filters. Planar filters are preferred since they can be fabricated using printed circuit technology with low cost. Such filters generally have a response at the desired part of the electromagnetic spectrum however they are accompanied by higher order harmonic components and unwanted responses, otherwise known as spurii. The spurii present a serious problem as they can degrade the performance of other wireless systems as most of the spectrum nowadays is highly congest with various systems, to name but a few such as mobile communications, radar and navigation. Spurii can cause leakage of inter-modulation products generated in the process of the up-conversion of the baseband signal before transmission. These inter-modulation signals if not blocked by the filter will leak and interfere with other systems. Therefore, it is essential that devices such as filters be developed free from spurious responses.

Most of the planar bandpass filters built on microstrip substrates are generally relatively large in size and have their spurious responses at $2f_o$ and $3f_o$, where f_o is the centre frequency. For example, the half wavelength resonator inherently has spurious passband at $2f_o$, while quarter wavelength filters have the first spurious passband at $3f_o$, but they require short-circuit connection via holes, which are not quite compatible with planar fabrication technique. To reject these frequency parasitics, half wavelength short circuit stubs, chip capacitors or cascaded rejection band filters have been traditionally used. However, these techniques are either narrow band, increase device area, or introduce significant insertion losses. Various other methods have been recently developed to improve the stopband performance of a planar microwave bandpass filters. These techniques to suppress spurious signals in bandpass filters include utilizing parallel-coupled microstrip filters with over-coupled end stages [1]. In [2] the sinusoidal rule is used to eliminate spurious harmonics by continuously perturbing the width of the coupled lines in the microstrip wiggly-line filter. Using stepped-impedance resonators in planar microstrip bandpass filters [3]–[5], the second harmonic is shown to shift to a higher frequency band resulting in relatively wide stopband. Moreover, harmonic suppression can be carried out by employing the cross-coupling between resonators [6], the split-ring resonators in close proximity to conductor strip [7], the open stub and spurline [8]–[11], ground-plane aperture [12], combining the low-pass/bandstop filter with a bandpass filter [13], and with the assistance of open stubs and inter-digital capacitors [14].

In this chapter the compact C-shape resonator is modified to suppress the spurious responses across a wide frequency range. This is achieved by loading the resonator with inductive and capacitive elements in the form of high and low impedance transmission lines of various geometries, slots, and stubs. It is demonstrated that the resulting resonant structure yields suppression of spurii across a wide stopband range up to 20 GHz. The final proposed bandpass filter structure achieves double the stopband response over e.g. reference [5] and three fold over [8], without compromising its salient features of passband insertion-loss and return-loss. In addition, the proposed structure is significantly smaller, i.e. by 50%, than those presented in references [5] and [10].

5.2 'Embedded-Square' C-Shape Resonator

Figure 5.1 shows the C-shape resonator from Chapter 4 loaded or embedded with a square patch which is connected to the ends of open loop resonators in order to achieve a wide spurious free response.

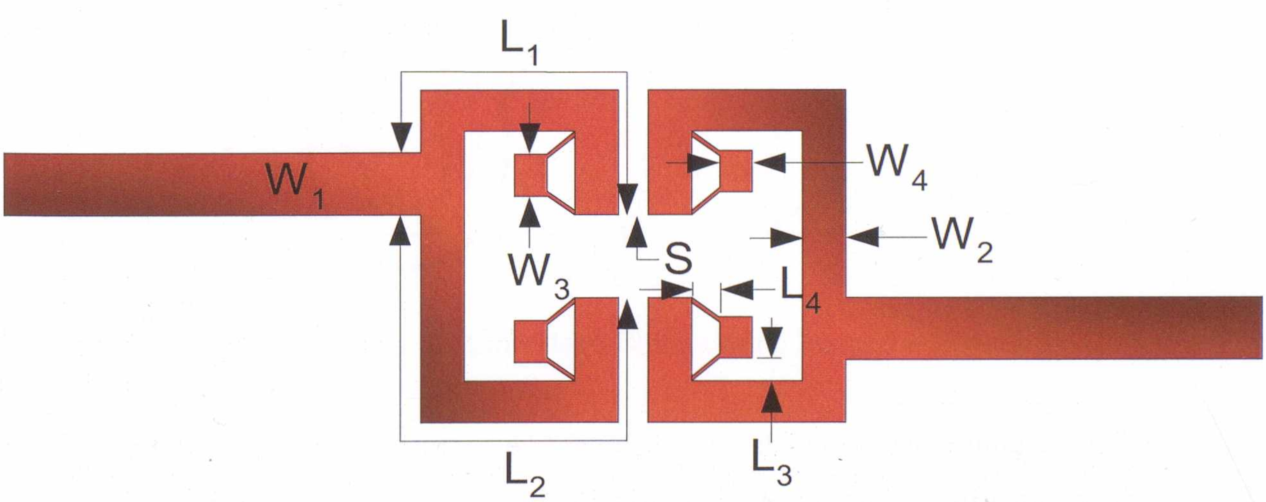

Figure 5. 1 The layout of the 'Embedded-Square' C-shape filter.

Initially, the 'embedded-square' C-shape bandpass filter, shown in Figure 5.1, was designed at a fundamental frequency of 3 GHz using Equations (4.15a) and (4.15b) in Chapter 4. The dimensions of the filter are: L_1 = 13.63 mm, L_2 = 19.63 mm, L_3 = 1.2

mm, L_4 = 1.4 mm, W_1 = 2.24 mm, W_2 = 0.2 mm, W_3 = 2 mm, W_4 = 1.2 mm and S = 0.25 mm.

5.2.1 The 'Embedded-Square' C-Shape Filter Analysis

To theoretically analyze the 'Embedded-Square' C-shape filter using ABCD matrix, the filter is first represented by its equivalent lumped element circuit, shown in Figure 5.2. To simplify the circuit further, the inductive elements comprising the triangle and consisting of elements *La* and *Lb* are represented by *Lt*, which is given by

$$Lt = \frac{Lb(La + Lb)}{L1 + 2L2} \tag{5.1}$$

The impedance Z indicated in Figure 5.2 is

$$Z = Lt + Cp \tag{5.2}$$

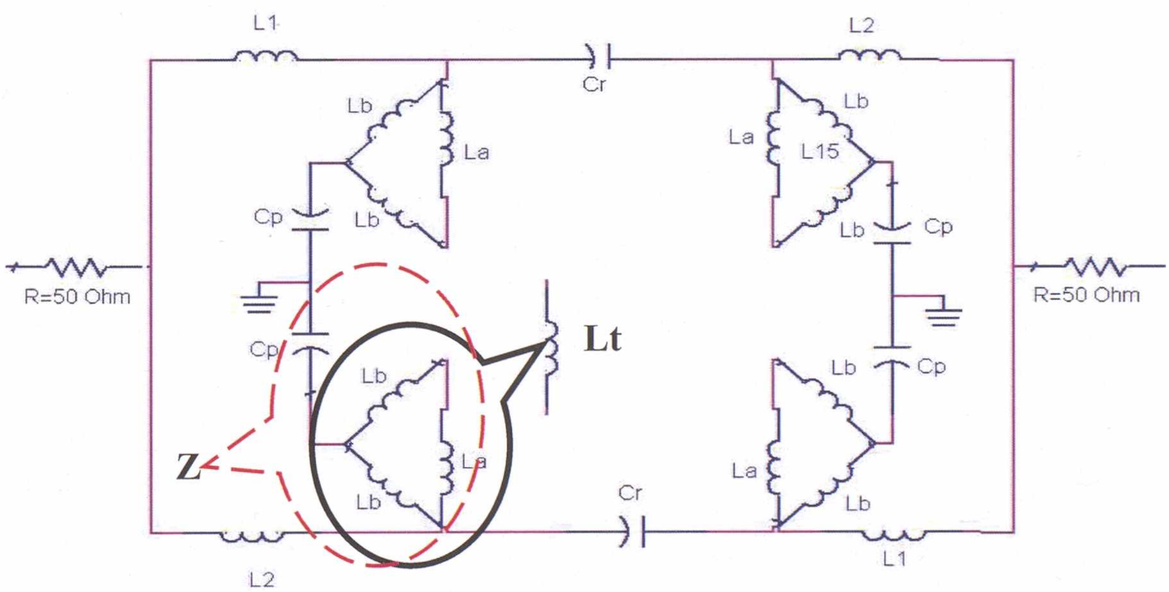

Figure 5. 2 Representing the Embedded-Square using lumped elements.

Further simplification of the circuit in Figure 5.2 is achieved by dividing it up into upper and lower sections. The final ABCD matrix for the proposed structure is then obtained by adding the matrix's representing the upper and lower sections, thus

The ABCD matrix for upper section

$$\begin{bmatrix} A & B \\ C & D \end{bmatrix}_{upper} = \begin{bmatrix} 1 & j\omega L1 \\ 0 & 1 \end{bmatrix} \begin{bmatrix} 1 & 0 \\ Z & 1 \end{bmatrix} \begin{bmatrix} 1 & 1/j\omega Cp \\ 0 & 1 \end{bmatrix} \begin{bmatrix} 1 & 0 \\ Z & 1 \end{bmatrix} \begin{bmatrix} 1 & j\omega L2 \\ 0 & 1 \end{bmatrix} \tag{5.3a}$$

For the lower section

$$\begin{bmatrix} A & B \\ C & D \end{bmatrix}_{lower} = \begin{bmatrix} 1 & j\omega L2 \\ 0 & 1 \end{bmatrix} \begin{bmatrix} 1 & 0 \\ Z & 1 \end{bmatrix} \begin{bmatrix} 1 & 1/j\omega Cp \\ 0 & 1 \end{bmatrix} \begin{bmatrix} 1 & 0 \\ Z & 1 \end{bmatrix} \begin{bmatrix} 1 & j\omega L1 \\ 0 & 1 \end{bmatrix} \tag{5.3b}$$

Therefore the overall matrix is

$$\begin{bmatrix} A & B \\ C & D \end{bmatrix}_{total} = \begin{bmatrix} A & B \\ C & D \end{bmatrix}_{upper} + \begin{bmatrix} A & B \\ C & D \end{bmatrix}_{lower} \tag{5.4}$$

The values of the capacitors and inductors in Figure 5.2 can then be calculated in order to plot the frequency response of the filter using the MATLAB code provided in Appendix I.

Figure 5.3 shows the theoretical response of the 'Embedded-Square' C-shape filter. By using the embedded-square patch at the end of the open loop resonator, the third transmission zero can be moved from 10 GHz in the classic open loop resonator to 8 GHz in this new structure. This leads to more attenuation in the out of band spurii up to 14 GHz.

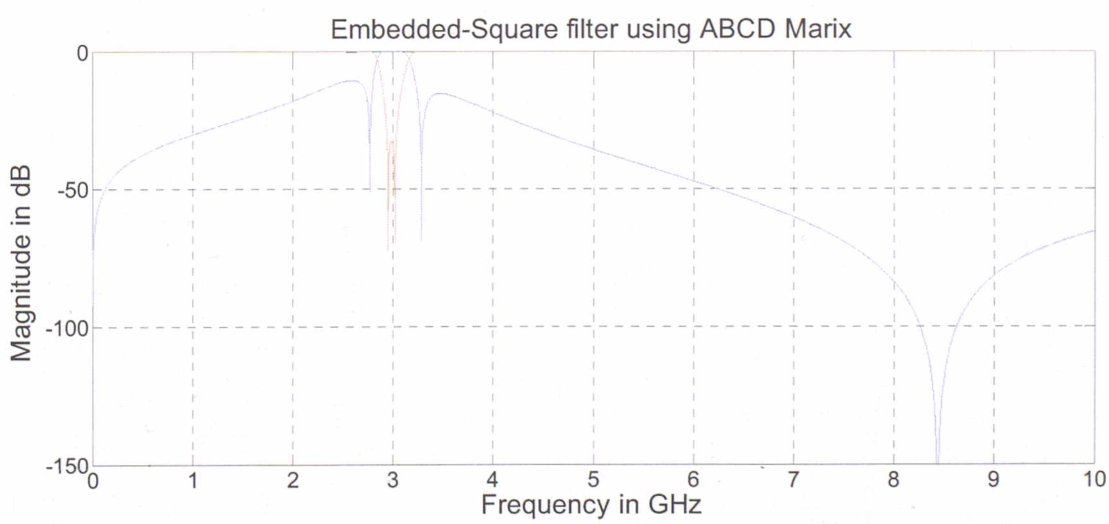

Figure 5. 3 Theoretical response of the 'Embedded-Square' C-shape filter.

5.2.2 Comparison of Simulated and Measured Results

The 'Embedded-Square' C-shape filter was fabricated on 3M Cu-clad217 substrate from Arlon with a thickness of 0.76 mm, relative dielectric constant of 2.17, loss tangent of 0.0009, and conductor thickness of 35 microns. The filter's performance was measured using a Network Analyzer. The photograph of the fabricated filter is shown in Figure 5.4. The simulated and measured broadband frequency response of this structure is shown in Figures 5.5 and 5.6, respectively. The simulated and measured narrow-band response is shown in Figure 5.7 and 5.8, respectively. The salient features of this device are shown in Table 5.1.

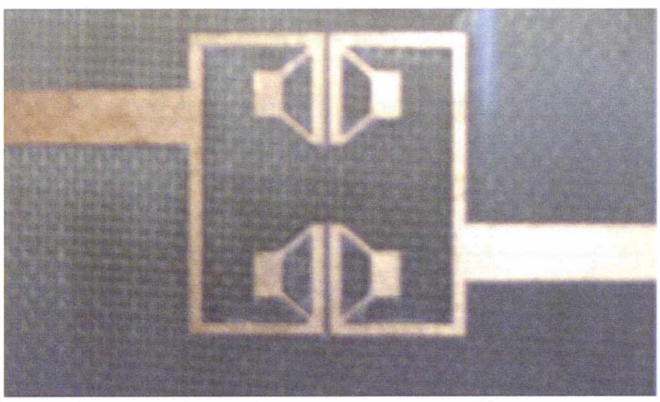

Figure 5. 4 Photograph of the fabricated circuit of 'Embedded-Square' C-shape resonator.

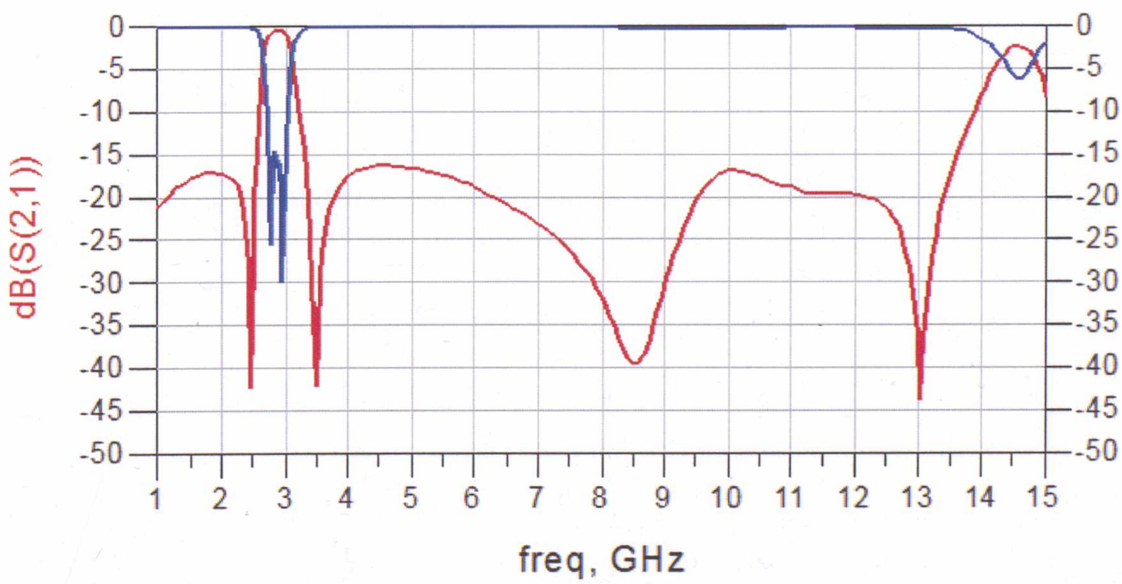

Figure 5. 5 The simulated frequency response of the 'embedded-square' C-shape resonator (broadband view).

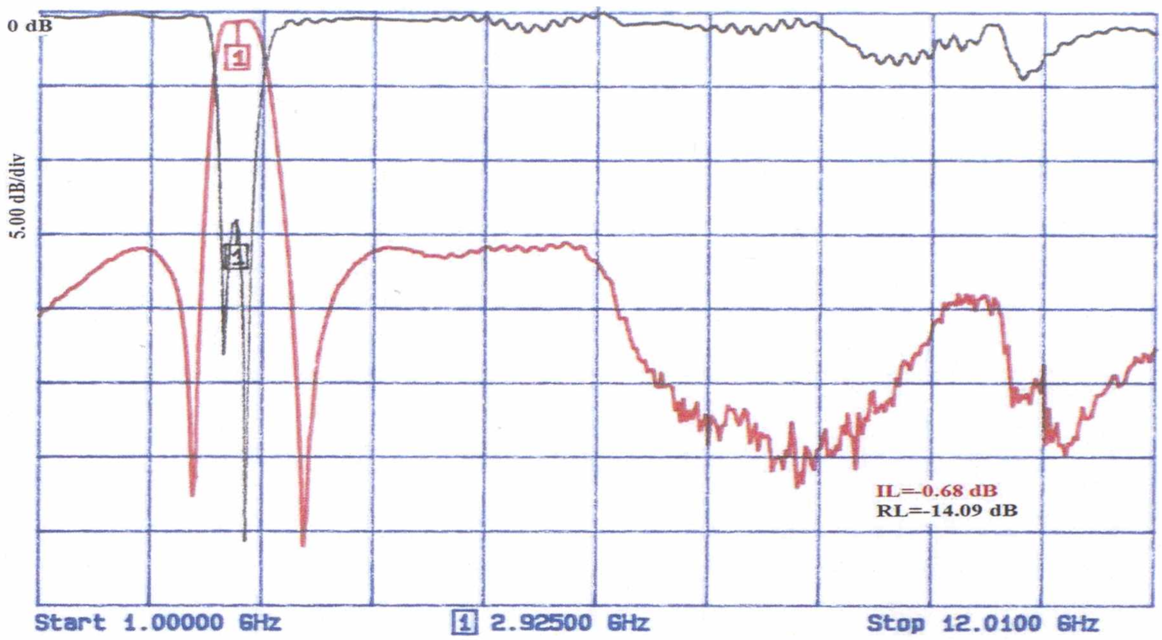

Figure 5. 6 The measured frequency response of the 'Embedded-Square' C-shape resonator (broad-band view).

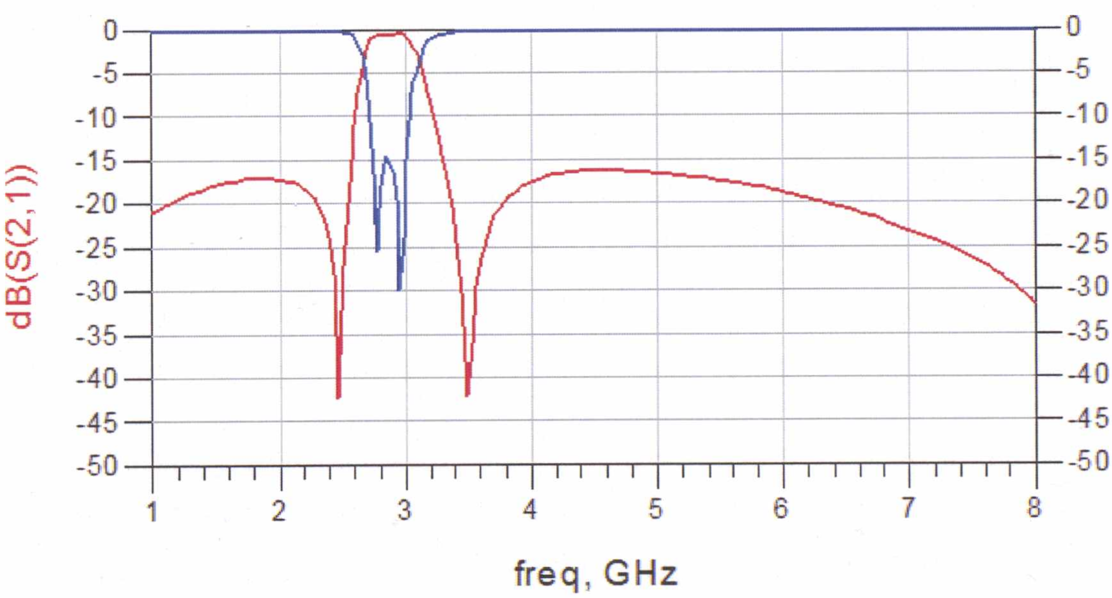

Figure 5. 7 The simulated frequency response of the 'Embedded-Square' C-shape resonator (narrow-band view).

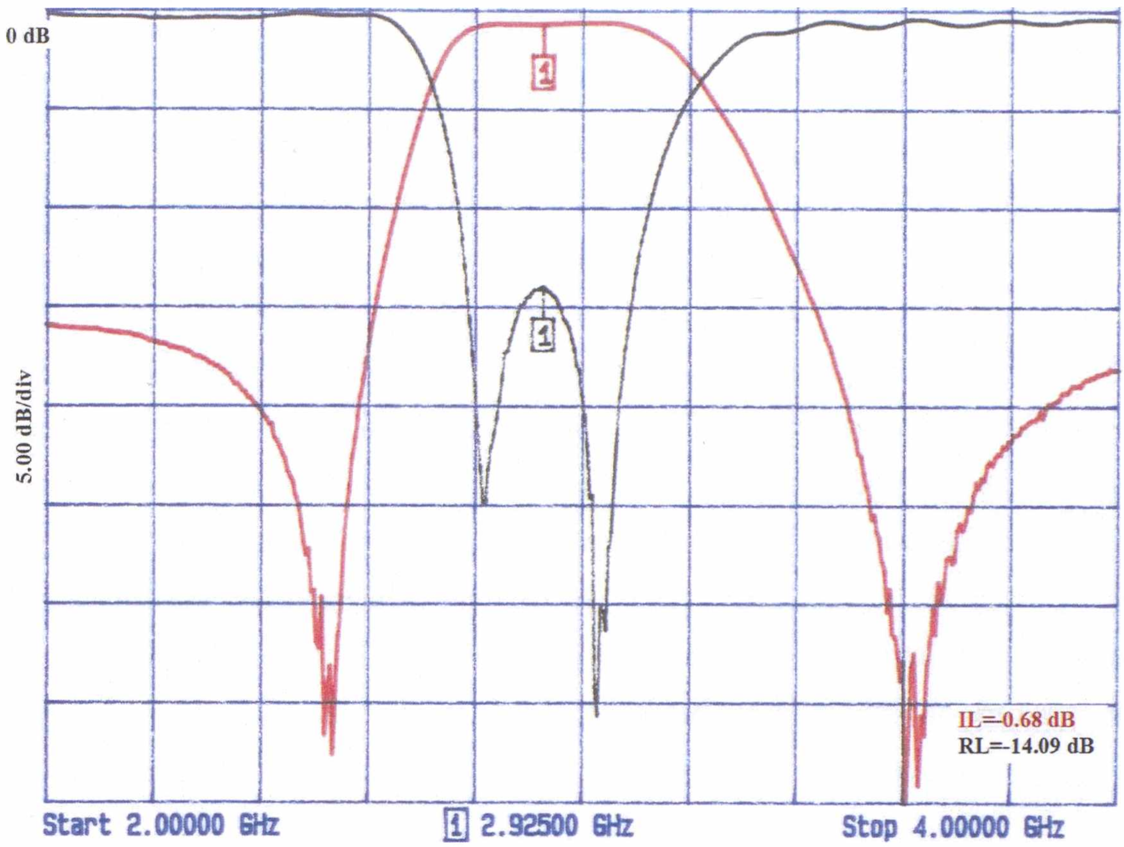

Figure 5. 8 The measured frequency response the 'Embedded-Square' C-shape resonator (narrow-band view).

The simulated structure's centre frequency f_o is 2.910 GHz with attenuation poles f_1 and f_2 at 2.470 GHz and 3.488 GHz, respectively. The fractional bandwidth is 15.33% with the 3-dB bandwidth of 446 MHz, while the passband insertion-loss is 0.493 dB and the return-loss is 14.463 dB. These results are compared with the measured results in Table 5.1.

Results	*Centre frequency* f_o (GHz)	*Insertion-loss* (dB)	*Return-loss* (dB)	*3-dB bandwidth* (MHz)	*FractionalBandwidth* (%)
Simulated	2.910	0.493	14.463	446	15.33
Measured	2.925	0.68	13.97	533	18.22
Error relative to simulation	0.52%	37.93%	3.41%	19.51%	2.89%

Table 5. 1 Comparison of frequency responses for measured and simulated results.

This 'Embedded-Square' C-shape resonator achieves passband rejection better than 14 dB and it suppresses spurious response by more than 15 dB up to 13.5 GHz.

The insertion-loss of the fabricated filter is only 0.68 dB at the centre frequency of 2.925 GHz. In addition, this resonator is able to achieve a 3-dB bandwidth of 533 MHz (i.e. fractional bandwidth of 18.22% at centre frequency of 2.925 GHz) with a return-loss of 13.97 dB. The fabricated filter exhibits a wider 3-dB bandwidth than the simulated one, because of the effect of a smaller coupling gap C_g between the two electrically coupled sections of the resonator in the fabricated structure. This is because the 3-dB bandwidth is inversely related to the coupling gap C_g. The error in insertion-loss of 37.93% is attributed to the inaccurate models employed in the simulation tool and fabrication errors. However, a better and a more precise fabrication technology can improve these errors. The errors in centre frequency, return-loss, and fractional bandwidth are much smaller, i.e. 0.52%, 3.41% and 2.89%, respectively. These measured results confirm the validity and the usefulness of the proposed 'Embedded-Square' C-shape resonator structure. Hence, these facets render the resonator to be suitable for many practical applications.

5.3 'Embedded-Triangle' C-Shape Resonator

Figure 5.9 shows the 'Embedded-Triangle' resonator. This structure has also evolved from compact C-shape resonator with some modification and is able to achieve spurious free response up to 17.5 GHz. This structure provides better return-loss (> 25 dB) as compared to the 'Embedded-Square' resonator in Figure 5.1.

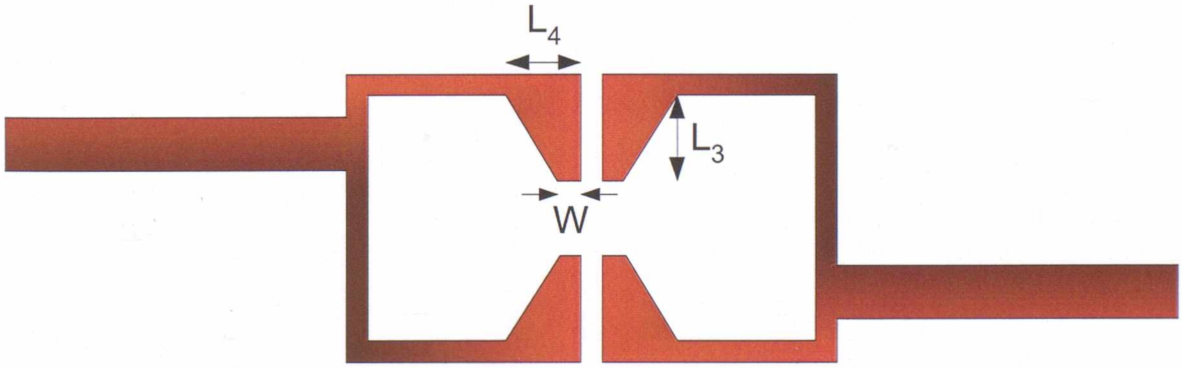

Figure 5. 9 The 'Embedded-Triangle' C-shape Resonator.

Initially the filter's fundamental resonant frequency of 3 GHz design was based on Equations (4.15a) and (4.15b) in Chapter 4. The filter's triangular shaped open end load dimensions, defined in Figure 5.9, are: $L_3 = 4.42$ mm, $L_4 = 2.4$ mm and W = 0.3 mm.

Similarly to the 'Embedded-Square' C-shape filter, this filter can be represented by its equivalent lumped element circuit to analyse the effect of this new structure. The values of the capacitors and inductors in Figure 5.10 can then be calculated in order to plot the frequency response of the filter using the MATLAB code provided in Appendix I.

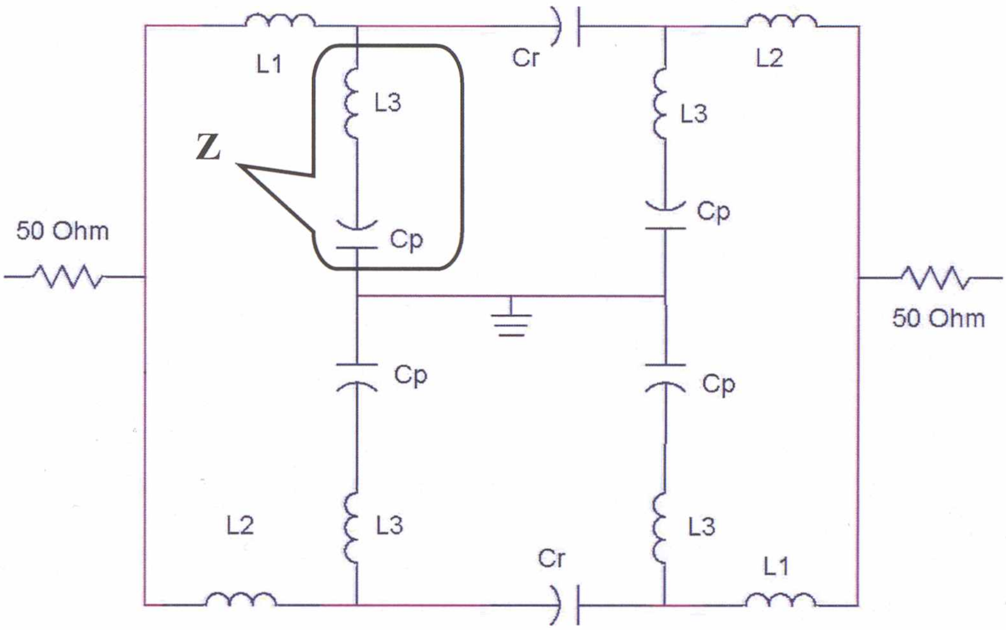

Figure 5. 10 Representing the Embedded-Triangles using lumped elements.

$$\begin{bmatrix} A & B \\ C & D \end{bmatrix}_{upper} = \begin{bmatrix} 1 & j\omega L1 \\ 0 & 1 \end{bmatrix} \begin{bmatrix} 1 & 0 \\ Z & 1 \end{bmatrix} \begin{bmatrix} 1 & 1/j\omega Cr \\ 0 & 1 \end{bmatrix} \begin{bmatrix} 1 & 0 \\ Z & 1 \end{bmatrix} \begin{bmatrix} 1 & j\omega L2 \\ 0 & 1 \end{bmatrix} \tag{5.5a}$$

$$\begin{bmatrix} A & B \\ C & D \end{bmatrix}_{lower} = \begin{bmatrix} 1 & j\omega L2 \\ 0 & 1 \end{bmatrix} \begin{bmatrix} 1 & 0 \\ Z & 1 \end{bmatrix} \begin{bmatrix} 1 & 1/j\omega Cr \\ 0 & 1 \end{bmatrix} \begin{bmatrix} 1 & 0 \\ Z & 1 \end{bmatrix} \begin{bmatrix} 1 & j\omega L1 \\ 0 & 1 \end{bmatrix} \tag{5.5b}$$

Where $Z = L3 + Cp$

$$\begin{bmatrix} A & B \\ C & D \end{bmatrix}_{total} = \begin{bmatrix} A & B \\ C & D \end{bmatrix}_{upper} + \begin{bmatrix} A & B \\ C & D \end{bmatrix}_{lower} \tag{5.6}$$

The theoretical frequency response of the 'Embedded-Triangle' C-shape filter is shown in Figure 5.11. This figure clearly shows the quasi-elliptical function response exhibited by the filter at around 3.2 GHz with a high out-of-band rejection up to 12 GHz.

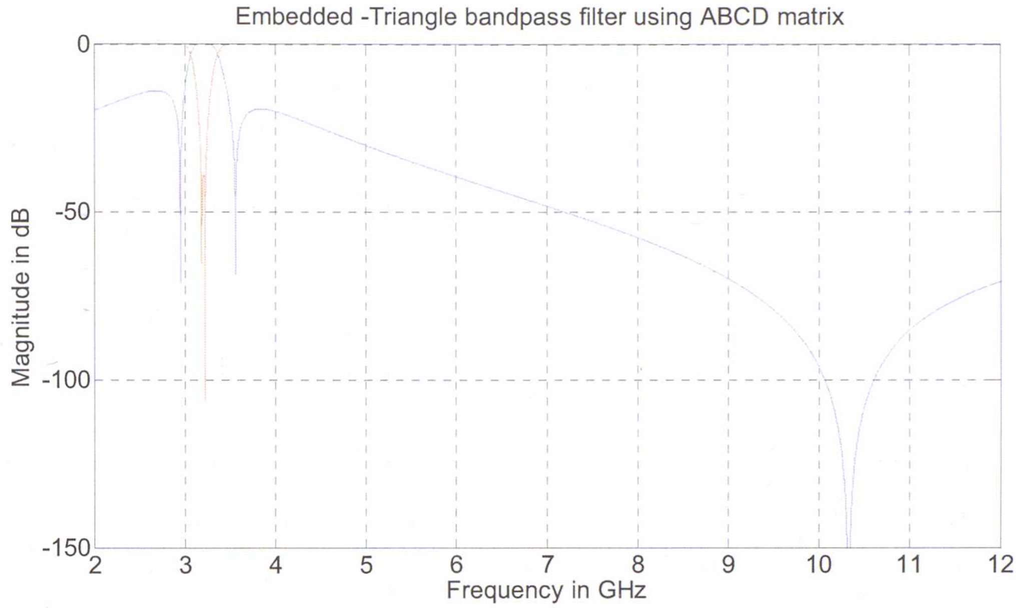

Figure 5. 11 The theoretical response of the 'Embedded-Triangle' C-shape bandpass filter.

5.3.1 Comparison of Simulated and Measured Results

The 'Embedded-Triangle' C-shape filter was fabricated on 3M Cu-clad217 substrate from Arlon having a thickness of 0.76 mm and relative dielectric constant of 2.17. The performance of the fabricated device was measured using a Network Analyzer. The photograph of the fabricated circuit is shown in Figure 5.12.

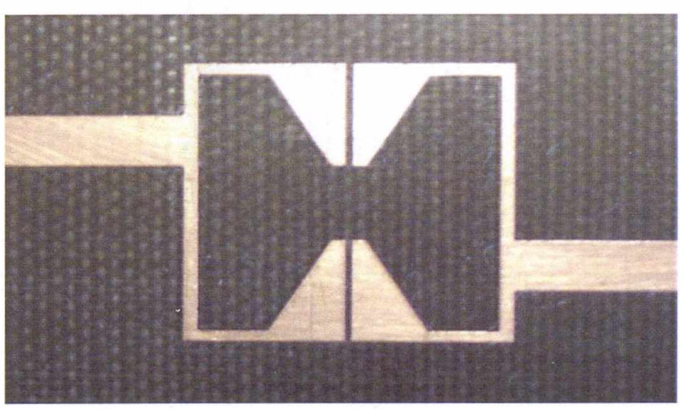

Figure 5. 12 Photograph of the fabricated circuit of 'Embedded-Triangle' resonator.

The broadband and narrowband simulated response of the 'Embedded-Triangle' resonator are shown in Figures 5.13 and 5.14, respectively. The filter's centre frequency, f_o is 3.187 GHz, while both attenuation poles, f_1 and f_2, are 2.640 GHz and 4.054 GHz, respectively. The passband insertion-loss is 0.365 dB and return-loss is

24.89 dB. The 3-dB bandwidth of the filter is 646 MHz at the centre frequency of 3.187 GHz, and its fractional bandwidth is 20.27%. These results are compared with the measured results presented in Figures 5.15 and 5.16 in Table 5.2.

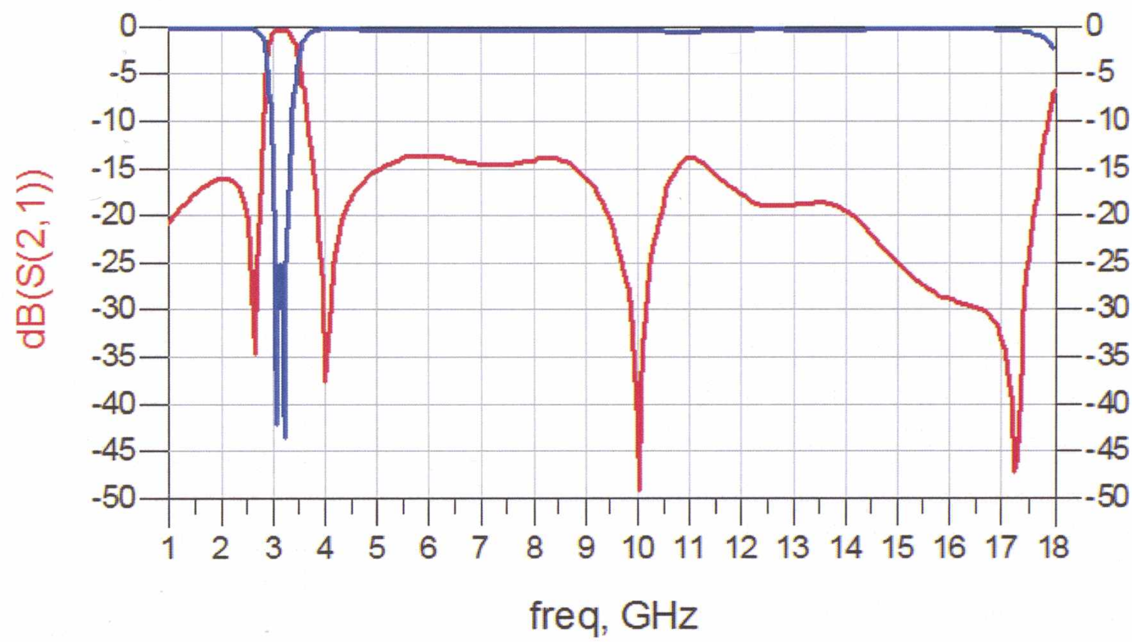

Figure 5. 13 The simulated frequency response of the 'Embedded-Triangle' C-shape resonator (broadband view).

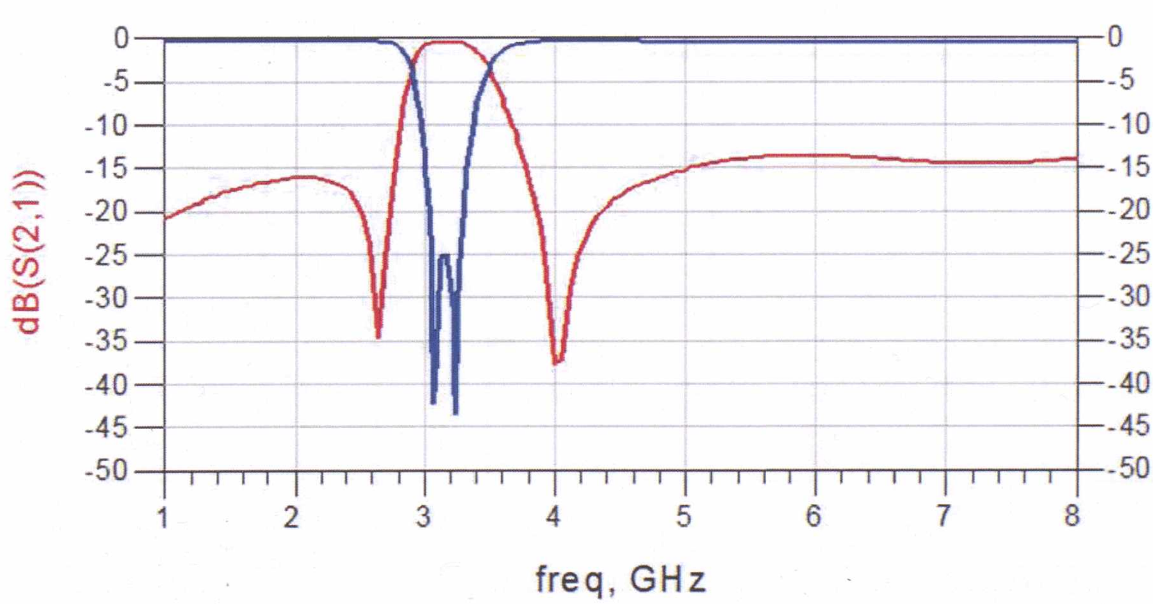

Figure 5. 14 The simulated frequency response of the 'Embedded-Triangle' C-shape resonator (narrowband view).

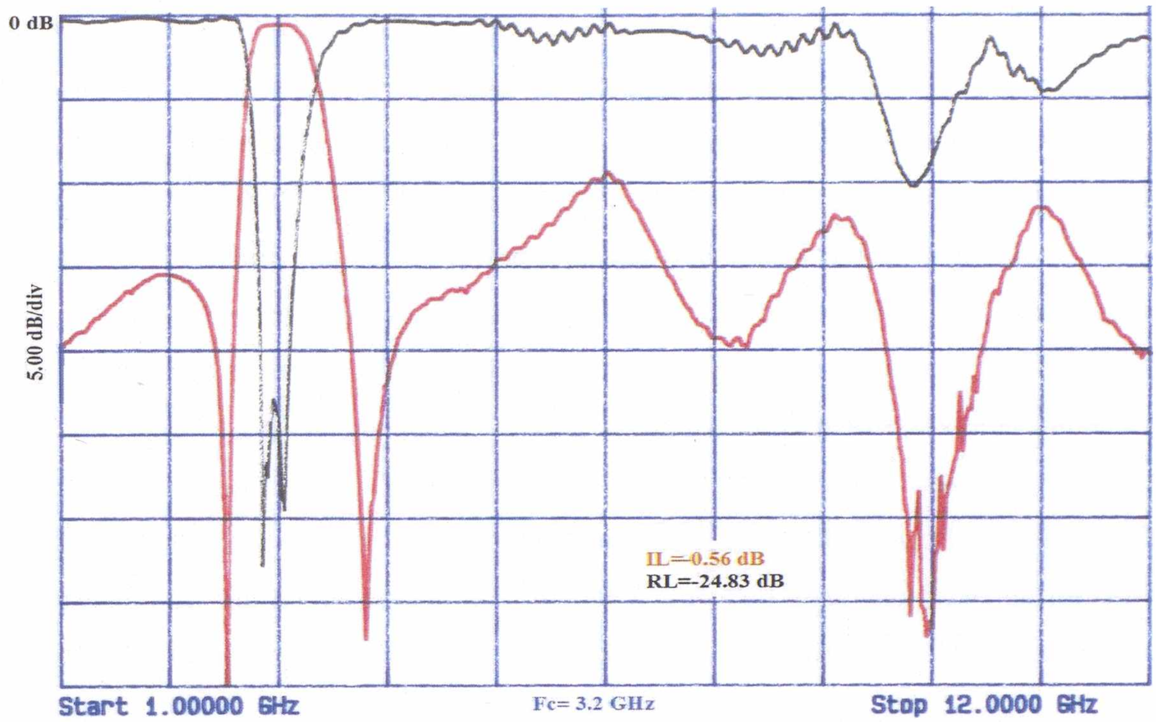

Figure 5. 15 Measured frequency response of the 'Embedded-Triangle' C-shape resonator (broadband view).

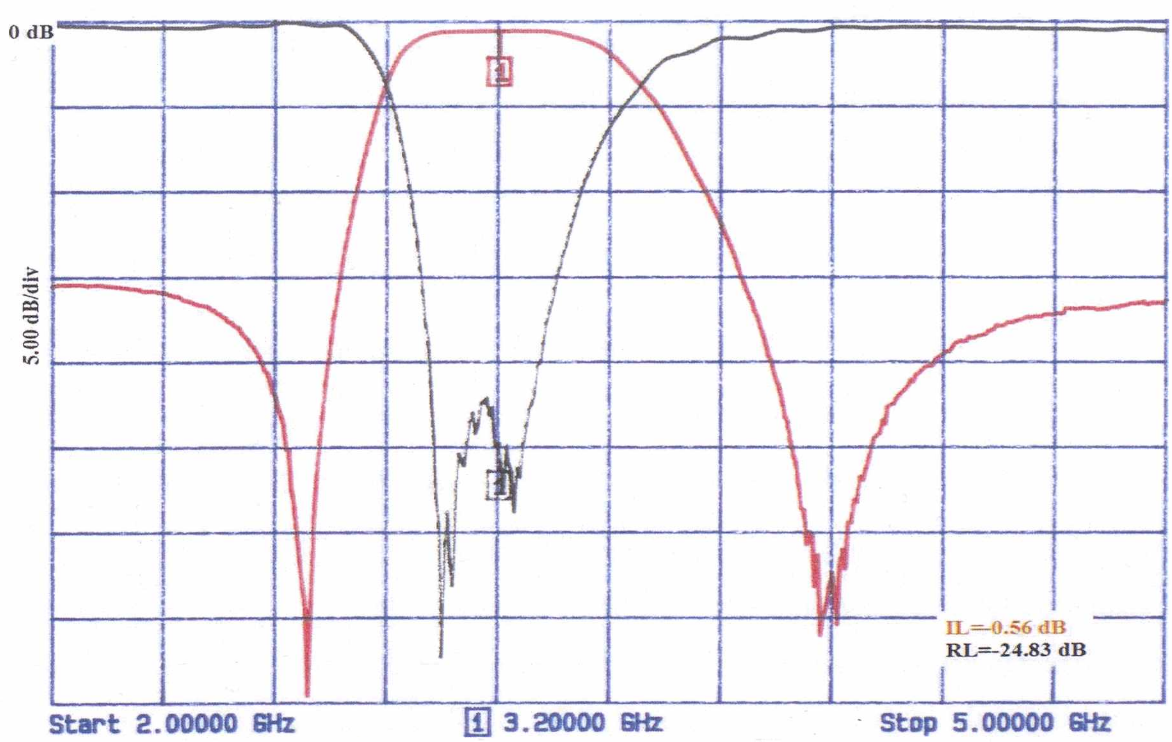

Figure 5. 16 The measured frequency response of the 'Embedded-Triangle' C-shape resonator (narrowband view).

The measured results show that the 'Embedded-Triangle' resonator provides out-of-band rejection of about 13 dB up to 17.5 GHz. In addition, this resonator is able to achieve a 3-dB bandwidth of 715 MHz (i.e. a fractional bandwidth of 22.34% at centre frequency of 3.2 GHz) with a return-loss of 24.83 dB. The insertion-loss of the fabricated filter is only 0.56 dB at centre frequency of 3.2 GHz. The conductor loss results in a higher insertion-loss of 53.43% compared to the simulated result. This discrepancy can be attributed to the simulation models and fabrication tolerance errors. The errors for centre frequency, return-loss and fractional bandwidth are only 0.41%, 0.24% and 2.07%, respectively. The fabricated filter exhibits a wider 3-dB bandwidth of 715 MHz as compared to a simulated value of 646 MHz. This is because of the effect of a smaller coupling gap C_g in the fabricated circuit, as the 3-dB bandwidth is inversely related to the coupling gap C_g. The 'Embedded-Triangle' resonator shows improvement over the 'Embedded-Square' resonator not only in the 3-dB bandwidth but also in the suppression of spurious response up to higher frequency range. Hence, its performance is suitable for many practical applications that emphasize broadband spurii free response.

Results	*Centre frequency, f_o* (GHz)	*Insertion-loss* (dB)	*Return - loss* (dB)	*3-dB bandwidth* (MHz)	*Fractional Bandwidth* (%)
Simulated	3.187	0.365	24.89	646	20.27
Measured	3.2	0.56	24.83	715	22.34
Error relative to simulation	0.41%	53.43%	0.24%	10.68%	2.07%

Table 5. 2 Comparison of frequency responses for measured and simulated results.

5.4 A Compact Ultra-Wideband Spurii-Free Quasi-Elliptic Function Filter

In this section a compact microstrip bandpass filter is proposed that provides a quasi-elliptical response with a sharp cut-off and high out-of-band rejection across a wide frequency spectrum. This is achieved with the assistance of triangular shaped capacitive loading at the open-end of the open-loop resonators that incorporate rectangular shaped slots and strategically located open-end stubs within the resonators. The consequence of this is the realisation of harmonic suppression over a very wide frequency bandwidth extending up to 20 GHz. A prototype was fabricated to verify the feasibility of the proposed technique. Measured results demonstrate that the stopband rejection better than 15 dB is obtained from 1 to 20 GHz. The rejection band obtained in this design is significant improvement over [5] by about two-fold, and over [8] by more than three-fold. In addition, the proposed filter is 50% smaller in size compared to open-loop filter structures reported in [5] and [10] even though these filters employ a higher dielectric constant substrate of 3.38.

5.4.1 A Compact Ultra-Wideband Filter Design

The layout of the proposed filter is shown in Figure 5.17. The open-loop resonators have asymmetric input and output feed lines to create two transmission zeros located on either side of the passband centre, and are capacitively loaded using triangular shaped microstrip patches at the open-ends of the resonators. The triangular patches include L-shaped slots. The triangular patches increase the electromagnetic coupling between the two open-loop resonators to minimise its passband loss. The simulations show that if these slots have a length equal to nearly half guide wavelength, the excited surface currents suffer from a destructive interference. The dimensions, shape and position of these slots have been chosen after a comprehensive numerical study of their influence on the rejection band. This led to significantly improved passband insertion-loss and return-loss performance and out-of band spurii rejection up to 17 GHz. Further improvement in extending the out-of-band rejection is obtained by including open-end stubs located at E-field maxima at the resonance frequency of interest, as shown in Figure 5.17. The frequency of the rejected band is related to the stubs' physical length, which is approximately one quarter guided wavelength at the centre of the band.

The proposed filter was designed at the centre frequency of 3 GHz and was fabricated on 3M Cu-clad217 substrate from Arlon with a thickness of 0.76 mm and relative dielectric constant of 2.17. The filter dimensions, as defined in Figure 5.17, are: L1 = 8.5 mm, L2 = 2.5 mm, L3 = 6 mm, L4 = 1.8 mm, L5 = 1.5 mm, L6 = 0.8 mm, L7 = 0.7 mm, L8 = 0.6 mm, L9 = 0.8 mm, L10 = 1.4 mm, W1 = 2.42 mm, W2 = 0.5 mm, G1 = 0.25 mm and S1 = 0.3 mm.

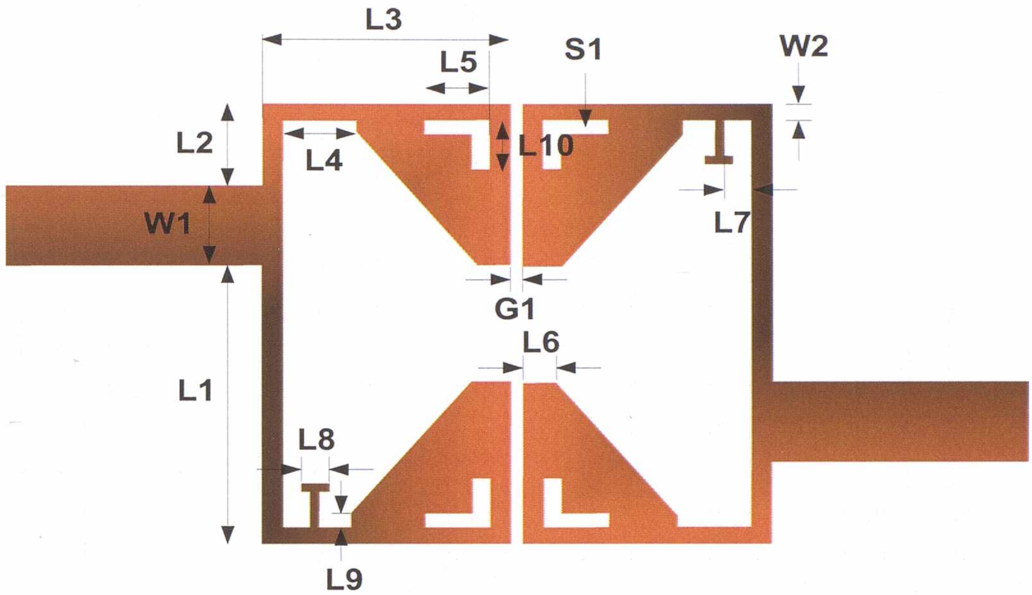

Figure 5. 17 Layout of the proposed open-loop resonator.

5.4.2 Comparison of Simulated and Measured Results

Figure 5.18 shows the simulation response of the proposed filter with the triangular patches include L-shaped slots. Figure 5.19 shows how the inclusion of the two open stubs, shown in Figure 5.17, eliminates the spurious response at 17.5 GHz.

The proposed filter with a centre frequency of 3 GHz exhibits an extra 5 dB rejection over a typical open-loop resonator filter across 1 to 20 GHz frequency range, as shown in Figure 5.20.The filter's 3 dB fractional bandwidth is approximately 16.2%. Two transmission zeros adjacent to the passband are been realised at 2.5 GHz and 3.7 GHz with the attenuations of around 40 dB; additionally, a third transmission zero is located at 10.3 GHz and the attenuation is better than 50 dB, and the fourth transmission zero is located at 18.3 GHz with attenuation better than 60 dB. The simulated passband insertion-loss is about 0.25 dB and the return-loss is about 30 dB. The proposed filter was fabricated with dimensions defined in Figure 5.17. Its measured wideband and narrowband responses are shown in Figures 5.21 and 5.22, respectively. The measured centre frequency is 3.04 GHz, insertion-loss is 0.10 dB and return-loss is 22.01 dB. The filter 3 dB fractional bandwidth is 16.87%. As shown in Figure 5.21 the filter provides ultra-broadband spurii rejection greater than 15 dB across 1 to 20 GHz. The observed differences between simulation and measurement results are attributed to the manufacturing tolerances of the prototype circuit. The photograph of the filter is shown in Figure 5.23.

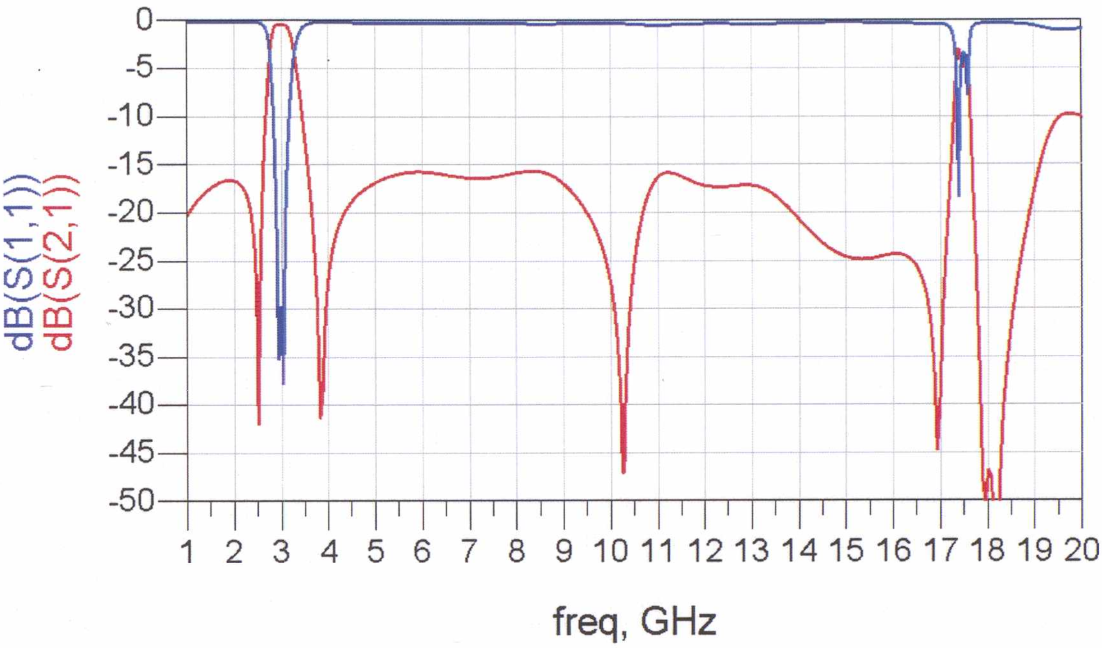

Figure 5. 18 Simulated response of the filter with effect the L-shaped slots in the patched triangles.

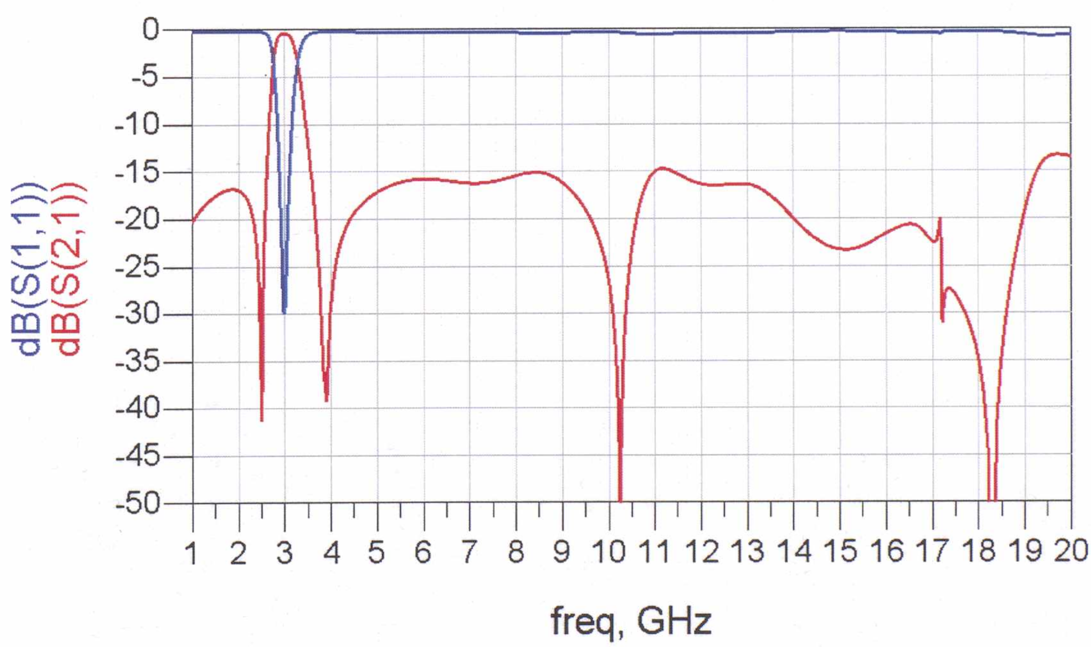

Figure 5. 19 Simulated response of the filter with effect of the open stubs.

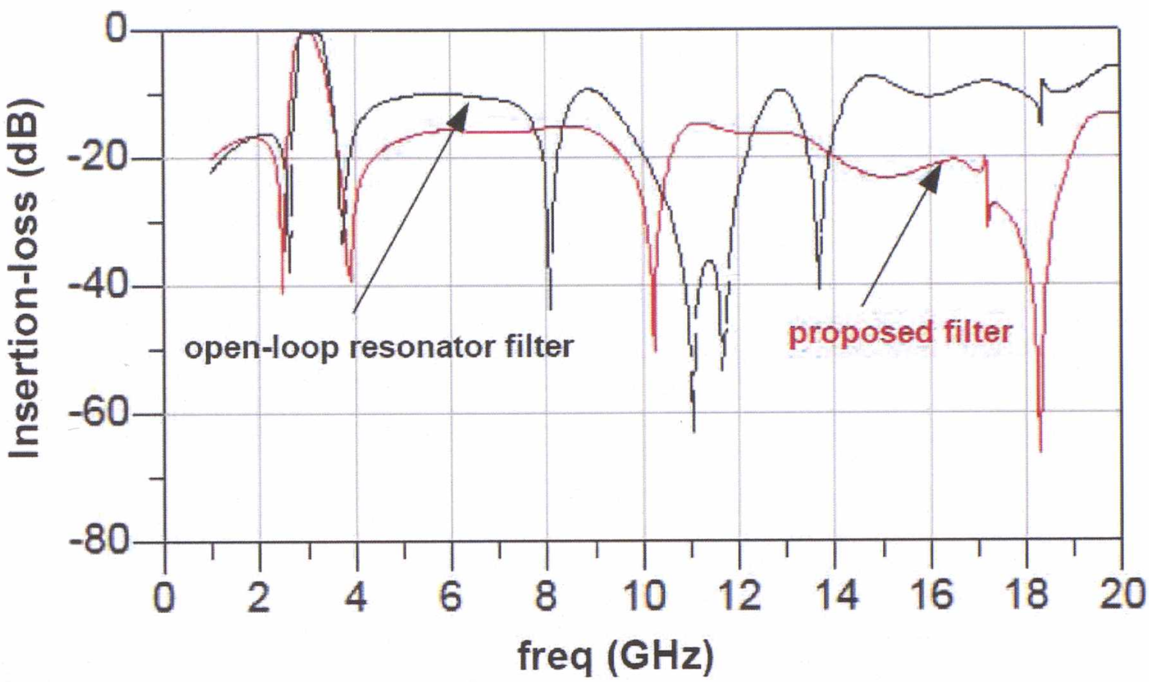

Figure 5. 20 Simulated insertion-loss response comparison of a traditional open-loop resonator filter with the proposed filter.

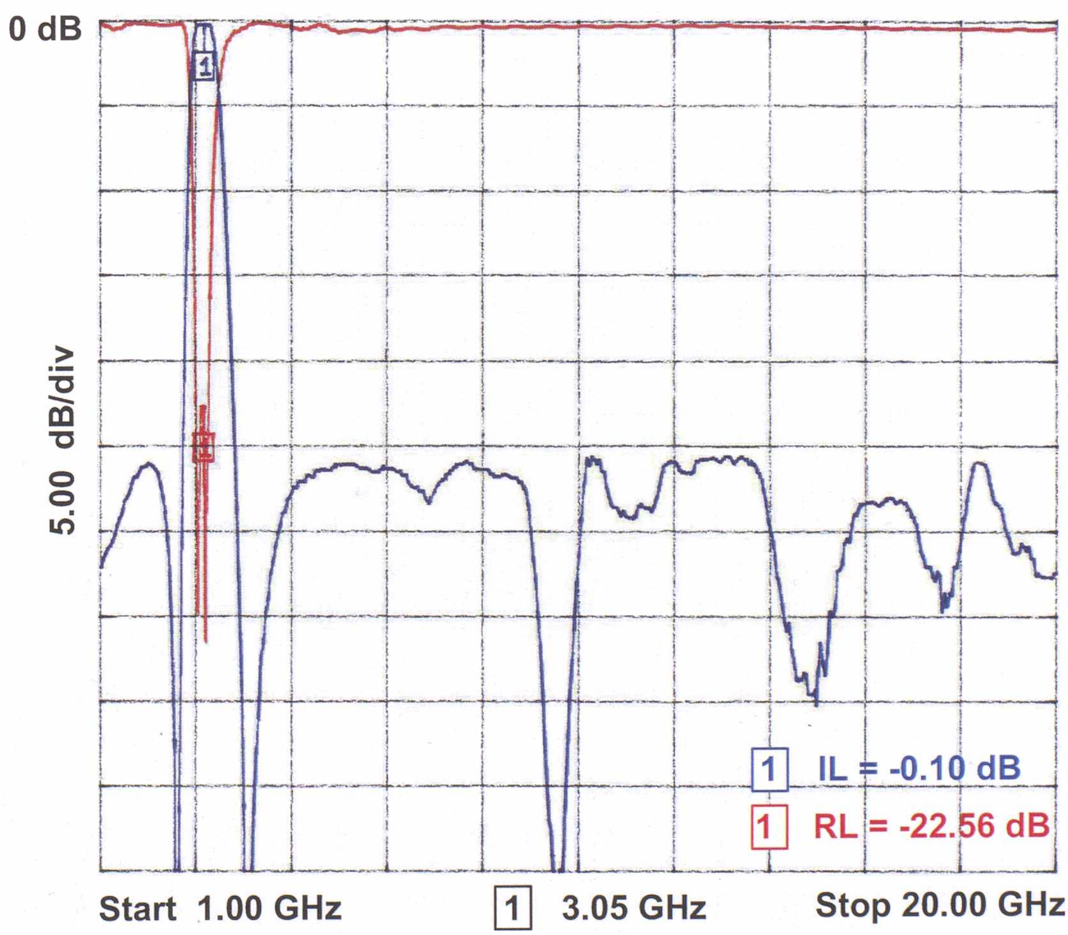

Figure 5. 21 Measured wideband insertion-loss and return-loss response of the proposed filter.

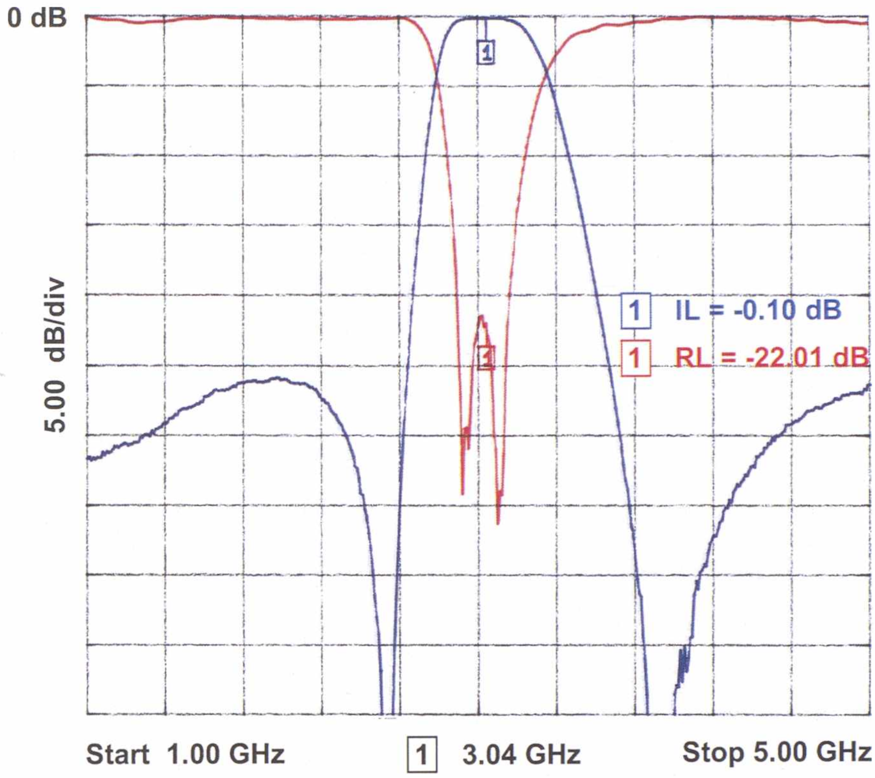

Figure 5. 22 Measured narrowband insertion-loss and return-loss performance of the proposed filter.

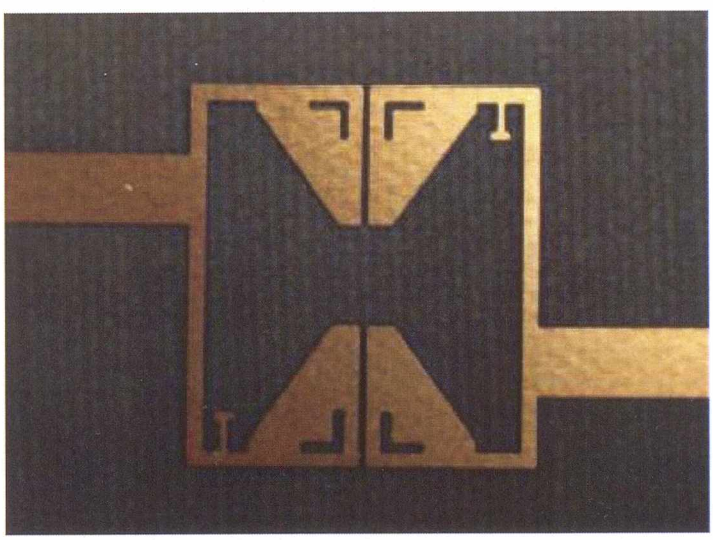

Figure 5. 23 Photograph of the fabricated ultra-wideband filter.

5.5 Miniature Quasi-Elliptic Bandpass Filter

A novel compact bandpass filter is described using stepped impedance resonator concept. The filter was designed at 2.30 GHz and achieved a sharp passband response, an excellent return-loss (18.2 dB) and insertion-loss (0.57 dB), as well as a very wide stop band rejection of >-15 dB across 1 to 8.8 GHz ($4f_o$). In addition the filter has a compact size of $0.124\lambda_o \times 0.124\lambda_o$. This filter was simulated and manufactured to verify its performance. The measured performance of the filter exhibits a significant improvement over [15] as well as that reported recently in [16], where the 2.22 GHz filters' insertion-loss is 1.75 dB, return-loss is 18 dB and its size is more than double (i.e. $0.32\lambda g \times 0.32\lambda g$) that obtained here even though the filters in [15] and [16] were constructed on a higher dielectric constant material ($\varepsilon_r = 3.38$ and $h = 0.8$ mm).

5.5.1 Filter Design

The proposed filter comprises of two half-ring resonators whose ends are in the form of a closed loop quadrant which is inverted and whose straight sides are closely spaced to each other. The characteristic impedance of the closed loop quadrant sides is lower than the rest of resonator to provide the necessary capacitance loading to miniaturise the resonator. The two resonators are located close to each other so that they are electromagnetically coupled to create a two-pole BPF. The geometry of the proposed filter is shown in Figure 5.24. The location of the two feed lines are located at the intersection of arc lengths θ_1 and θ_2, that determine the two transmission zeroes close to the filter passband. The frequency of these transmission zeros are approximately given by [17]:

$$f_1 \approx \frac{nc}{4\theta_1\sqrt{\varepsilon_{eff}}} \text{ and } f_2 \approx \frac{nc}{4\theta_2\sqrt{\varepsilon_{eff}}} \qquad n = 1, 3, 5 \ldots \qquad (5.7)$$

Where ε_{eff} is the effective dielectric constant, n is the mode number, c is the speed of light in free space.

A two-pole microstrip bandpass filter was designed at the fundamental resonant frequency of 2.2 GHz using the proposed resonator structure. The dimensions of the filter as defined in Figure 5.24 are: input/output feed lines $W_3 = 2$ mm; arc lengths $\theta_1 = 1$ mm, $\theta_2 = 9.5$ mm; arc radius $R_1 = 5.2$ mm, $R_2 = 6.2$ mm; coupling gap $S_1 = 0.2$ mm, $S_2 = 0.4$ mm; and width $W_1 = 0.7$ mm, $W_2 = 1.3$ mm, $W_4 = 0.5$ mm. The filter has an overall size of 12.4×12.4 mm^2, i.e. $0.124\lambda g \times 0.124\,\lambda g$, where λg is the guide wavelength at 2.2 GHz.

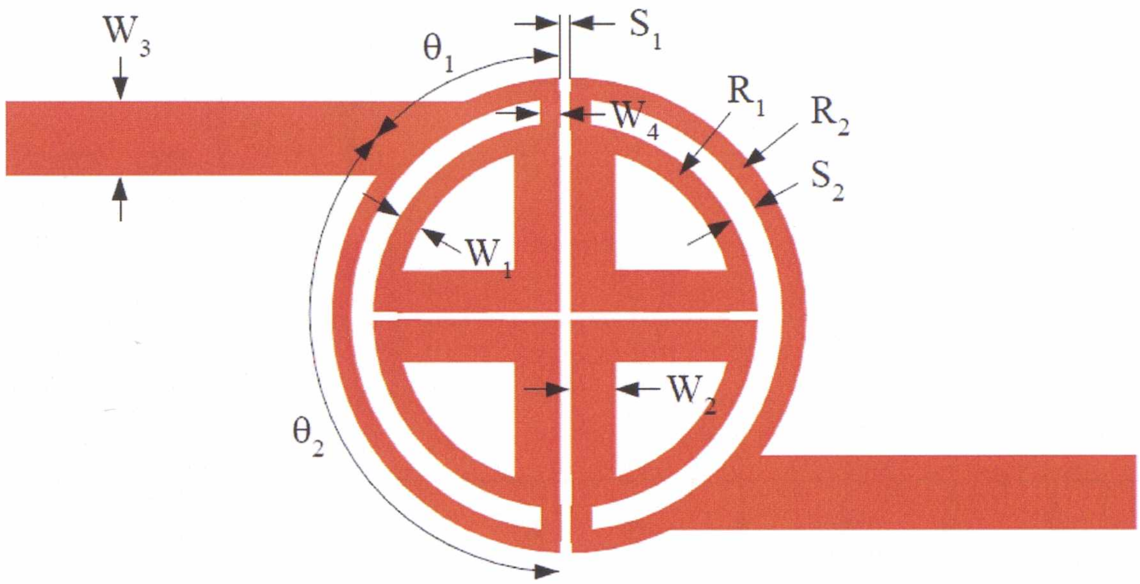

Figure 5. 24 Layout of the Miniature Quasi-Elliptic Bandpass Filter

5.5.2 Simulation and Measured Results

Figure 5.25 shows the simulated transmission and return-loss responses of the filter. Its insertion-loss and return-loss are 0.33 dB and 25 dB, respectively, at the filters centre frequency of 2.2 GHz. The two transmission zeros adjacent to the filters passband are realised at 1.9 and 2.6 GHz with attenuation about 50 dB; additionally, a third transmission zero is located at 5.1 GHz with attenuation better than 50 dB. The stop-band rejection is better than -15 dB from 1 to about 7.7 GHz. Figure 5.26 shows the measured transmission and return-loss responses of the filter centred at 2.30 GHz. Its passband return-loss is better than -18.2 dB and the insertion-loss is better than 0.57 dB. Its stop-band extends to 8.8 GHz with a rejection better than -15 dB. It can be observed that good agreement between the simulation and measured results is obtained. The slight discrepancy is attributed to fabrication tolerance.

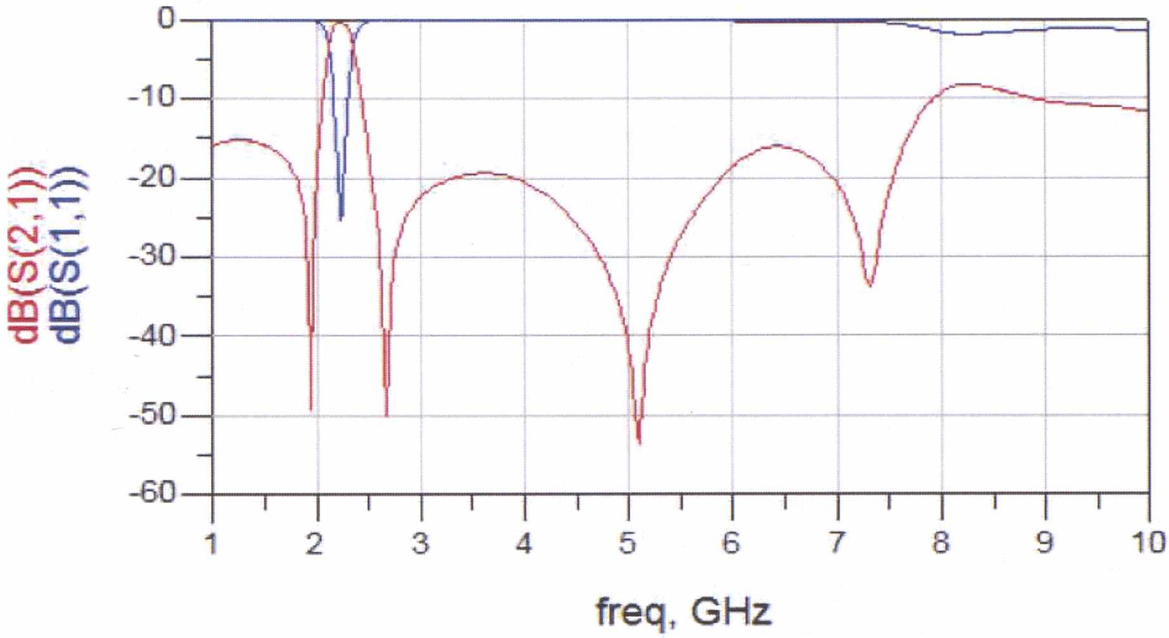

Figure 5. 25 Simulated transmission and return-loss characteristics of the proposed filter.

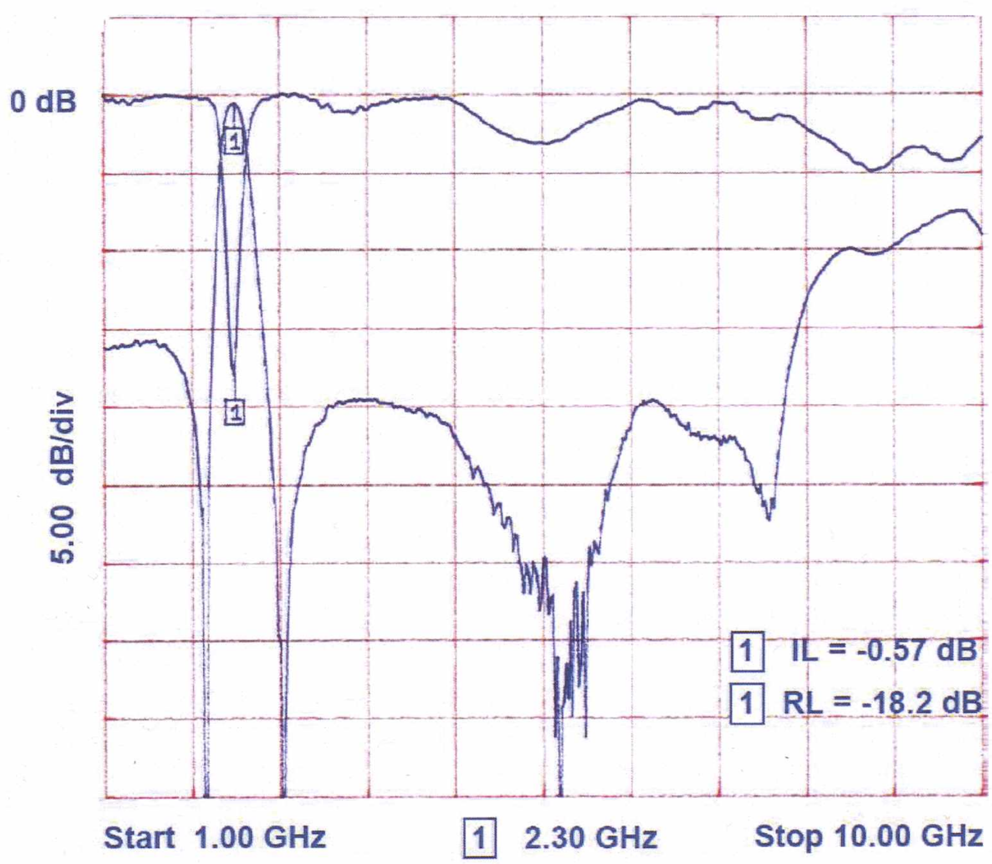

Figure 5. 26 Measured transmission and return-loss characteristics of the proposed filter.

5.6 References

[1] J.T. Kuo, S.P. Chen, and M. Jiang, "Parallel-coupled microstrip filters with overcoupled end stages for suppression of spurious responses," *IEEE Microw. Wireless Compon. Lett.*, vol. 13, no. 10, pp. 440–442, Oct. 2003.

[2] T. Lopetegi, M.A.G. Laso, J. Hernández, M. Bacaicoa, D. Benito, M.J. Garde, M. Sorolla, and M. Guglielmi, "New microstrip wiggly-line filters with spurious passband suppression," *IEEE Trans. Microw. Theory Tech.*, vol. 49, no. 9, pp. 1593–1598, Sep. 2001.

[3] J.T. Kuo and E. Shih, "Microstrip stepped impedance resonator bandpass filter with an extended optimal rejection bandwidth," *IEEE Trans. Microw. Theory Tech.*, vol. 51, no. 5, pp. 1554–1559, May 2003.

[4] K. U-yen, E.J. Wollack, T. A. Doiron, J. Papapolymerou, and J. Laskar, "A planar bandpass filter design with wide stopband using double split-end stepped-impedance resonators," *IEEE Trans. Microw. Theory Tech.*, vol. 54, no. 3, pp. 1237–1244, Mar. 2006.

[5] C.W. Tang and H.H. Liang, "Parallel-coupled stacked SIRs bandpass filters with open-loop resonators for suppression of spurious responses," *IEEE Microw. Wireless Compon. Lett.*, vol. 15, no. 11, pp. 802–804, Nov. 2005.

[6] S.Y. Lee and C.M. Tsai, "New cross-coupled filter design using improved hairpin resonators," *IEEE Trans. Microw. Theory Tech.*, vol. 48, no. 12, pp. 2482–2490, Dec. 2000.

[7] J.G. García, F. Martín, F. Falcone, J. Bonache, I. Gil, T. Lopetegi, M.A.G. Laso, M. Sorolla, and R. Marqués, "Spurious passband suppression in microstrip coupled line bandpass filters by means of split ring resonators," *IEEE Microw. Wireless Compon. Lett.*, vol. 14, no. 9, pp. 416–418, Sep. 2004.

[8] W.H. Tu and K. Chang, "Compact microstrip bandstop filter using open stub and spurline," *IEEE Microw. Wireless Compon. Lett.*, vol. 15, no. 4, pp. 268–270, Apr. 2005.

[9] W.H. Tu and K. Chang, "Compact second harmonic-suppressed bandstop and bandpass filters using open stubs," *IEEE Trans. Microw. Theory Tech.*, vol. 54, no. 6, pp. 2497–2502, Jun. 2006.

[10] C.W. Tang and M.G. Chen, "Wide stopband parallel-coupled stacked SIRs bandpass filters with open-stub lines," *IEEE Microw. Wireless Compon. Lett.*, vol. 16, no. 12, pp. 666–668, Dec. 2006.

[11] C.W. Tang and Y.K. Hsu, "Design of a wide stopband microstrip bandpass filter with asymmetric resonators," *IEEE Microw. Wireless Compon. Lett.*, vol. 18, no. 2, pp.91–93, Feb. 2008.

[12] M.D.C. Velazquez, J. Martel, and F. Medina, "Parallel coupled microstrip filters with ground plane aperture for spurious band suppression and enhanced coupling," *IEEE Trans. Microw. Theory Tech.*, vol. 52, no. 3, pp. 1082–1086, Mar. 2004.

[13] C. Quendo, E. Rius, C. Person, and M. Ney, "Integration of optimized low-pass filters in a bandpass filter for out-of-band improvement," *IEEE Trans. Microw. Theory Tech.*, vol. 49, no. 12, pp. 2376–2383, Dec. 2001.

[14] C.W. Tang, Yen-Kuo Hsu, "A microstrip bandpass filter with ultra-wide stopband", *IEEE Trans. Microw. Theory Tech.*, vol. 56, no. 6, pp.1468–1472, June 2008.

[15] Li, J.L., Chen, J.X., Wang, J.P., Shao, W., Xue, Q., Xue, L.J.: "Miniaturised microstrip bandpass filter using stepped impedance ring resonators", IEE Electronic Letters 2004, Vol. 40, No 22.
[16] Wang, Y., Wang, B-Z, Wang, J.: "The design of coupled resonator bandpass filter with wide stop band", IEEE microwave and wireless components letters Vol.18, No.4, 2008.
[17] Chang, K., Hsieh, L.H., Microwave Ring Circuits and Related Structures, 2004 John Wiley & Sons.

Chapter 6 Dual-band bandpass filter structures

6.1 Introduction

The increasing demands of wireless communication applications necessitates RF transceivers to operate in multiple separated frequency bands so that users can access various services with a single multimode handset or terminal. For example, global systems for mobile communications (GSMs) operate at both 900 and 1800 MHz, wireless code-division multiple-access (WCDMA) operate at 2 GHz. IEEE 802.11b and IEEE 802.11a wireless local area network (LAN) products operate in the unlicensed industrial, scientific medical (ISM) bands of 2.4 and 5 GHz. Hence, dual-band filters are recently receiving much attention. One way [1] of designing a dual-band filter is to combine two bandpass filters designed for two different passband responses. However, this requires an implementation area twice that of a single-band filter and additional external combining networks. Thus, an integrated filter with a dual passband response is more attractive. There are several approaches reported to date in the design of an integrated dual passband filter [2]–[6]. Parallel-coupled line dual-band BPF has been presented in [2] using stepped-impedance resonators (SIRs) with sinuous configuration to reduce size, two resonance frequencies of which can be controlled by the impedance ratio and electrical length of two sections. In [3], a dual-band BPF using pseudo-inter-digital SIRs is proposed and is more compact than the filter in [2]. On the other hand, element-loaded resonators are attracting more and more interest for their application in constructing dual-band response. For example, in [4] and [5], stub-loaded open-loop resonators are proposed to design dual-band filters. Capacitor loaded pseudo-inter-digital filter is proposed in [6]. By regulating the value of the capacitor, the central frequency of its second passband can be tuned without affecting the central frequency of the first passband.

In this chapter two novel structures are proposed for microstrip dual-band bandpass filter applications. The first structure was developed by modifying the open-loop 'C-shape' resonator described in Chapter 4. The upper passband of the proposed filters have the ability to be tuned relative to the lower passband. To realise higher skirt selectivity spur-line is used to create additional transmission zero. The second structure was devised with the assistance of symmetric resonators interconnected with an inter-digital capacitor. It is demonstrated that it is possible to change the single-band bandpass filter to a dual-band bandpass filter by changing the parameters of the inter-digital capacitor. The filter exhibits a high selectivity and its second passband response can be precisely controlled relative to the first passband over a large frequency range by a factor of $1.51f_o$, where f_o is centre frequency of the primary passband. The performance of both filters was verified experimentally.

6.2 Dual-Band Bandpass Filter Using Stub-Loaded Open Loop Resonator

6.2.1 Filter Design

The proposed dual-band bandpass filter shown in Figure 6.1(a) consists of a modified open loop C-shape resonator. Compared to the conventional open-loop C-shape resonator, the resonator has extra closed loops and an open stub loaded inside one of the closed loop. This allows dual-band operation without any increase in the dimensions of the resonator. The centre frequency of the first passband is determined by the entire length of the open loop resonator, whereas the length of the internal open loop resonator determines the second passband. These frequencies are approximately calculated as

$$f_1 = \frac{2nc}{3L_a\sqrt{\varepsilon_{eff}}} \quad \text{and} \quad f_2 = \frac{nc}{L_b\sqrt{\varepsilon_{eff}}} \qquad n = 1, 3, 5\ldots \tag{6.1}$$

Where ε_{eff} is the effective dielectric constant, n is the mode number, c is the speed of light in free space, L_a = L7 + L8 and L_b = L7 + L8 - 2×L6. Figure 6.2 shows the simulated response of the dual-band filter in Figure 6.1.

Both passband frequencies given by (6.1) are obtained from the same resonator. In order to make the second passband independent from the first passband response open-end stubs in a 'T-shape' are introduced as shown in Figure 6.1(b). Therefore, in addition to the open loop length, which determines the centre frequency of the first passband, the length and the width of the 'T-shape' open stub determines the frequency of the second passband. The bandwidth of the passband depends upon the external quality factor and the coupling coefficients between the two resonators. In particular, the coupling gap S and length L5 determine the bandwidths.

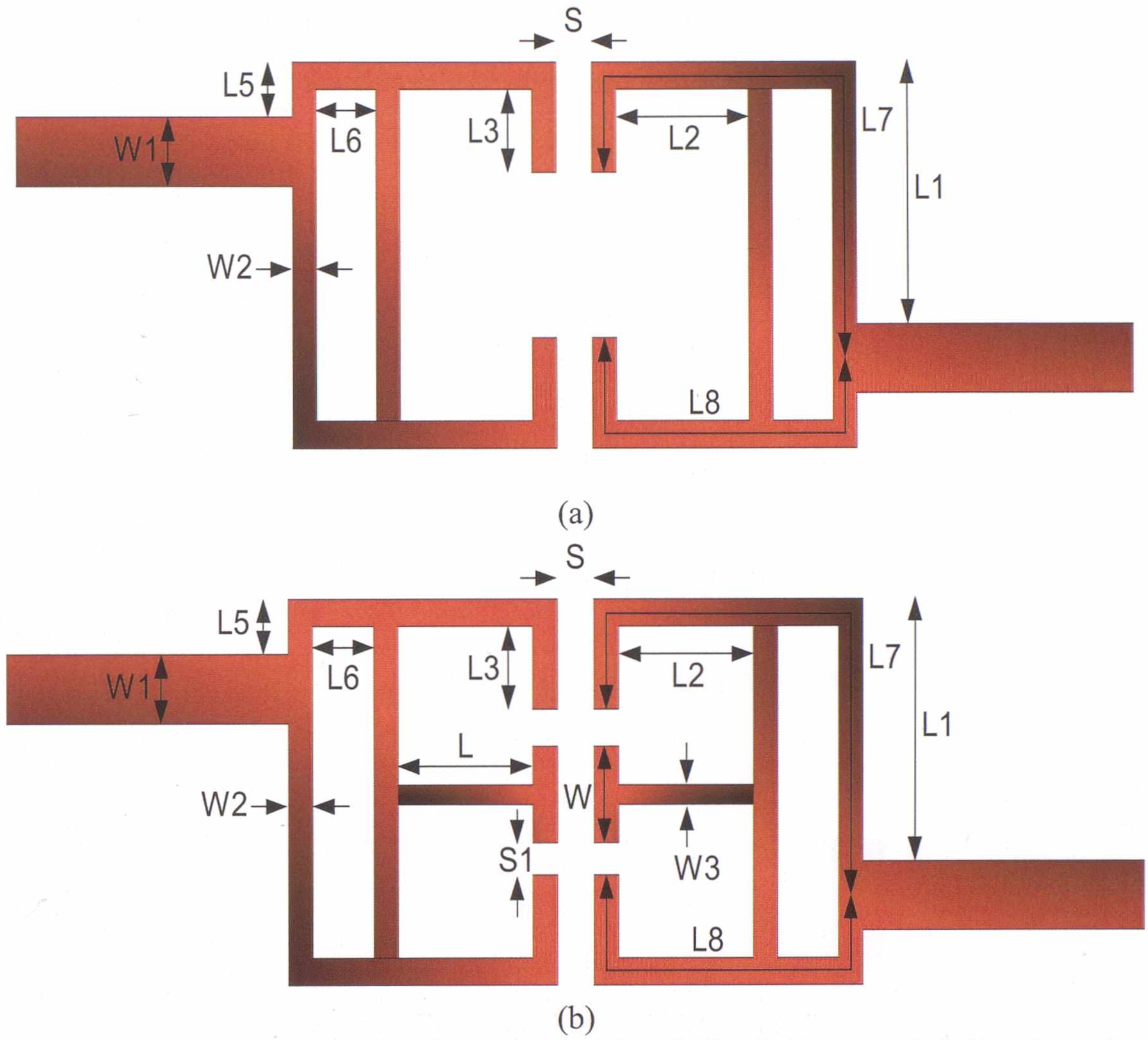

Figure 6.1 (a) Layout of the proposed dual-band filter without stubs, (b) with stub loading.

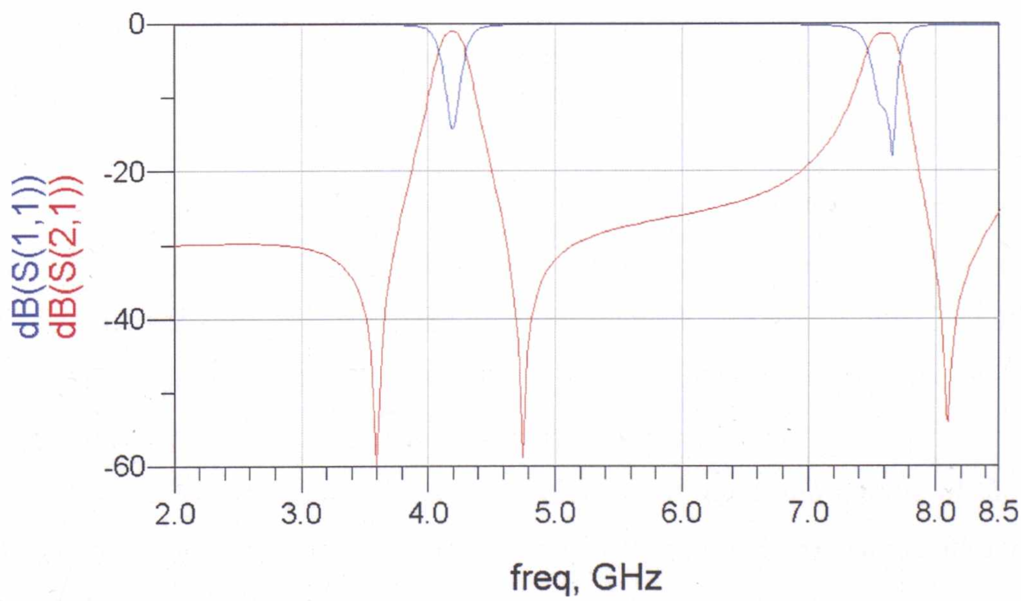

Figure 6. 2 The simulated response of the proposed dual-band filter without stub.

6.2.2 Theoretical Analysis of Stub-Loaded Resonator

The analysis of the generalised stub-loaded resonator (SLR) in Figure 6.1(b) was developed with reference to [7] in order to determine its effect on the first and second passband responses.

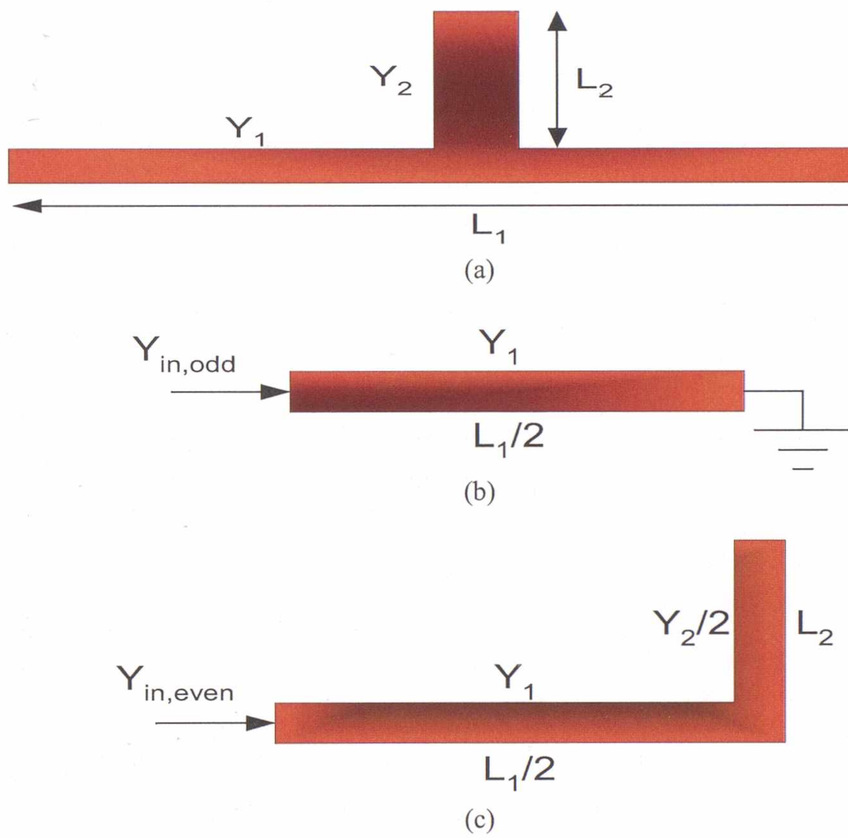

Figure 6. 3 (a) Structure of the stub-loaded resonator, (b) odd-mode equivalent circuit, and (c) even-mode equivalent circuit.

The proposed SLR comprises of a half-wavelength resonator and an open stub. With reference to Figure 6.3, Y_1, L_1, Y_2 and L_2 denote the characteristic admittances and lengths of the microstrip line and open stub, respectively. The open stub is shunted at the midpoint of the microstrip line to obtain a symmetrical in structure, therefore odd- and even-mode analysis can be adopted to characterize it.

For odd-mode excitation, there is a voltage null along the middle of the SLR. This leads to the approximate equivalent circuit of Figure 6.3 (b). The resulting input admittance for odd-mode can be expressed as

$$Y_{in,odd} = \frac{Y_1}{j\tan(\theta_1/2)} \tag{6.2}$$

Where $\theta_1 = \beta L_1$ is the electrical length of the microstrip line. From the resonant condition of $Y_{in,odd} = 0$, the odd mode frequency can be deduced as

$$f_{odd} = \frac{(2n-1)c}{L_1\sqrt{\varepsilon_{eff}}} \qquad n = 1, 3, 5\ldots \tag{6.3}$$

It can be observed that the odd-mode resonant frequencies are not affected by the open stub. For even-mode excitation, there is no current flow through the symmetrical plane. Thus we can bisect the circuit with open circuits at the middle to obtain the equivalent circuit of Figure 6.3(c). Ignoring the discontinuity of the folded section, the input admittance for even-mode can be approximately obtained as

$$Y_{in,even} = jY_1 \frac{2Y_1 \tan(\theta_1/2) + \tan(\theta_2)}{2Y_1 - Y_2 \tan(\theta_1/2)\tan(\theta_2)} \tag{6.4}$$

Where $\theta_2 = \beta L_2$ is the electrical length of the open stub. The resonant condition is $Y_{in,even} = 0$. Thus, at the even-mode resonant frequencies, it can be derived as

$$cot(\theta_1/2)tan(\theta_2) = -\frac{2Y_1}{Y_2} \tag{6.5}$$

According to Equation (6.5) it can be noticed that the even mode frequency is a function of L_1, L_2, and the ratio of Y_1/Y_2.

Therefore applying (6.5) to this proposed filter the upper passband can be easily controlled by changing the width of the stub (W3) or changing the length of the stub (L), without altering resonator's width. Figure 6.4 and Figure 6.5 shows how the upper passband can be controlled by changing the parameters W3 and L, respectively, without affecting the lower passband response.

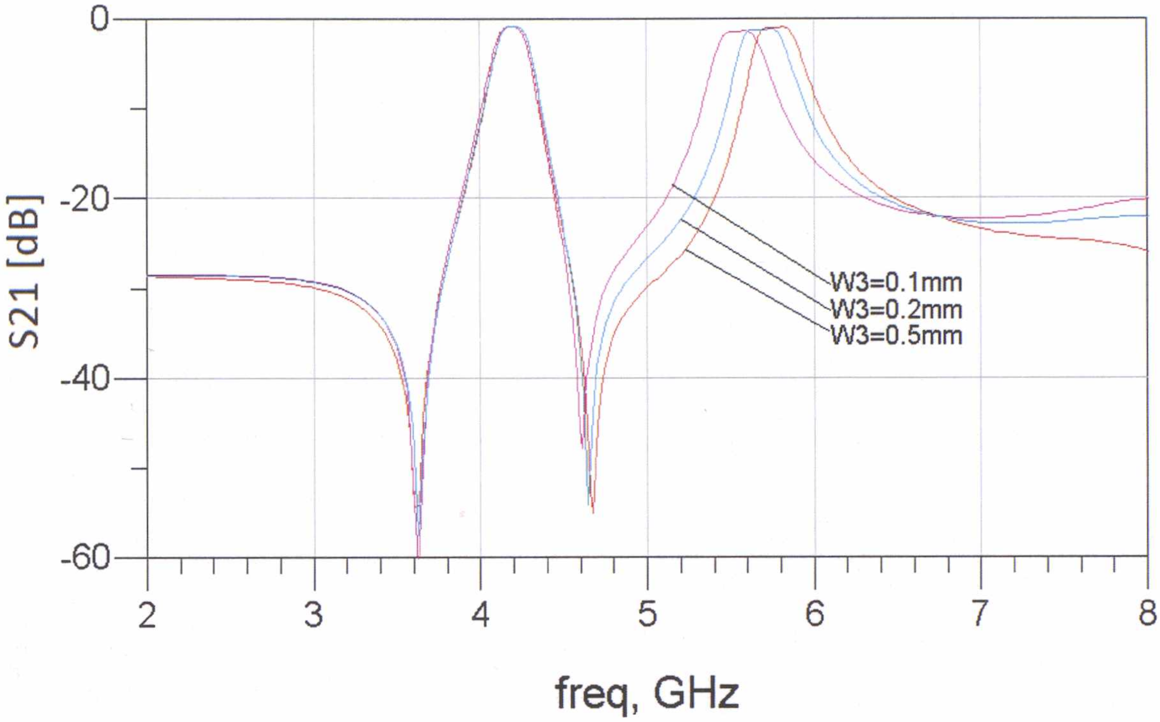

Figure 6. 4 Changing the centre frequency of the upper passband by changing the width of the stub.

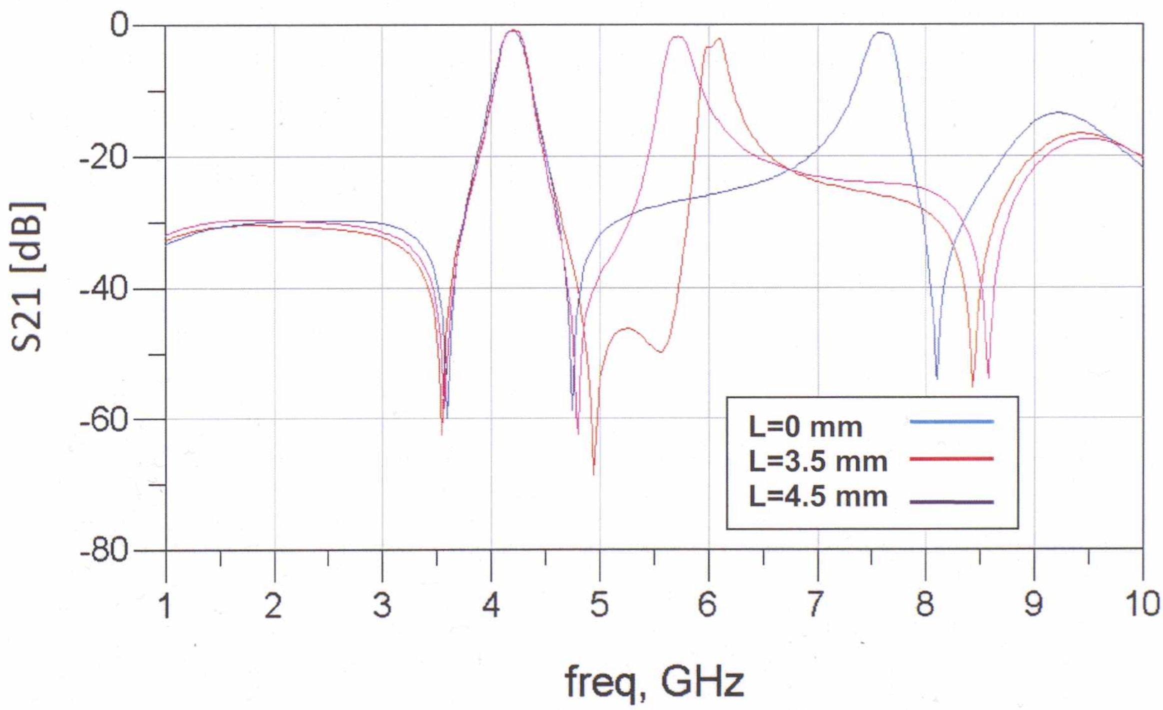

Figure 6. 5 Changing the centre frequency of the upper passband by changing the length of the stub.

6.2.3 Simulation and Measurement

To validate the feasibility of the proposed bandpass filter with stubs, it has been designed for a lower passband resonant frequency of 4.15 GHz and an upper passband frequency of 5.59 GHz, see Figure 6.7. To achieve this upper passband the length of the stub is L = L2 = 4 mm. However, when the stub length is made of zero the upper passband is at 7.38 GHz, see Figure 6.8. Other dimensions of the filter are: L1 = 9.5 mm, L2 = 4 mm, L3 = 4 mm, L4 = 7 mm, L5 = 3.5 mm, L6 = 1.6 mm, L7 = 21 mm, L8 = 15.4 mm, W2 = 0.5 mm, W1 = 2.4 mm, W = 4.5mm, S1 = 1 mm, and S = 1.2 mm.

Figure 6.6 and 6.7 shows the simulation and the measured results, respectively, with W3 = 0.5 mm. The measured result shows the filter has two passband responses centred at 4.15 and 5.59 GHz with a high out-of-band rejection. For the lower passband the insertion-loss is less than 1 dB, and return-loss is greater than 20 dB. In the case of the upper passband, its insertion-loss is about 1.8 dB, and return-loss is more than 10 dB. Three transmission zeros are realised with more than 40 dB attenuation. All stopband obtain the rejection levels of about 20dB. The correlation with the simulation results is remarkable. The simulated response in Figure 6.6 has insertion-loss and return-loss of 0.9 dB and 17 dB, respectively, for the lower passband. The insertion-loss and return-loss for the upper passband are 1.9 dB and 9.9 dB, respectively. Slight deviation is observed, which is attributed to fabrication tolerance of the filter.

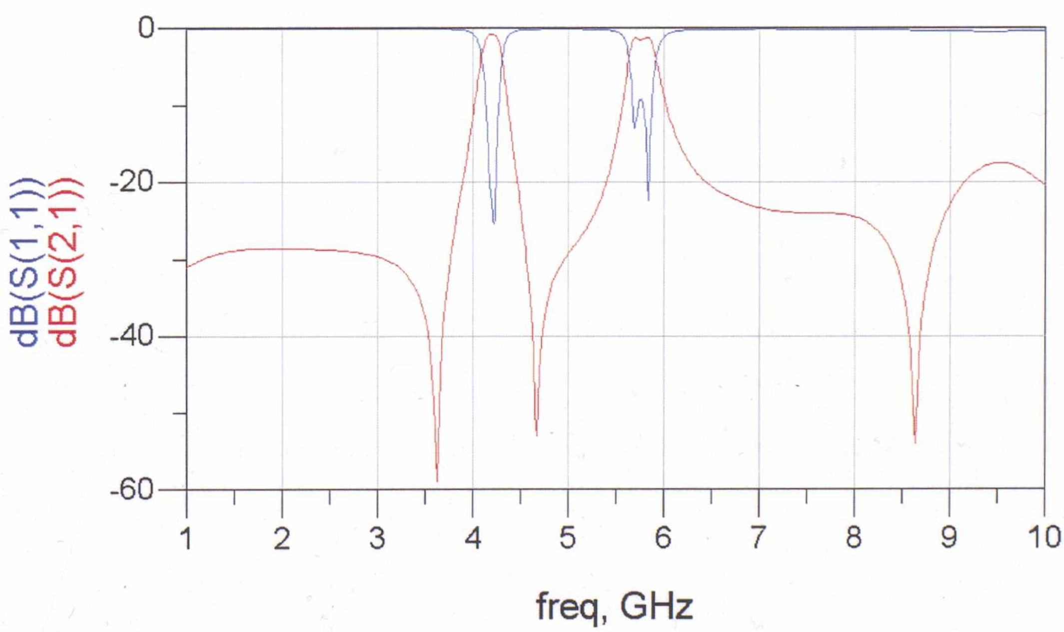

Figure 6. 6 Simulated results of the proposed dual-band filter with W3 = 0.5 mm.

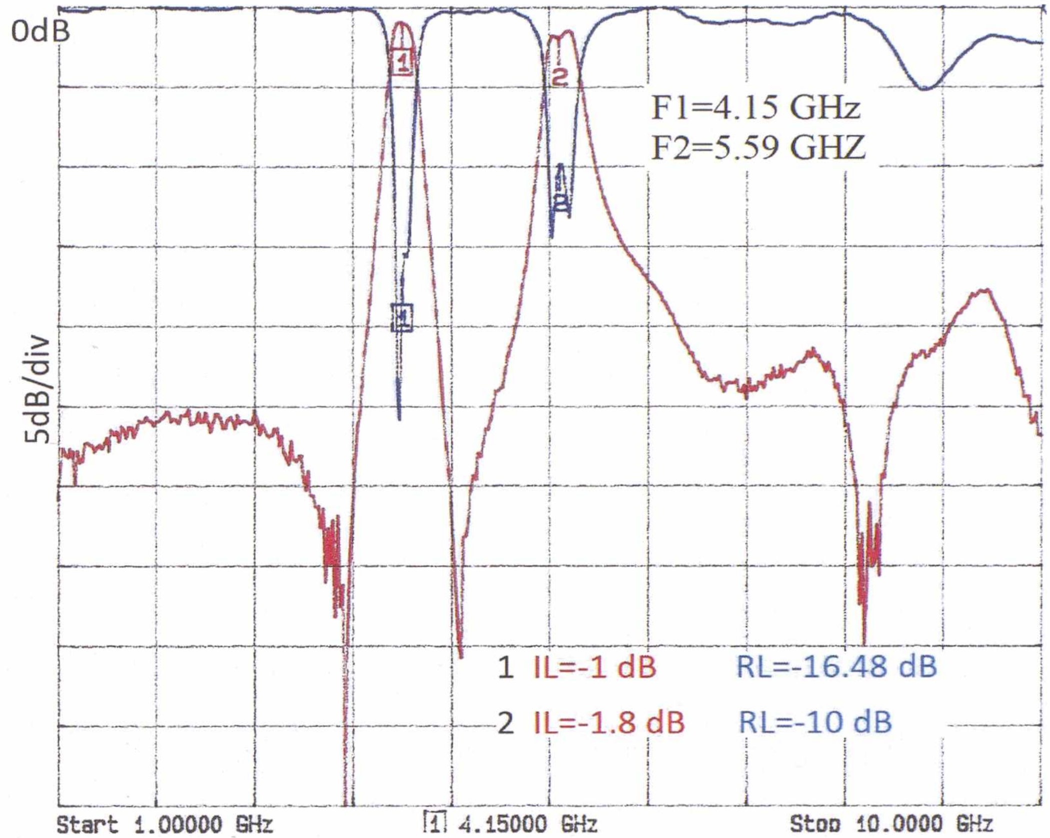

Figure 6. 7 Measured results of the proposed dual-band filter with W3 = 0.5 mm. Scale: for IL is 5 dB/div; for RL is 3 dB/div

Figure 6.2 and 6.8 shows the simulation and the measured results, respectively, of the proposed dual band bandpass filter without a stub. Referring to the measured results in Figure 6.8 the two passband responses are located at 4.15 GHz and 7.38 GHz with high out-of-band rejection. For the lower passband the insertion-loss is 0.9 dB and the return-loss is more than 19.43 dB. In the case for the upper passband the insertion-loss is about 4 dB and the return-loss is more than 13.40 dB. Three transmission zeros are realised with more than 35 dB attenuation. Compared with the simulation results in Figure 6.2, the correlation is good. The simulated insertion-loss and return-loss for the lower passband are 2 dB and 14 dB, respectively. For the upper passband the insertion-loss and return-loss are 2 dB and greater than 18 dB, respectively. The photographs of the dual-band filter without and with stub loading are shown in Figures 6.9 and 6.10, respectively.

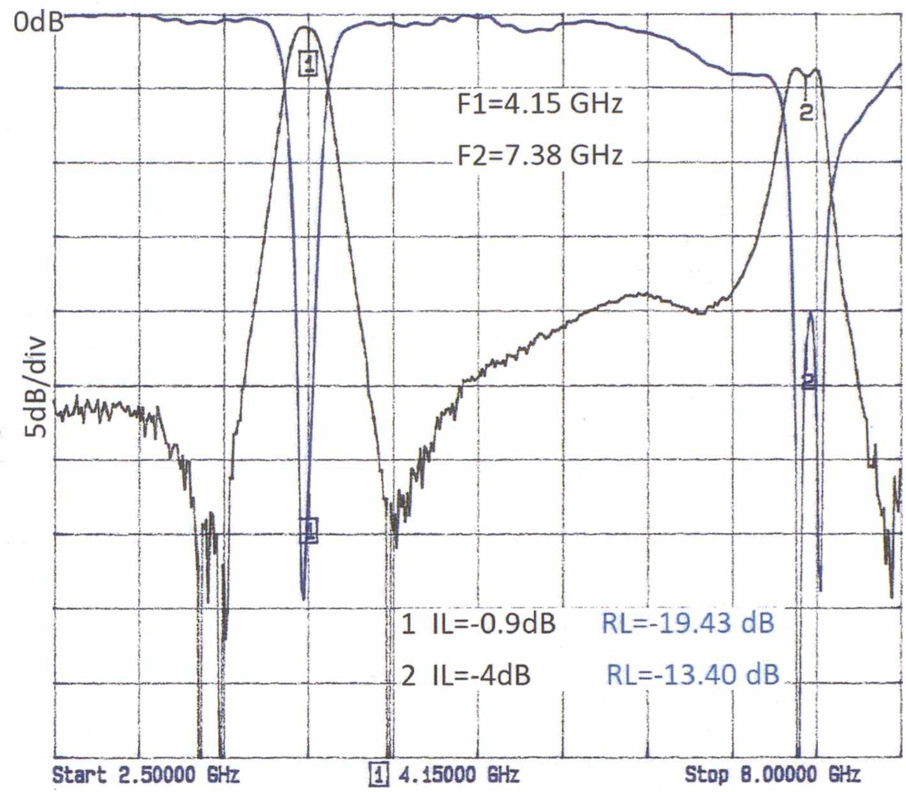

Figure 6. 8 The measured results of the proposed bandpass filter without stub. Scale: for IL is 5 dB/div; for RL is 3 dB/div

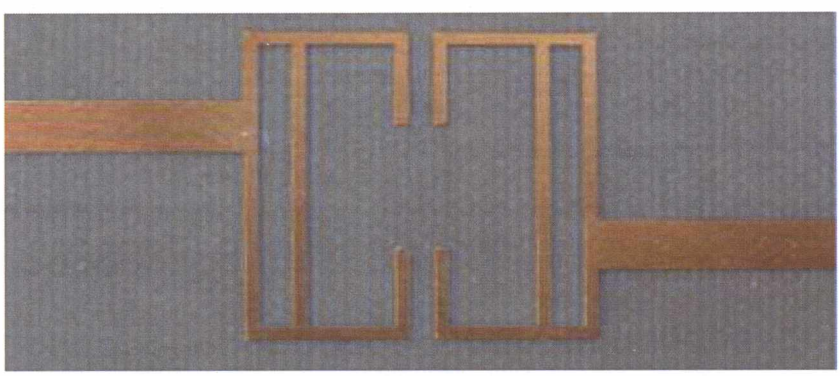

Figure 6. 9 Photograph of the proposed dual-band filter without stub.

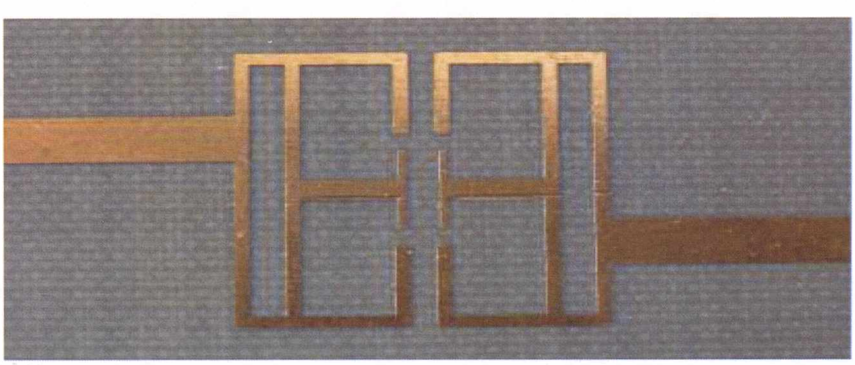

Figure 6. 10 Photograph of the proposed dual-band filter with stub loading.

6.2.4 A Dual-Band Filter with Additional Transmission Zeros

The filters in Section 6.2 exhibit three transmission zeros. If another transmission zero can be introduced then the filter's selectivity can be further improved. Spur-line technique has been proven to successfully create additional transmission zeros [8]-[9]. Hence, spur-lines are introduced in the dual-band filter design to achieve a sharper roll-off. The spur-lines are incorporated into the input and output feed lines. The resulting layout configuration of the filter is shown in Figure 6.11.

The spur-lines have a length of 7.2 mm, which approximately corresponds to the quarter guide wavelength at the frequency where the additional fourth transmission zero is required. The simulated and measured results are given in Figures 6.12 and 6.13, respectively. The simulation shows the fourth transmission zero is realised at 8.5 GHz. Two passband responses are centred at 4.2 and 5.7 GHz. The insertion-loss of the lower and upper passband is 0.9 and 1.8 dB, respectively, and their corresponding return-loss is greater than 15 dB. The measured results show an insertion-loss of 1.08 and 1.8 dB for lower and upper passband, and return-loss greater than 14 dB for both passband responses located at 4.15 and 5.62 GHz. Good agreement between the simulation and measured results is obtained.

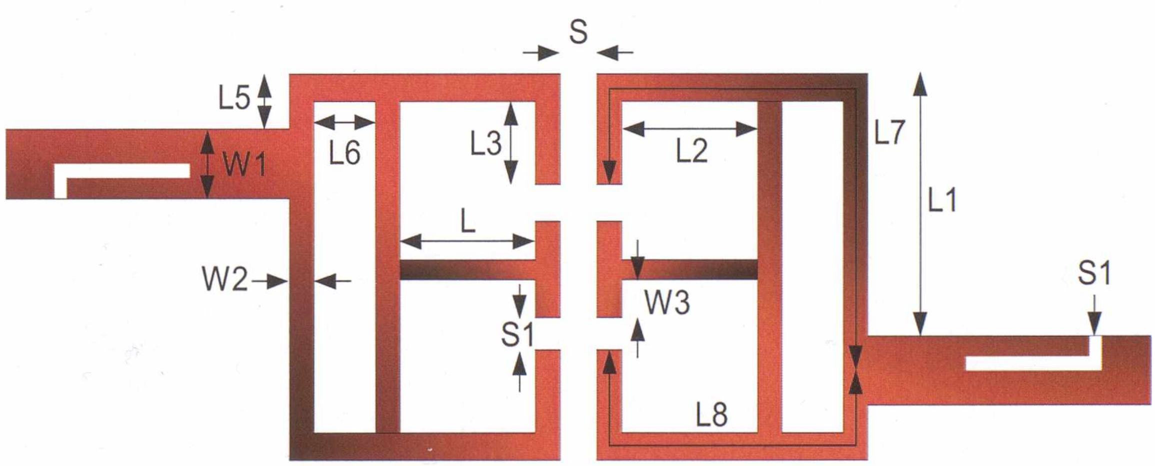

Figure 6. 11 Layout of the proposed dual-band filter with spur-lines.

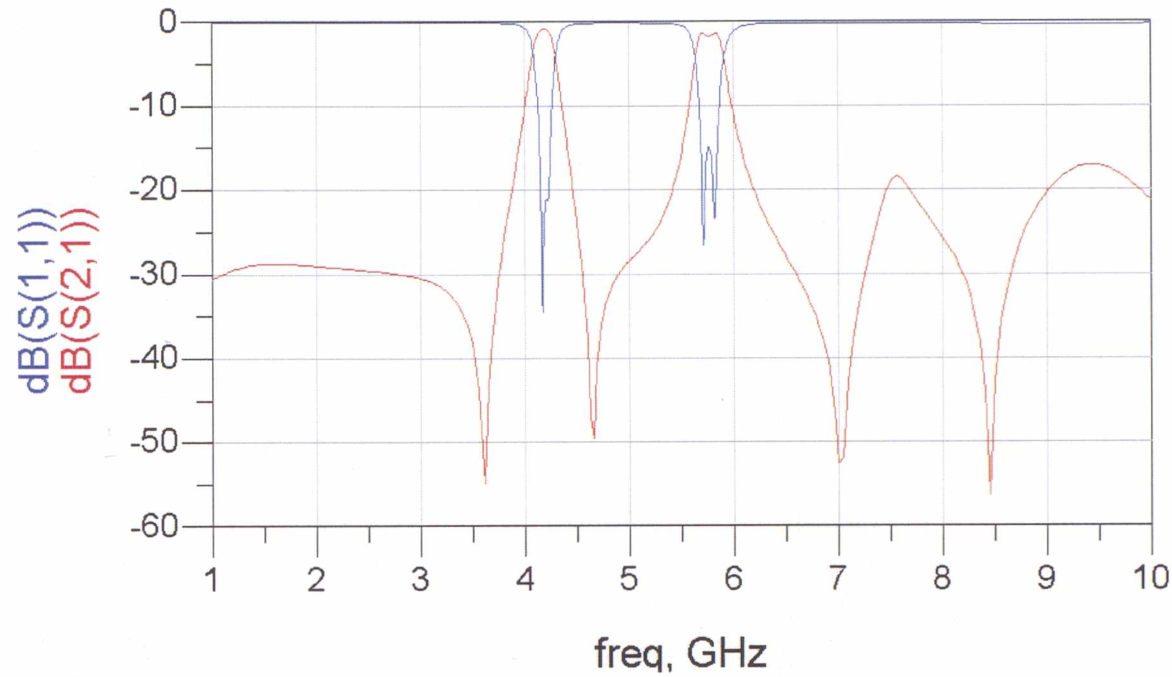

Figure 6. 12 The simulated results of dual-band filter with spur-lines.

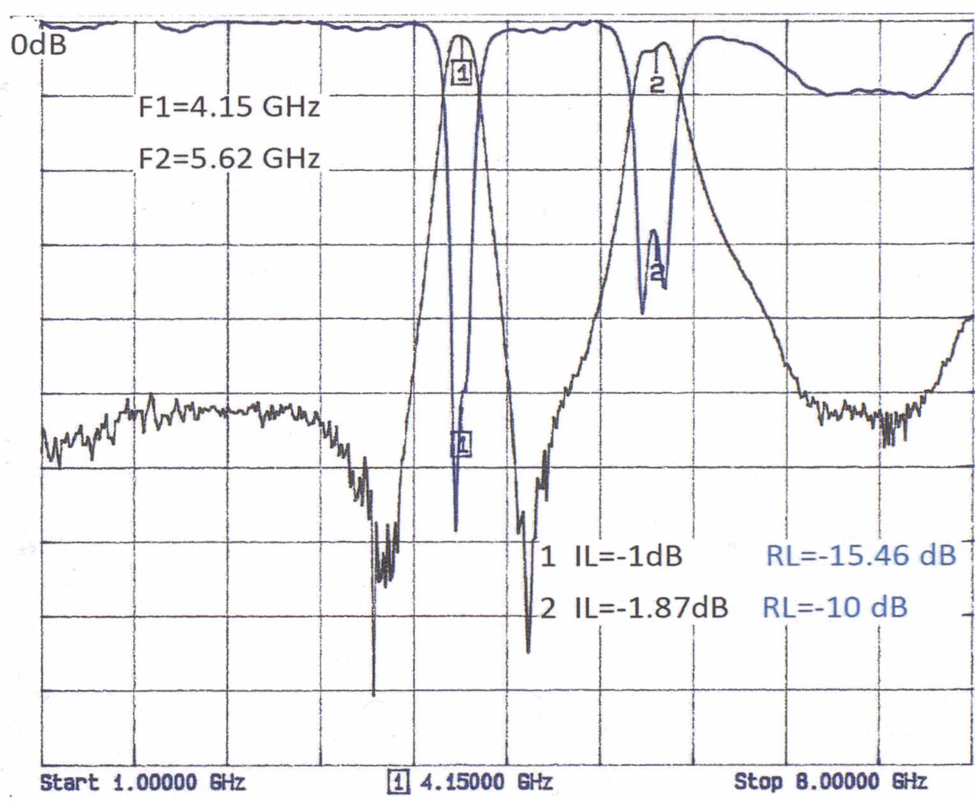

Figure 6. 13 The measured results of dual-band filter with spur-lines. Scale: for IL is 5 dB/div; for RL is 3 dB/div

6.3 Dual Passband Bandpass Filter Using Inter-Digital Capacitor

Another novel microstrip bandpass filter is proposed, as shown in Figure 6.14, which consists of two asymmetric resonators and the inter-digital capacitor. Changing the parameters of the inter-digital capacitors changes the coupling between the two resonators, and this leads to change from dual-mode single passband to single-mode dual passband bandpass filter.

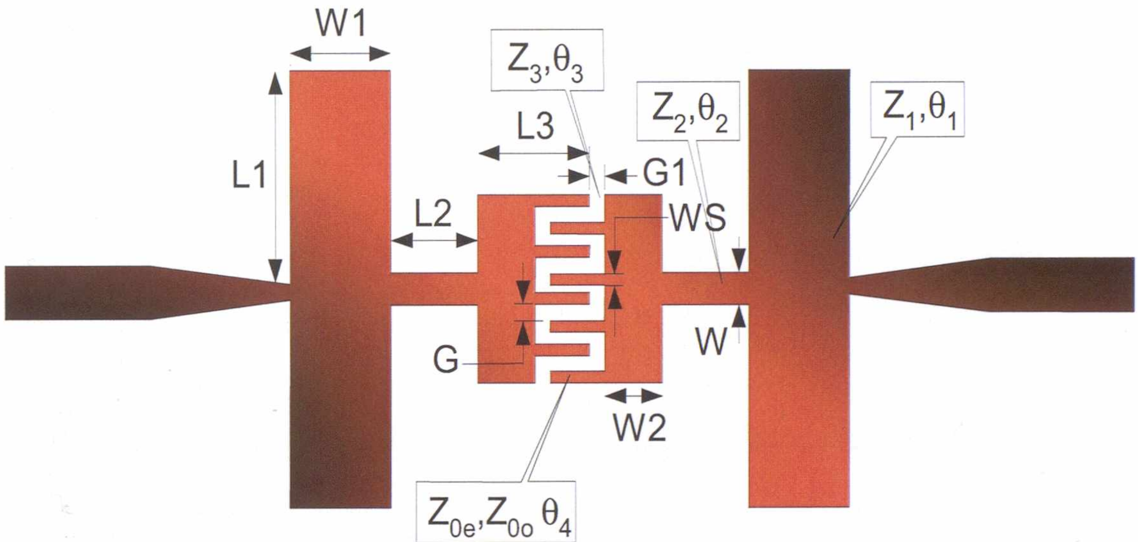

Figure 6. 14 Layout diagram of the proposed dual passband filter.

6.3.1 Theoretical Modelling of the Dual Passband Filter

The proposed bandpass filter can be transformed into the equivalent circuit shown in Figure 6.15 with the immittance inverter. The transformed admittance inverter J_{12} and J_{23} of transmission lines Z_2 and Z_3, and the even and odd-mode line admittances Y_{0e} and Y_{0o} can be derived for a lossless case as [10]:

$$J_{12} = Y_2 \csc\theta_2 \tag{6.6}$$

$$J_{23} = Y_3 \csc\theta_3 \tag{6.7}$$

$$\frac{Y_{oe}}{Y_4} = 1 - \frac{J_{34}}{Y_4}\cot\theta_4 \tag{6.8}$$

$$\frac{Y_{o_0}}{Y_4} = 1 + \frac{J_{34}}{Y_4}\cot\theta_4 \tag{6.9}$$

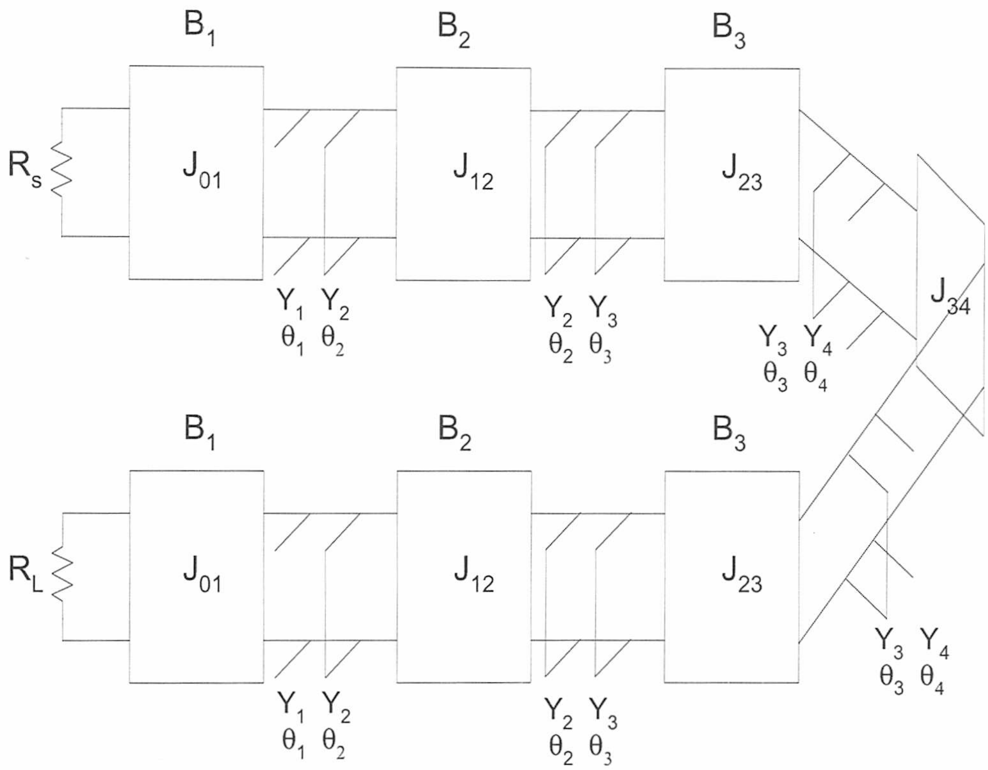

Figure 6. 15 Equivalent circuit of the proposed dual-band bandpass filter.

By matching with the generalized bandpass filter, the parameters of susceptance and susceptance slope can be than expressed as following [10]:

$$B_1 = Y_1 \tan\theta_1 - Y_2 \cot\theta_2 \tag{6.10}$$

$$B_2 = -Y_2 \cot\theta_2 - Y_3 \cot\theta_3 \tag{6.11}$$

$$B_3 = Y_4 \tan\theta_4 - Y_3 \cot\theta_3 \tag{6.12}$$

$$b_1 = \frac{\omega_o}{2}\frac{\delta B_1}{\delta\omega}\bigg|_{\omega=\omega_o} = \frac{1}{2}\left[Y_1\theta_1 \sec^2\theta_1 + Y_2\theta_2 \csc^2\theta_2\right] \tag{6.13}$$

$$b_1 = \frac{R_s g_0 g_1 J_{01}^2}{\Delta} \tag{6.14}$$

$$b_2 = \frac{\omega_o}{2}\frac{\delta B_2}{\delta\omega}\bigg|_{\omega=\omega_o} = \frac{1}{2}\left[Y_2\theta_2 \csc^2\theta_2 + Y_3\theta_3 \csc^2\theta_3\right] \tag{6.15}$$

$$J_{12} = \Delta\sqrt{\frac{b_1 b_2}{g_1 g_2}} \tag{6.16}$$

$$b_3 = \frac{\omega_o}{2}\frac{\delta B_3}{\delta\omega}\bigg|_{\omega=\omega_o} = \frac{1}{2}\left[Y_4\theta_4 \sec^2\theta_4 + Y_3\theta_3 \csc^2\theta_3\right] \qquad (6.17)$$

$$J_{23} = \Delta\sqrt{\frac{b_2 b_3}{g_2 g_3}} \qquad (6.18)$$

$$Y_1 = \frac{2b_1 - Y_2\theta_2 \csc^2\theta_2}{\theta_1 \sec^2\theta_1} \qquad (6.19)$$

$$Y_3 = \frac{2b_2 - Y_2\theta_2 \csc^2\theta_2}{\theta_3 \csc^2\theta_3} \qquad (6.20)$$

$$Y_4 = \frac{2b_3 - Y_3\theta_3 \csc^2\theta_3}{\theta_4 \sec^2\theta_4} \qquad (6.21)$$

6.3.2 Asymmetric Resonant Structure

The proposed bandpass filter in Figure 6.14 is an asymmetric structure. Hence, the resonant condition for this step impedance resonator (SIR) can be expressed as [11]:

$$R_1 = \tan\theta_1 \tan\theta_2 \qquad (6.22)$$

$$R_2(R_3 - \tan\theta_3 \tan\theta_4) = \tan\theta_2(R_3 \tan\theta_3 + \tan\theta_4) \qquad (6.23)$$

Where $R_1 = Z_1/Z_2$ $R_2 = Z_3/Z_2$ and $R_3 = Z_4/Z_3$ (6.24)

Then, it can be shown that

$$Y_1 = \frac{Y_2}{\tan\theta_1 \tan\theta_2} \qquad (6.25)$$

$$Y_4 = \frac{Y_2 - Y_3 \tan\theta_2 \tan\theta_3}{\tan\theta_4\left(\frac{Y_2}{Y_3}\tan\theta_3 + \tan\theta_2\right)} \qquad (6.26)$$

6.3.3 Design Example

In order to make it simpler and easier to fabricate, inverters J_{01} are set to $0.02(1/Y_0)$ equates to the system impedance as 50 Ω. Therefore a transmission line of 50 Ω can be directly connected to the input and output ports in this bandpass filter.

In this example the bandpass filter's specifications are:

Centre frequency = 2.66 GHz
Passband ripple = 0.01 dB
Fractional bandwidth = 6%

Furthermore, the optimised values for a given response are electrical length θ_2 and impedance Z_2 are 63.84 Ω and 21.91°, respectively.

Then the g-values are [12]:
$g_0 = 1$, $g_1 = 0.7128$, $g_2 = 1.2003$, $g_3 = 1.3212$, $g_4 = 0.6476$ and $g_5 = 1.1007$

Hence, $b_1 = 0.0638$ and $b_2 = 0.0476$.

Consequently according to (6.6)-(6.26) the electrical length θ_1, θ_2 and θ_4 and the impedance Z_1, Z_3, Z_{0e} and Z_{0o} of the proposed bandpass filter can be calculated by using MATLAB or any other root searching program. (The MATLAB code used to calculate the filter parameters is given in the Appendix II). The electrical length θ_1, θ_2 and θ_4 and the impedance Z_1, Z_3, Z_{0e} and Z_{0o} obtained are: 53.18°, 26.17°, 17.73°, 29.98°, 45 Ω, 160.7 Ω and 157 Ω, respectively.

According to (6.27)-(6.28) or Linecal in ADS can be used to determine the physical dimensions of the proposed bandpass filter shown if Figure 6.12. The dimensions obtained are: W = 1.7 mm, W1 = 5 mm, W2 = 2.9 mm, L1 = 12 mm, L2 = 5.1 mm, L3 = 7.2 mm, G1 = 1.7 mm, G = 0.7 mm and WS = 0.7 mm.

$$W \approx \left(\frac{377}{Z\sqrt{\varepsilon_r}} - 1.57 \right) h \tag{6.27}$$

$$l = \frac{\theta \lambda_g}{2\pi} \tag{6.28}$$

6.3.4 Simulation and Measurement

The theoretical, simulation and the measured results of the single-mode bandpass are shown in Figures 6.16, 6.17 and 6.18, respectively. The theoretical results of the bandpass filter exhibits a high out-of-band rejection with an insertion-loss of 0 dB and about 17 dB of return-loss. The simulated results show the filter to exhibit an insertion-loss of less than 0.3 dB and a return-loss of about -17 dB. The insertion-loss and return-loss of the measured results in Figure 6.18 are 0.5 dB and 15.54 dB, respectively. The measured results validate the theoretical and simulation models.

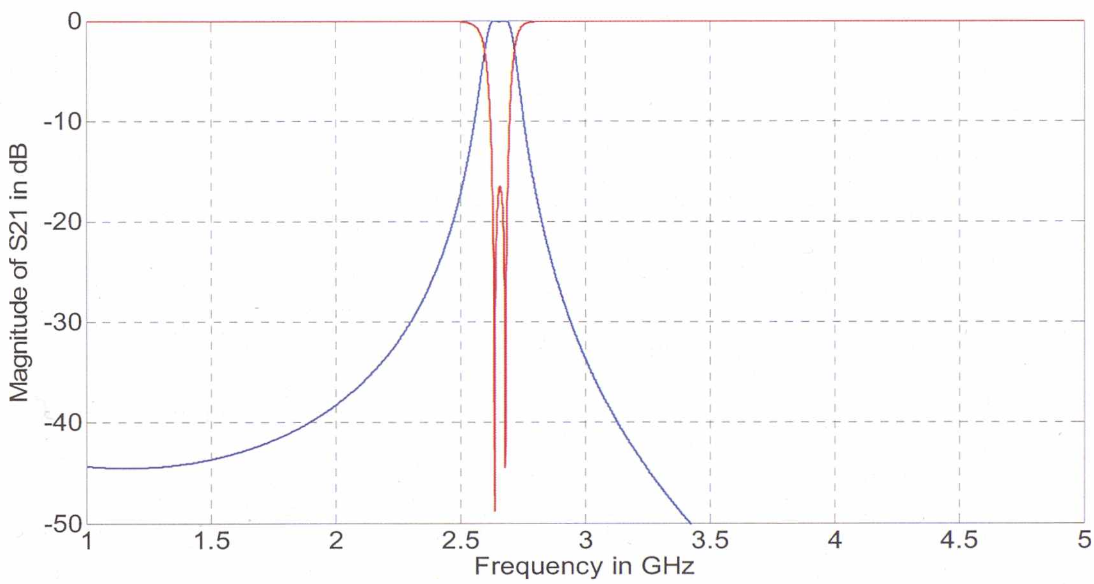

Figure 6. 16 The theoretical results of the proposed bandpass filter.

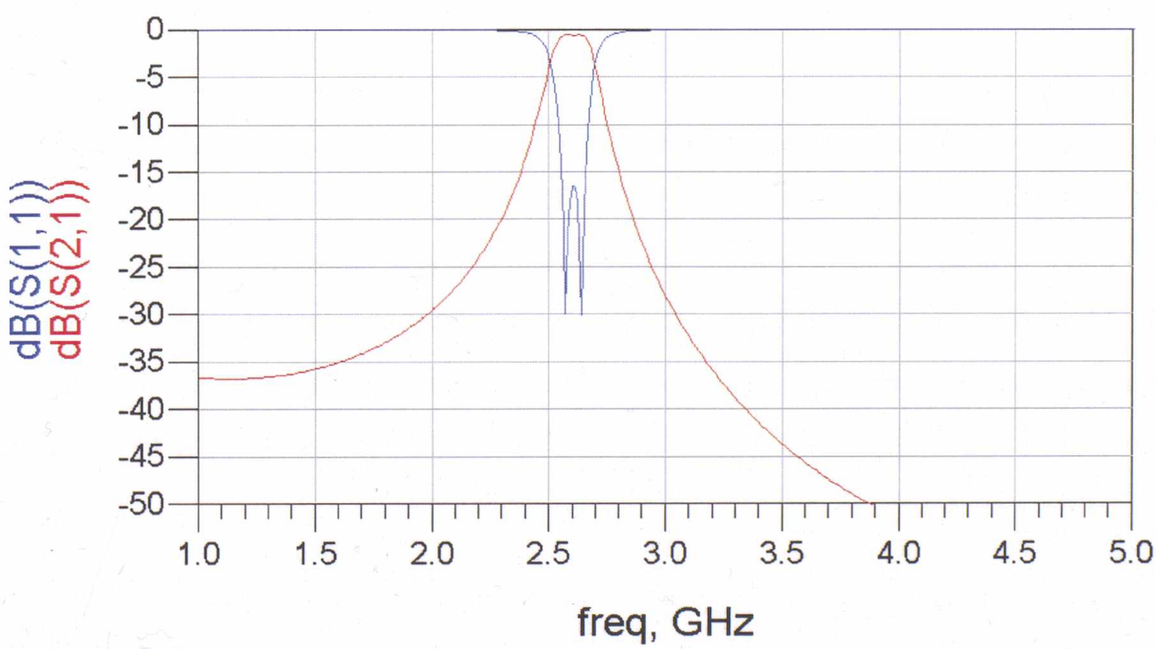

Figure 6. 17 The simulated result of the proposed bandpass filter.

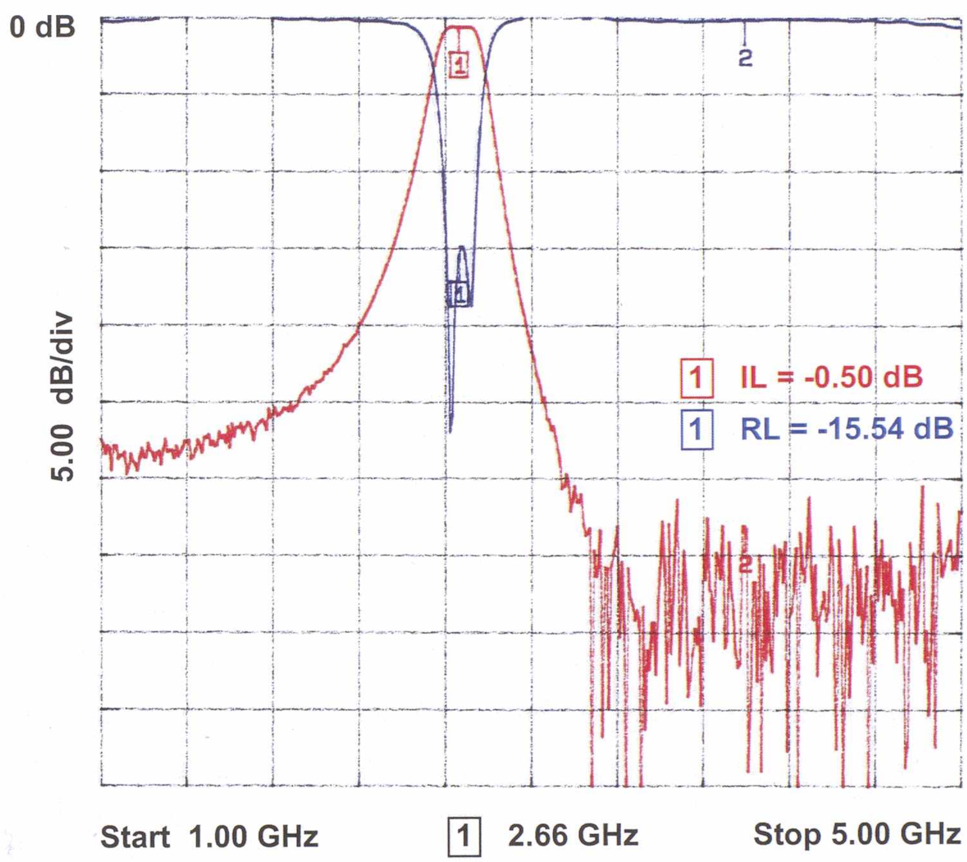

Figure 6. 18 The measured results of the proposed bandpass filter.

6.3.5 Dual Passband Bandpass Filter Case

Figure 6.19 shows the relation between the finger width Ws, the gap between the finger G and the distance between the two resonant frequencies Δf. Parameter Ws was studied for various values from 0.1 to 0.7 mm, and the maximum distance between the two resonant frequencies Δf was obtained when Ws is a minimum. It was found that Δf decreases with an increase in Ws, and that Δf can be controlled by the fingers width G. Δf increases with a decrease in G. So by selecting the minimum values for Ws and G it was possible to optimise the maximum value for Δf of 2.2 GHz, i.e. Δf can be controlled anywhere between 0 and 2.2 GHz.

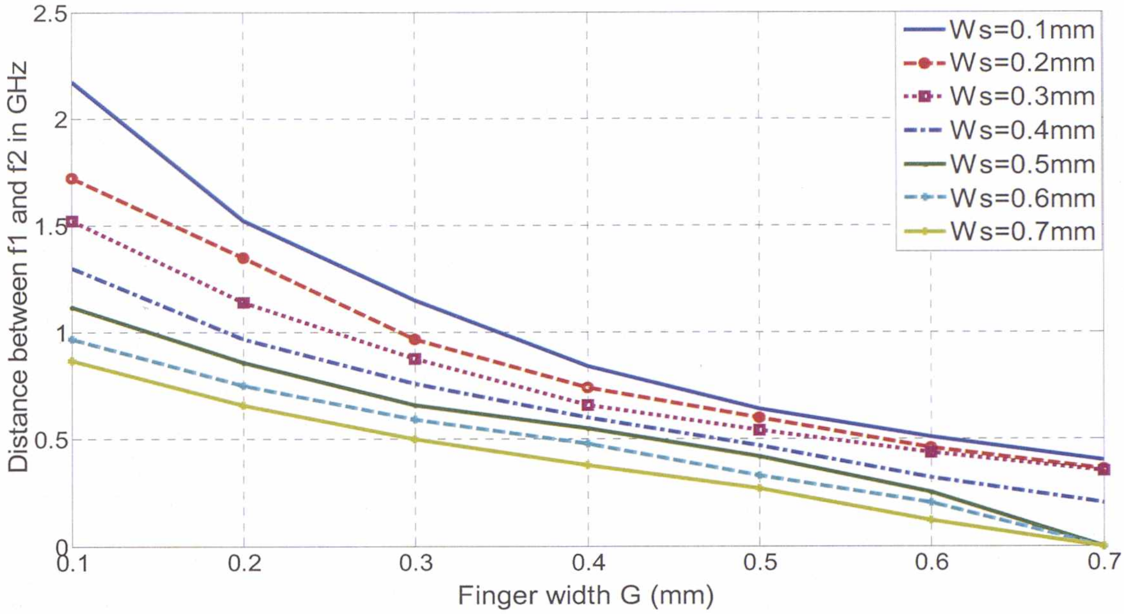

Figure 6. 19 Relationship between parameters Δf, Ws and G.

As an example, to obtain a second passband which is 1.4 GHz from the first passband, in particular at 4 GHz, then appropriate values of parameters G and Ws can be selected from Figure 6.19, thus

G = 0.2 mm, Ws = 0.2 mm

or G = 0.22 mm, Ws = 0.1 mm

The first choices were selected due to difficulty of fabricating the very small dimension of Ws.

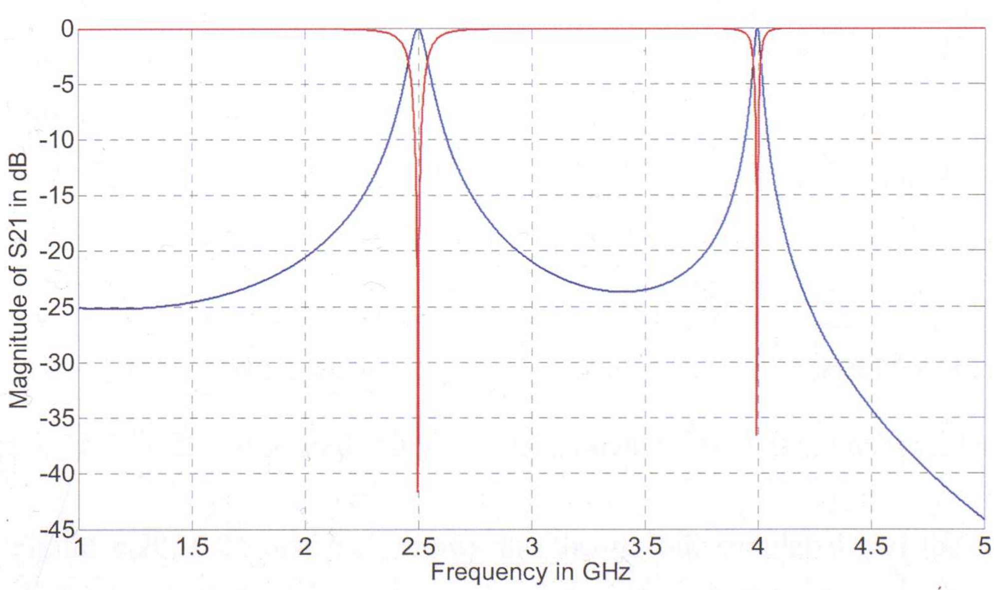

Figure 6. 20 Theoretical response of the dual passband filter in Fig. 6.12.

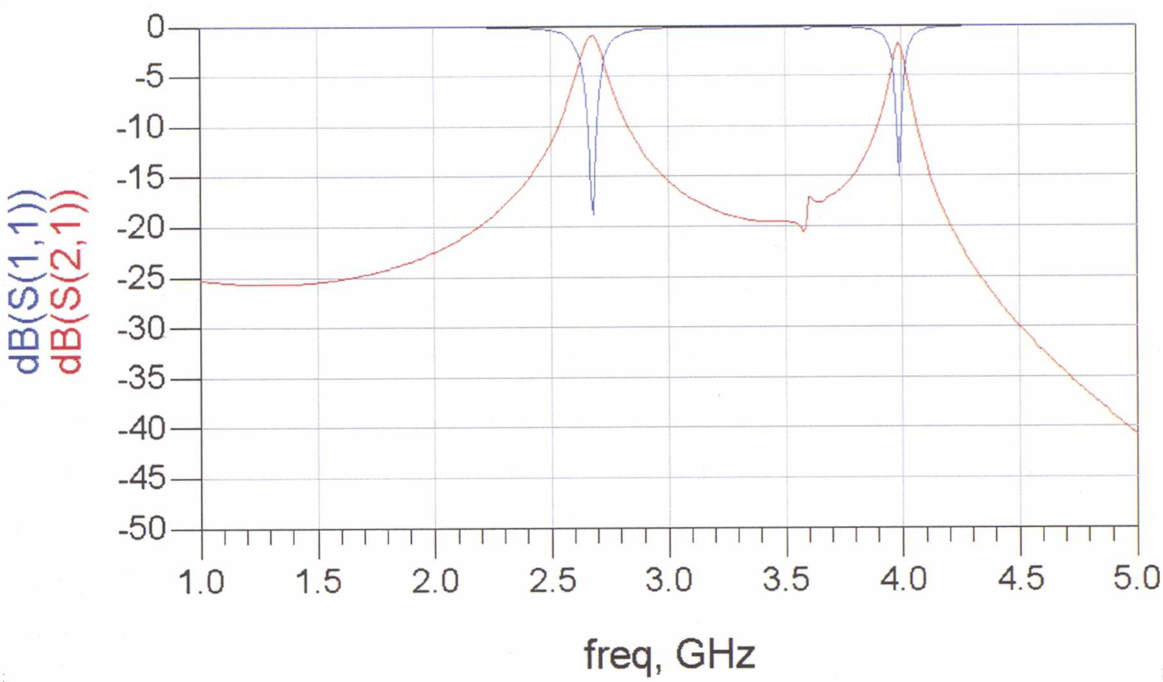

Figure 6. 21 The simulated results of the dual-passband filter in Fig. 6.12.

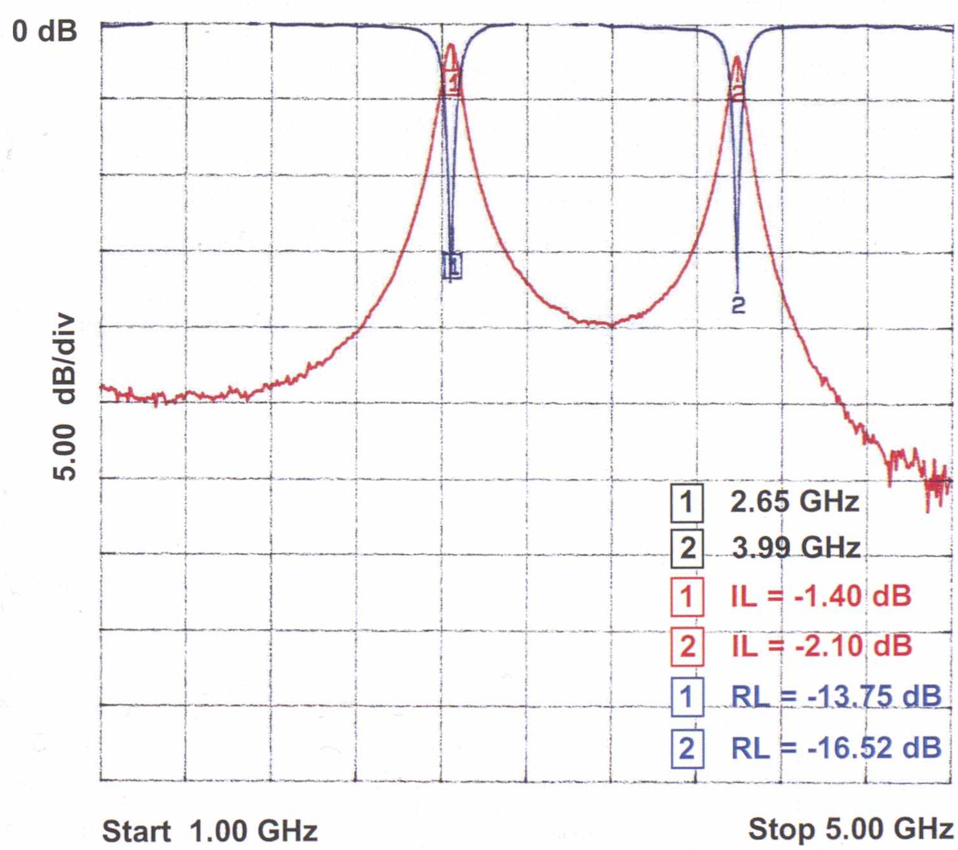

Figure 6. 22 The measured results in case of dual passbands bandpass filter.

Figure 6.20, 6.21 and 6.22 shows the theoretical, simulated and the measured results, respectively, of the proposed bandpass filter for a dual passband mode response. The theoretical result shows an ideal filter with no insertion-loss and high return-loss at both pass bands. This is expected as the theoretical model is assumed lossless. The simulated lower passband has an insertion-loss and return-loss of 1 dB and 18 dB, respectively, at 2.7 GHz; and for the upper passband the insertion-loss and return-loss are 2 dB and 15 dB, respectively, at 4 GHz. The measured response in Figure 6.22 shows the lower passband to have an insertion-loss of 1.40 dB at 2.65 GHz with 13.75 dB of return-loss; and the upper band to have an insertion-loss of 2.0 dB at 3.99 GHz with 16.52 dB of return-loss. There is excellent correlation between the simulated and measured results. The observed differences between simulations and measurements are attributed to the fabrication tolerance. The conductor loss, dielectric loss and non-ideal microstrip/coaxial line transitions also contribute to the insertion-loss of the filter. Figure 6.23 shows a photograph of the fabricated filter.

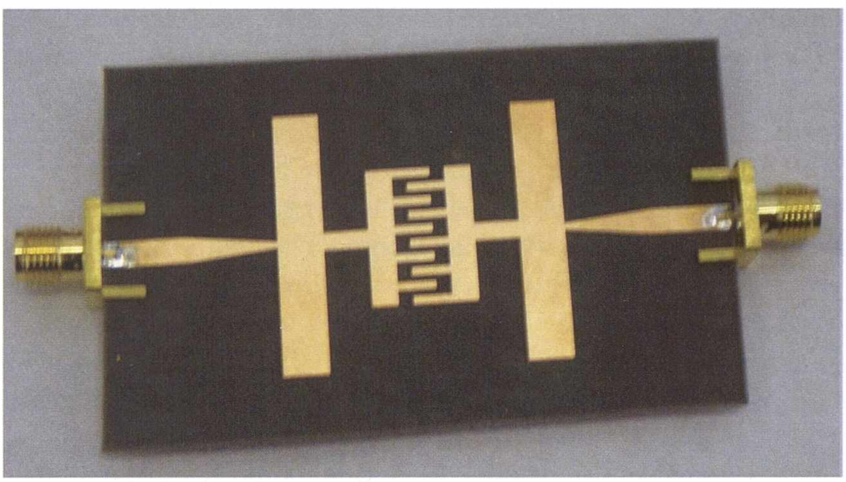

Figure 6. 23 Photograph of the fabricated proposed filter

6.4 References

[1] S. Wu and B. Razavi, "A 900-MHz/1.8-GHz CMOS receiver for dual band applications," IEEE.J. Solid-State Circuits, vol. 33, no. 12, pp. 2178–2185, Dec. 1998.

[2] S. Sun and L. Zhu, "Compact dual-band microstrip bandpass filter without external feeds," IEEE Microw. Wireless Compon. Lett., vol.15, no. 10, pp. 644–646, Oct. 2005.

[3] M.H. Wang, H.W. Wu, and Y.K. Su, "Compact and low loss dual band bandpass filter using pseudo-interdigital stepped impedance resonators for WLANS," IEEE Microw. Wireless Compon. Lett., vol. 17, no. 3, pp. 187–189, Mar. 2007.

[4] X.Y. Zhang, J.X. Cheng, Q. Xue, and S.M. Li, "Dual-band bandpass filters using stub loaded resonators," IEEE Microw. Wireles Compon. Lett., vol. 17, no. 8, pp. 583–585, Aug. 2007.

[5] P. Mondal and M.K. Mondal, "Design of dual-band bandpass filters using stub-loaded open-loop resonators," IEEE Trans. Microw. Theory Tech., vol. 56, no. 1, pp. 150–154, Jan. 2008.

[6] X. Y. Zhang and Q. Xue, "Novel centrally loaded resonators and their applications to bandpass filters," IEEE Trans. Microw. Theory Tech., vol. 56, no. 4, pp. 913–921, Apr. 2008.

[7] Xiu Yin Zhang, Jian-Xin Chen, *IEEE*, Quan Xue, *IEEE*, and Si-Min Li "Dual-Band Bandpass filter using stub-loaded resonators", IEEE Microw. And Wireless Components Letter, Vol. 17, No. 8, August 2007, pp. 583.

[8] W.-H. Tu and K. Chang, "Compact microstrip bandstop filter using open stub and spurline," *IEEE Microw. Wireless Compon. Lett.*, vol. 15, no. 4, pp. 268–270, Apr. 2006.

[9] Y.-Z.Wang and M.-L. Her, "Compact microstrip bandstop filters using stepped-impedance resonator (SIR) and spur-line sections," *Proc. Inst. Elect. Eng.*, vol. 153, no. 5, pp. 435–440, Oct. 2006.

[10] G.L. Matthaei, L. Young, and E.M. Jones, Microwave Filters, Impedance-Matching Network, and Coupling Structures. Norwood, MA: Artech, 1980.

[11] C.W. Tang and Y.K. Hsu, "Design of a wide stopband microstrip bandpass filter with asymmetric resonators," IEEE Microw. Wireless Compon. Lett., vol. 18, no. 2, pp. 91–93, Feb. 2008.

[12] D.M Pozar, Microwave Engineering, Wiley 2004.

Chapter 7 Conclusion and Future Work

The radio spectrum is an enigmatic natural resource that offers immense benefit to industry, government, and private citizens by supporting radio/wireless communications and a wide variety of other systems such as radar and remote sensing. It is non-depleting and exists everywhere, but it is finite and can be rendered less useful by noise and interference. Until recently, traditional methods of allocating spectrum and assigning channels have ensured effective and efficient use of the spectrum. Today, the rapidly expanding competition for spectrum use for wireless communication systems and the practice of spectrum auctions have increasingly necessitated the efficient usage of the limited frequency spectrum. In addition, with increasing subscriber numbers the interference between different systems is likely to increase. To avoid inter-modulation in the RF front ends, highly selective preselect filters are required for an efficient exploitation of the spectrum. Hence the aim of this research was to investigate novel microwave resonant structures that enable fabrication of compact narrowband microwave filters.

The main drawback of traditional planar microwave filters is the presence of unwanted frequency passband responses, which are a consequence of parasitic resonances at the harmonics of the fundamental frequency. These devices exhibit a periodic dependence of line impedance with length and frequency, the presence of these spurious frequency passbands is thus inevitable. Unfortunately, these undesired responses may degrade device performance and may be the origin of signal interference between neighbouring channels. To circumvent these problems this thesis presents novel microstrip filter structures and presents numerous designs and experimental results. The planar filters developed in the thesis have desired attributes of highly selectivity analogous to quasi-elliptic function filters, relatively narrow-bandwidth, low passband insertion-loss and high return-loss, and high out-of-band rejection in order to minimize the unwanted radiation interfering with other wireless systems. Also developed were dual passband filters whose second passband centre frequency can be controlled precisely. Dual-band filters are needed in systems where RF transceivers operate in multiple separated frequency bands so that users can access various services with a single multimode handset or terminal. Traditional techniques for designing dual-band filters is to combine two bandpass filters which are designed for two different centre frequencies, but, it requires an implementation area twice that of a single-band filter and additional external combining networks. The filters presented in this thesis satisfy the stringent requirements demanded for mobile and satellite communication systems. The filters also possess other desirable features such as being miniature and highly compact compared to traditional microwave filter designs, light weight, low cost and can be easily be integrated into a wireless communication system. In addition, the structure of the filter can be implemented using monolithic microwave integrated technology (MMIC).

The 'C-shape' resonator structure was theoretically analysed by using a simple transmission-line model and ABCD Matrix to derive the two transmission zero frequencies, and hence the centre frequency of the filter. The theoretical results were then verified by using Agilent's ADS-Momentum which uses a 2.5D method of moments technique to arrive at an accurate solution. The 'C-shape' resonator was also thoroughly analysed to ascertain the parameters that affect its function. The two attenuation poles were calculated based on the theory and they were confirmed by simulation results. It was shown that there was a very good correlation between the simulated and calculated results, i.e. about 95%. The discrepancy is attributed to the lossless models employed in the theory as well as the unaccounted losses at the abrupt transition at the resonator's corners.

The 'C-shape' structure was then compacted to reduce its dimension by folding inward the open-end to form a compact 'C-shape' resonator. The symmetrical and asymmetrical input and output feed-line cases were examined. It was shown that for the symmetrical input/output tapping feed-lines case, (i.e. $l_1 \neq l_2$) resulted in a bandpass response that was devoid of any transmission zero and its selectivity was moderate. Furthermore, it was shown that when $l_1 = l_2$ in the symmetrical case, there was no output response. In contrast, the asymmetrical case, the resonator produced a bandpass response with attenuation poles located on either side of the passband. The subsequent work was based on the asymmetrical scenario.

The compact 'C-shape' structure was then theoretically analysed and verified using ADS-Momentum. It was shown that the worst-case error between simulated and calculated results in the location of the transmission zeros was 10%. This discrepancy can be attributed to the lossless theoretical model and the eight corners sections in the schematic that were additional and not accounted for in the calculation. Moreover, the coupling gap C_c was not accounted for in the theoretical calculation. It was also shown that the tapping line positions affect the resonator's centre frequency, and the error in the calculated and simulated attenuation poles (i.e. around passband) for various tapping positions provided an average combined error for both poles of around 9.7%.

The effect of l_1 (i.e. the length of short section of compact 'C-shape' structure) was then analysed and it was shown that as l_1 increased, first attenuation pole, f_1 increases and second attenuation pole, f_2 decreases; this parameter controls the sharpness of the skirt rejection. Moreover, the return-loss was reduced and insertion-loss was increased when l_1 increases. From these results, the optimum position for l_1 and l_2 were selected to be 13.63 mm and 17.63 mm, respectively, because this configuration provided sharp filter skirt, i.e. rejection, while maintaining a reasonably low insertion-loss.

The effect of coupling in the compact 'C-shape' structure was also analysed by changing the following parameters: the input/output tapping feed-line positions, the coupling gaps C_c at the open-end boundary and the coupling gap C_g between the two electrically coupled sections (i.e. left and right sections) of the resonator. When the input and output lines are tapped at offset position "t" from the resonators horizontal centre plane (i.e. virtual ground-plane) and is increased, the coupling becomes stronger but the external quality factor Q_E declines significantly. When coupling gap C_c is large, the magnitude of coupling effect is less. It was also verified that as coupling gap C_g reduced, over-coupled occurred but the 3-dB bandwidth become broader. It is, however, worth pointing out that the coupling effect of gap C_g is more significant as compared to the effect of gap C_c. Hence, the optimal values of coupling gaps C_c and C_g are selected at 5.58 mm and 0.2 mm, respectively.

Manipulation of the resonator's line width by reducing it had a pronounced effect on the filter's 3-dB bandwidth, e.g. for a line width of 2 mm, the 3-dB bandwidth was 285 MHz, while for a line width of 200 microns, the 3-dB bandwidth increased by a factor of more than three to 959 MHz which corresponds to a fractional bandwidth of 24.6%. The added bonus of reducing line width was to realise a filter response with a relatively low passband insertion-loss and a high return-loss. Hence the best and feasible line width for this resonator was chosen to be 200 microns.

The compact 'C-shape' resonators were fabricated on 3M Cu-clad 217 substrate with $\varepsilon_r = 2.17$ and $h = 0.794$ mm, and having line width of $w = 1$ mm and $w = 0.2$ mm. The resonator with a line width of 1 mm provided a passband response centred at 3.5975 GHz, with an insertion-loss of 1.14 dB, return-loss of 13.20 dB and 3-dB bandwidth of 330 MHz. The result showed an excellent agreement between the simulated and measured results in terms of location of centre frequency and return-loss with errors of only 1.91% and 0.6%, respectively. The disagreement in insertion-loss of 54.51% was attributed to the fabrication tolerance and the accuracy of the substrate thickness employed. Furthermore, the fabricated filter exhibits a wider 3-dB bandwidth with 23.13% error, which is due to a smaller coupling gap C_g between the two electrically coupled sections of the resonator in the fabricated circuit as the 3-dB bandwidth inversely related to the gap C_g.

For the resonator with line width of 200 microns, the fabricated filter produced a 3-dB bandwidth of 1027 MHz with a fractional bandwidth of 24.63% at centre frequency of 4.17 GHz. The fabrication errors for this resonator are higher because of the very thin line width. The measured return-loss is 24% higher than the simulated data. The insertion-loss error is 12.29%, however, the measured insertion-loss is only about 1 dB, which is practically acceptable. The difference between the simulation and measurement results is considered to be due to the process where the fabrication error, accuracy of substrate dielectric constant and simulator precision are non-negligible.

It was also demonstrated that the modification of compact 'C-shape' resonator by compacting the structure to form 'E-' and 'G-shape' resonators could enhance filter performance. By increasing the folded arms length, the positions of the centre frequency, f_o and the two attenuation poles (i.e. f_1 and f_2) are shifted to lower frequencies value. In addition, a 4^{th} attenuation pole is generated at the higher frequency, which has higher control over the out-of-band rejection and enhances the steepness of the filter's cutoff point.

In Chapter 5, two new design structures of resonators namely 'Embedded-Square' and 'Embedded-Triangle' resonators are developed and shown to eliminate spurious interference responses across a wide frequency band. These new filters were developed by embedding additional structures within the compact 'C-shape' resonator. The simulated and experimental performances of these filters showed good agreement with each other. The fabricated 'Embedded-Square' resonator has a 3-dB bandwidth of 533 MHz with a fractional bandwidth of 18.22 % at 2.925 GHz. The passband insertion-loss exhibited by this resonator is only 0.68 dB. This resonator produces a passband rejection better than 14 dB and it suppresses spurious responses by more than 15 dB up to 13.5 GHz, i.e. $4f_o$.

The second structure, namely 'Embedded-Triangle' resonator is able to achieve a 3-dB bandwidth of 715 MHz with a fractional bandwidth of 22.34% at centre frequency of 3.2 GHz. The return-loss and insertion-loss of this structure are 24.83 dB and 0.56 dB, respectively. In addition, this resonator is able to provide out-of-band rejection of about 15 dB up to 17.6 GHz, i.e. $4f_o$. This 'Embedded-Triangle' resonator shows improvement over the 'Embedded-Square' resonator not only in the 3-dB bandwidth but also in the suppression of spurious response up to a higher frequency range. Hence, this resonator exhibits an improved performance over the 'Embedded-Square' structure and is therefore more suitable for many practical applications which emphasise broadband spurious free responses. The proposed filters exhibit good stopband rejection and their measured results confirm the validity and the usefulness of the proposed 'Embedded-Square' and 'Embedded-Triangle' resonators structure in many practical applications.

A novel approach is described to design and implement an ultra-wide stopband planar bandpass filter with a sharp cut-off by loading the open-loop resonators with triangular shaped patches with slots. The geometrical parameters and position of the slots determine the notch frequency. Also included within the open-loop structure are open-end stubs that further extend the filters rejection band. The filters' effectiveness for harmonic suppression is demonstrated via fabricated. Compared with the conventional structure the proposed filter provides a high out-of-band rejection and wideband characteristic. The measured centre frequency is 3.04 GHz, insertion-loss is 0.10 dB and return-loss is 22.01 dB. The filter's 3-dB fractional bandwidth is 16.87%. As shown in Figure 5.21 the filter provides ultra-broadband spurii rejection greater than 15 dB across the frequency range 1 to 20 GHz.

A novel microstrip bandpass filter has been presented that employs stepped impedance ring resonator structure with direct feed lines to realise a compact device. The filter exhibits a sharp elliptical response with a low passband transmission and matching characteristics as well as a high out-of-band rejection due to the two transmission zeros near its passband. The devices' feasibility was validated by simulation and practical measurements. The filter designed at 2.30 GHz exhibited a sharp passband response, an excellent return-loss (18.2 dB) and insertion-loss (0.57 dB), as well as a very wide stop band rejection of >15 dB across the frequency range 1 to 8.8 GHz ($4f_o$).

Novel dual-band microstrip bandpass filters were developed by modifying the 'C-shape' open loop resonator. It was discovered that by loading the modified resonator with 'T-shape' stub it was possible to precisely control the upper passband response. This property was also verified theoretically and confirmed with simulation and experimental results. The selectivity of the proposed filter was improved further by incorporating spur-lines into the input and output feed-lines. With stub loading the measured results show an insertion-loss of 1.08 and 1.8 dB for lower and upper passband, and return-loss greater than 14 dB for both passband responses located at 4.15 and 5.62 GHz. Without stub two passband responses are located at 4.15 GHz and 7.38 GHz, where the lower passband insertion-loss is 0.9 dB and the return-loss is more than 19.43 dB, and the upper passband insertion-loss is about 4 dB and the return-loss is more than 13.40 dB.

Another novel microstrip bandpass filter is proposed, which consists of two asymmetric resonators and the inter-digital capacitor. By changing the parameters of the inter-digital capacitors changes the coupling between the two resonators, and this leads to change from dual-mode single passband to single-mode dual passband bandpass filter. The measured response, for an inter-digital capacitor finger width and gap between the finger of 200 microns, lower passband has an insertion-loss of 1.40 dB at 2.65 GHz with 13.75 dB of return-loss; and the upper band has an insertion-loss of 2.0 dB at 3.99 GHz with 16.52 dB of return-loss.

In conclusion the aim and objectives of this research project have been achieved, i.e. compact filters have been developed and tested, which possess desired properties of low insertion-loss, high return-loss, high selectivity, ultra-wideband spurious free response, low cost, and compact size. The resonator was analysed and modelled and confirmed from measurements. The investigation conducted includes theoretical modelling of the novel resonator structures, which enabled an insight of its operation and resonator's parameters that dictate its overall performance.

Future Work

Future work may include the following investigations:

- Developing a theoretical model that accounts for dielectric loss and loss attributed to non-uniform transmission-lines,
- Multi layer resonant structures to further reduce the size of the filter,
- Investigating of electronic tuning of the filters passband for reconfigurable applications required in software radio,
- Development of compact ultra-wideband filters for UWB applications in the FCC's unlicensed band between 3.1 to 10.6 GHz,
- Improving out-of-band rejection using defected ground-plane techniques, and
- Reducing the size of the filter using metamaterials.

APPENDIX I

MATLAB codes uses the equations (A1) to (A8) to calculate and plot the values of the lumped elements and the theoretical response throughout this research.

$$L(nH) = 2 * 10^{-4} l \left[ln\left(\frac{l}{W+t}\right) + 1.193 + 0.2235\frac{W+t}{l}\right].K_g \quad \text{for } l \text{ in } \mu m \qquad (A1)$$

$$K_g = 0.57 - 0.145\, ln\frac{W}{h} \qquad (A2)$$

$$C_p = 0.5C_e \qquad (A3)$$

$$C_r = 0.5\, C_0 - 0.25\, C_e \qquad (A4)$$

$$\frac{C_0}{W}(pF/m) = \left(\frac{\varepsilon_r}{9.6}\right)^{0.8} * \left(\frac{s}{W}\right)^{m_0} exp(k_0) \qquad (A5)$$

$$\frac{C_e}{W}(pF/m) = 12\left(\frac{\varepsilon_r}{9.6}\right)^{0.9} * \left(\frac{s}{W}\right)^{m_e} exp(k_e) \qquad (A6)$$

$$\left.\begin{aligned} m_0 &= \frac{W}{h}[0.619\, log(W/h) - 0.3853] \\ k_0 &= 4.26 - 1.453 log(W/h) \end{aligned}\right\} for\ 0.1 \leq s/W \leq 1.0 \qquad (A7)$$

$$\left.\begin{aligned} m_e &= 0.8675 \\ K_e &= 2.043(W/h)^{0.12} \end{aligned}\right\} \text{for } 0.1 \leq s/W \leq 0.3 \qquad (A8)$$

The calculated lumped element values for the 'Embedded-Square' filter using the MATLAB code provided are:

L1 = 1.48 nH
L2 = 1.05 nH
L3 = 0.2 nH
C_p = 0.0178 pF
C_r = 0.002 pF

The area of the triangle's shape highed below determines its capacitance.

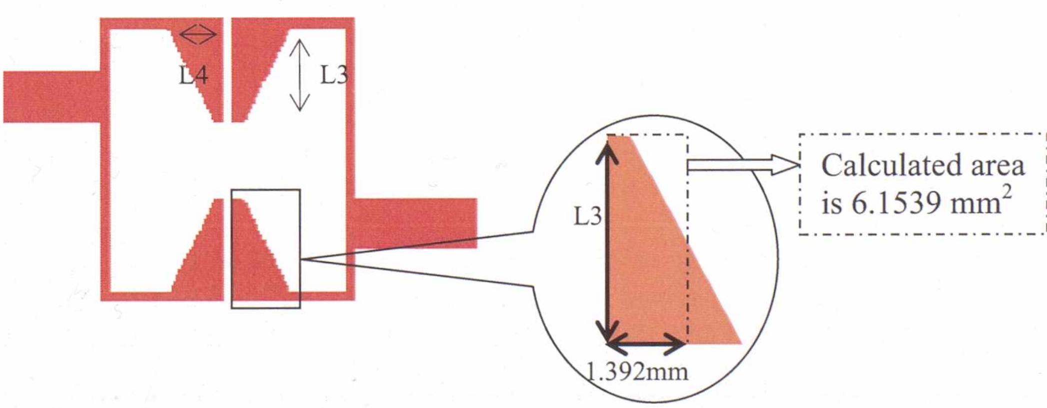

The calculated lumped element values for the 'Embedded-Triangle' using the MATLAB code provided are:

L1 = 1.03 nH
L2 = 0.7 nH
L3 = 0.1 nH
C_p = 0.02376 pF
C_r = 0.00209 pF

MATLAB CODES

```
%This MATLAB code to convert the microstrip gap to its
%equivalent lumped elements value (Cp and Cr where both
%output values are in pF)given its width, relative
%permittivity of the dielectric, height of dielectric and
%trace thickness
h=0.000794;       the thickness of the microstrip.
er=2.17;
s1 = input('inter the value of the Gap in mm: ');
W1 = input('inter the width value of the cap in mm: ');

s=s1/1000;
W=W1/1000;
mo=(W/h)*[0.619*log(W/h)-0.3853];
ko=4.26-1.453*log(W/h);
me=0.8675;
ke=2.043*(W/h)^0.12;

Co =[((er/9.6)^0.8)*((s/W)^(mo))* exp(ko)]*W;
Ce =[12*((er/9.6)^0.9)*((s/W)^(me))* exp(ke)]*W;

Cp=0.5*Ce
Cr=0.5*Co-0.25*Ce
```

```
%This MATLAB code to convert the microstrip inductors to
%its equivelent lumped elements value given its width,
%length, relative permittivity ofthe dielectric, height of
%dielectric and trace thickness
h=0.031259843; % the thickness of the microstrip in inch
               %=0.76mm.

l = input('Inter the length value of the inductor in mm:
');
W = input('Inter the width value of the inductor in mm: ');

w=W/0.039370079; %converting from mm to inch
b=l/0.039370079; %converting from mm to inch
L= 0.00508*b*(log(2*b/(w+h))+.5+0.2235*(w+h)/b)
```

```
%This MATLAB code to convert the microstrip capacitors to
%its equivalent lumped elements value given its widths,
%relative permittivity of the dielectric, height of
```

```
%dielectric and trace thickness Note the output values are
%in pF

h=0.000794;     % the thickness of the microstrip in meter
er=2.17;
t=0.000035;

a = input('inter the width value(W1) in mm: ');
b = input('inter the width value (W2)in mm: ');
W1=a/1000;     % converting to meter
W2=b/1000;     % converting to meter
C=[[2.64*(10^-11)*(er+1.41)]/[log((5.98*h)/(0.8*W1+t))]]*W2
```

Code to plot the response of both embedded-square and embedded-triangles filter:

```
%this matlab code for plotting the response of the
%embedded-square and embedded-triangle filters
clc;
clear all;

%these parameters to be changed according to filter
parameters

%==========================================================

L1=?????????????;
L2=?????????????;
Cp=?????????????;
Cr=?????????????;
Z0=50;
Y0=1/Z0;
k=0;
L3=?????????????;

%==========================================================

for f=[1:0.001:15]
w=2*pi*f*10e9;

A1=j*w*L1;
A2=1/((j*w*L3)+(1/(j*w*Cp)));
A3=1/(j*w*Cr);
A4=A2;
A5=j*w*L2;

B1=j*w*L2;
B2=A2;
B3=1/(j*w*Cr);
B4=A2;
B5=j*w*L1;

E = [1 A1; 0 1];
```

```
F = [1 0; A2 1];
G = [1 A3; 0 1];
H = [1 0; A4 1];
K = [1 A5; 0 1];

E1 = [1 B1; 0 1];
F1 = [1 0; B2 1];
G1 = [1 B3; 0 1];
H1 = [1 0; B4 1];
K1 = [1 B5; 0 1];

M=E*F*G*H*K;
L=E1*F1*G1*H1*K1;

A=M(1,1);
B=M(1,2);
C=M(2,1);
D=M(2,2);

Ab=L(1,1);
Bb=L(1,2);
Cb=L(2,1);
Db=L(2,2);

Y11t=(D/B);
Y22t=(A/B);
Y12t=((B*C)-(A*D))/B;
Y21t=-1*(1/B);

Y11b=(Db/Bb);
Y22b=(Ab/Bb);
Y12b=((Bb*Cb)-(Ab*Db))/Bb;
Y21b=-1*(1/Bb);

Y11=Y11t+Y11b;
Y22=Y22t+Y22b;
Y12=Y12t+Y12b;
Y21=Y21t+Y21b;

S21=(-2*Y21*Y0)/(((Y11+Y0)*(Y22+Y0))-(Y21*Y12));
S11=(((Y11-Y0)*(Y22+Y0))-(Y21*Y12))/(((Y11+Y0)*(Y22+Y0))-
(Y21*Y12));
k=k+1;
Y1(k)=S21;
Y2(k)=S11;
end;
figure(1);
plot([1:0.001:15], 20*log10(abs(Y1)));
hold on;
plot([1:0.001:15], 20*log10(abs(Y2)),'R');
grid
xlabel('Frequency in Ghz');
ylabel('Magnitude in dB');
```

```
title('Bandpass Filter Using ABCD Matrix');
```

Reference:

[1] Microstrip filters for RF/microwave applications By Jia-Sheng Hong, M. J. Lancaster

APPENDIX II

```
%This MATLAB code used to solve the designing equations for
%bandpass filter using inter-digital capacitor in chapter
%7, then the odd and the even mode of Y4 can be calculated
%according to equations 6.8 and 6.9 these variables defined
%as the following:
%x(1)=Q1;x(2)=Q3;x(3)=Q4;X(4)=y1;X(5)=y3;X(6)=y4;


function F =farhat(x)
 F(1) =(1/2)*(X(4)*x(1)*sec(x(1))*sec(x(1))+0.043)-0.0638;
 F(2) =(1/2)*(0.043+x(5)*x(2)*csc(x(2))*csc(x(2)))-0.0476;
F(3)=(1/2)*(x(6)*x(3)*sec(x(3))*sec(x(3))+x(5)*x(2)*csc(x(2
))*csc(x(2)))- (3.623*(x(5)*csc(x(2)))*(x(5)*csc(x(2))));
 F(4) = x(4)*tan(x(1))*tan(0.3825)-(1/63.84);
 F(5) =(1/(2*63.84))-(x(5)*tan(0.3825)*tan(x(2)))-
(x(6)*tan(x(3))*((1/2*x(5)*63.84)*tan(x(2))+tan(0.3825)));
clc;
clear all;

z = [0.1; 0.2; 0.4; 0.21; 0.1; 0.3]; % Make a starting
guess at the solution
options =
optimset('Display','iter','MaxFunEvals',1e+8,'MaxIter',1e+8
,'TolFun',0.00001);% Option to display output
[x,fval] = fsolve(@farhat,z,options) % Call optimizer
```